NANO-OPTOMECHANICAL SYSTEM BASED ON MICROWAVE FREQUENCY SURFACE ACOUSTIC WAVES

A DISSERTATION

SUBMITTED TO THE FACULTY OF

UNIVERSITY OF MINNESOTA

BY

SEMERE AYALEW TADESSE

IN PARTIAL FULFILLMENT OF THE REQUIREMENTS

FOR THE DEGREE OF

DOCTOR OF PHILOSOPHY

MO LI

JANUARY 2016

Acknowledgements

I would like to express my deepest gratitude to my advisor, Prof. Mo Li, for giving me the chance to work on this exciting project, and providing a conducive research environment to achieve the goals of the project. His excellent guidance, motivation, and timely feedback were instrumental for the success of my phd research. The patience and thrust he showed to me has carried me through difficult moments of my phd journey.

My acknowledgement also goes to Dr. Huan Li and Qiyu Lui with whom I formed effective collaboration in the last two projects of my research. Even before we jumped to collaborate on a project, Huan had been my immediate resource person for questions I had about my research. His insight and intelligent thoughts, willingness and patience to discuss any question I had at any time was amazing and contributed to the success of my research. I would also like to thank my group mates Dr. Jong Wook Noh Dong, Dr. Yu Chen, Nathan Youngblood, and Li He with whom I had interesting discussions about my research.

I am also grateful to Prof. Rhonda Franklin for allowing me use her lab microwave measurement resources for some of my experiments. Her graduate students Glenston Miranda, Chanjoon Lee and Alex Nelson were very cooperative and flexible in arranging a time table to share the measurement tool.

Finally, my gratitude goes to my parents, Ayalew Tadesse and Yewbdar Sinadir, and my wife Gerawork Fekadu for the love and support they gave me.

Dedication

To my wife, Gerawork, and our little angel Kalkidan.

Abstract

Cavity optomechnics studies the interaction of cavity confined photons with mechanical motion. The emergence of sophisticated nanofabrication technology has led to experimental demonstrations of a wide range of novel optomechanical systems that exhibit strong optomechanical coupling and allow exploration of interesting physical phenomena. Many of the studies reported so far are focused on interaction of photons with localized mechanical modes.

For my doctoral research, I did experimental investigations to extend this study to propagating phonons. I used surface travelling acoustic waves as the mechanical element of my optomechanical system. The optical cavities constitute an optical racetrack resonator and photonic crystal nanocavity. This dissertation discusses implementation of this surface acoustic wave based optomechanical system and experimental demonstrations of important consequences of the optomechanical coupling. The discussion focuses on three important achievements of the research.

First, microwave frequency surface acoustic wave transducers were co-integrated with an optical racetrack resonator on a piezoelectric aluminum nitride film deposited on an oxidized silicon substrate. Acousto-optic modulation of the resonance modes at above 10 GHz with the acoustic wavelength significantly below the optical wavelength was achieved. The phase and modal matching conditions in this paradigm were investigated for efficient optmechanical coupling.

Second, the optomechanical coupling was pushed further into the sideband resolved regime by integrating the high frequency surface acoustic wave transducers with

a photonic crystal nanocavity. This device was used to demonstrate optomecahnically induced transparency and absorption, one of the interesting consequences of cavity optomechanics. Phase coherent interaction of the acoustic wave with multiple nanocavities was also explored. In a related experiment, the photonic crystal nanoscavity was placed inside an acoustic echo-chamber, and interaction of a phonon pulse with the photonic nanocavity was investigated.

Third, an effort was made to address a major limitation of the surface acoustic wave based optomechanical system - loss of acoustic energy into the oxidized silicon substrate. To circumvent this problem, the optomechanical system was implemented in a suspended aluminum nitride membrane. The system confined the optical and acoustic wave within the thickness of the membrane and led to a stronger optomechanical coupling.

At the end a summary is given that highlights important features of the optmechanical system and its prospects in future fundamental research and application.

Table of Contents

List of Tables

List of Figures

Chapter 1. Introduction

1.1. Background

In the last decade, cavity optomechanics has emerged as an interesting research area in the optical physics and photonics community [1]. It studies the mutual coupling of optical and mechanical degrees of freedom of optical interferometric structures. These structures, generally called optomechanical systems, harbor both optical and mechanical resonant modes. Radiation pressure force accounts for the mutual coupling of these two different degrees of freedom.

Photons carry momentum and induce radiation pressure forces when impinging on objects. Though this force can be too minute to significantly affect macroscopic objects, meticulously designed and fabricated mechanical systems can feel the force and measurable changes of mechanical state can be observed. More importantly, the use of a high quality optical resonator will greatly amplify the radiation pressure force as the intracavity field will be resonantly enhanced. The theoretical analysis of this force was formulated by Maxwell, and a series of experimental demonstrations later showed photons interact with atoms and macroscopic objects through transfer of linear and angular momentum [2]–[4]. These fundamental physics studies had inspired and led demonstrations of interesting applications of optical force. In the 1970s, Ashkin used optical force from focused laser beams to trap and manipulate dielectric particles [5]. The nonconservative nature of the force was utilized in laser cooling of atomic motion which now has become an indispensable technique in ultracold atom experiments [6], [7]. In the 1960s, in an effort to improve the measurement sensitivity of gravitational wave

detectors, Vladimir Braginsky and co-workers theoretically investigated and experimentally demonstrated the use of radiation pressure to cool macroscopic objects in the realm of microwave cavity [8], [9]. This experiment was later extended to the optical regime where a Fabry-Perot cavity was shown to exhibit optical bistability due to radiation pressure induced change of its cavity length [10]. This experiment marked the beginning of cavity optomechanics.

The advent and possibility of fabricating high quality factor whispering gallery mode optical resonators and minuscule mechanical oscillators brought a new enthusiasm and intense interest to cavity optmechanics [11]. Beginning in 2005, a plethora of cavity optomechanics experimental demonstrations were reported which were based on a wide range of novel whispering gallery mode optical resonators and other interfermeteric structures. These experiments demonstrated interesting consequences of cavity optomechanics like radiation pressure induced self oscillations [12]–[14], feedback cooling of mechanical motion [15]–[17], optomechanically induced transparency [18], [19], precision displacement measurements down to the standard quantum limit [20]–[22], and many more. The enthusiasm around cavity optomechanics stems from not only its importance in studying fundamental physics but also its potential applications in engineering. It is a promising candidate for high precision measurements of displacements, forces, and accelerations. It also provides a unique platform for classical and quantum information processing, for example, as a coherent interface between optical and microwave signals, and as a quantum memory.

1.2. Objective of the study

There is a continuing effort to realize many more novel optomechanical systems which will have merits in achieving these applications with better performance and ease of implementation. Many of the studies reported so far are focused on interaction of photons with localized mechanical modes. For this dissertation, we did experimental investigations to extend this study to propagating phonons. We used surface travelling acoustic waves as mechanical elements of our optomechanical system. For the optical component, a racetrack ring resonator and a photonic crystal beam cavity were used. We believe our optomechnaical system will be part of the optomechanics toolbox where some of its unique features make it a good alternative in the applications cavity optmechnaics aspires to realize. For example, the propagating nature of the high frequency phonons of our system and the possibility to electrically induce these mechanical waves make it a viable candidate for a coherent link between optical and microwave domains. Our work has resulted in publication of three papers [23]–[25]. This thesis presents the experimental results reported in these published articles.

1.3. Organization of the thesis

In this introduction chapter, I gave a short overview of cavity optomechanics and its coupling mechanism. Potential applications and prospects of the field are introduced. In the next chapter, I will discuss surface acoustic waves, the mechanical element of our optomechanical system. Basic physics, modeling techniques, design and fabrication issues, and device characterization results are presented. Chapters 3-5 are compiled presentations of the journal articles published from this work.

Chapter 3 discusses our experimental demonstration of acousto-optic modulation of an optical racetrack ring resonator with microwave frequency surface acoustic waves [23]. The experimental technique used to integrate the surface acoustic wave and optical resonator devices is explained. A quantitative analysis of coupling efficiency between the surface acoustic wave and the optical cavity is given.

Chapter 4 discusses our experimental work in utilizing the integrated surface acoustic wave photonic cavity system to demonstrate optomechanically induced transparency and absorption [24]. Coherent and strong optomechanical coupling between surface acoustic wave and multiple photonic cavities is also discussed. In a related experiment, we further studied the photon-phonon interaction by placing a photonic cavity inside an acoustic echo-chmaber and probing the echo pulses optically. Both frequency and time domain measurement results are discussed. This work was done in collaboration with Dr. Huan Li and Qiyu Lui.

Chapter 5 describes the experiments and results obtained in an attempt to overcome some of the limitations of our surface acoustic wave based optomechnical system. In this experiment, we implemented the optomechanical system on a suspended membrane to avoid the loss of acoustic wave energy to the silicon substrate [25]. The design, fabrication, and improved optomechanical coupling efficiencies are reported. This work was also done in collaboration with Dr. Huan Li and Qiyu Lui.

Finally, I will conclude the report by highlighting important achievements of this research and its implications for future work in the field of optical physics and photonics.

Chapter 2. Surface Acoustic Waves

2.1. Introduction

Surface Acoustic Waves (SAW) are periodic mechanical vibrations that propagate on the surface of an elastic medium. The study of SAW dates back to 1885 when Lord Rayleigh predicted its mode of propagation and properties [26]. This acoustic wave propagates on the surface of an elastic medium with the particles vibrating in the plane containing the surface normal and the propagation direction (sagittal plane), and its amplitude decreasing with substrate depth [27]. This type of SAW wave is usually referred as Rayleigh type SAW wave. Rayleigh's motivation to study SAW was to explain seismic signals observed after a ground shock. He showed that the slower SAW wave accounts for the signal observed following the bulk acoustic waves of a ground shock. Though originally SAW were a topic of interest in geophysics and seismology communities, the ability to generate SAW in piezoelectric substrates later brought interesting applications in communication and microelectronics as signal processing units. Other types of SAW (like Love waves, Sezewa waves, etc.) with different polarization states were also studied and experimentally demonstrated. In this dissertation, however, only Rayleigh type SAW are considered.

In this chapter I discuss the basic physics of SAW, their generation mechanism, typical modeling techniques, fabrication processes, characterization methods, and measurement results of representative devices.

2.2. Basic Physics of SAW

2.2.1. Piezoelectricity

The first experimental demonstration of piezoelectricity dates back to 1880 when Pierre Curie and Jacques Curie observed surface charges appearing on crystals such as quartz when subjected to mechanical stress [28]. In order to distinguish this phenomenon from pyroelectricity, which is electricity generation by heating, this phenomenon was named piezoelectricity which literally means electricity generated from pressure. The inverse process where mechanical deformation is induced by electricity was later deduced from fundamental thermodynamic principles by Lippmann in 1881 [29]. The Curie brothers later confirmed this inverse process experimentally. The development of the field continued with a rigorous mathematical description of the process and identification of crystal groups that exhibit this phenomenon. The first experimental observations of piezoelectricity were restricted to naturally occurring crystalline materials like quartz, topaz, tourmaline and the like. But later this attribution was extended to manmade ceramic perovskite crystals like Barium titanate (BaTiO3), Lead zirconate titane (PZT), Lithium Niobate (LiNbO3), Lithium Tantalate (LiTaO3), etc. GaAs, AlN, ZnO are some examples of semiconductors that exhibit piezoelectricity.

The physical origin of piezoelectricity can be explained in relation to the existence of electric dipole moments in solid crystals which are induced on lattice sites with asymmetric charge surroundings. When a mechanical stress is applied to a piezoelectric material, the crystal geometry changes such that the ions in the structure are displaced and an effective dipole moment is created. To get non-vanishing polarization,

the dipole formed must not be cancelled out by other dipoles in the unit cell, and hence the crystal structure should be non-centrosymmetric. Of the 32 crystalline classes, the 20 non-centrosymmetric crystal classes exhibit piezoelectricity. In the reverse piezoelectric process, when the material is subjected to external electric field, a dipole moment is formed and results in deformation. In the other classes of piezoelectric materials, which also happens to be ferroelectric, there already exists electric dipoles in the structure even in the absence of external electric field. In such materials, neighboring dipoles aggregate into clusters called Weiss domains. These domains are usually randomly oriented; however, a poling process (subjecting the material to a uni-directional strong electric field) can align the domains in ceramic piezoelectric crystals and induce strong piezoelectric characteristics.

2.2.2. Field Equations

Quantitative analysis of piezoelectricity was done by Voigt and Duhem who formulated a macroscopic phenomenological theory based on thermodynamic principles. This thermodynamic approach predicts the reversibility of the direct and indirect piezoelectric effects and equivalence of the corresponding constants. The formulation is summarized below as is given in [30].

The total internal energy density of a piezoelectric material is the sum of the mechanical and electrical work done, and is given in differential form as:

$$dU = T_{ij} ds_{ij} + E_m dD_m \qquad \textbf{2.1}$$

where E_m and D_m are electric field and electric displacement vectors respectively, T_{ij} is the mechanical stress second rank tensor and s_{ij} denotes the mechanical strain second rank tensor which can be written in terms of spatial gradient of displacement u_i as

$$s_{ij} = \frac{1}{2}\left(\frac{\partial u_i}{\partial x_j} + \frac{\partial u_j}{\partial x_i}\right). \quad \textbf{2.2}$$

The electric Gibbs energy (electric enthalpy), $G = G(s_{ij}, E_i)$ can be written in its differential form as:

$$dG = \left(\frac{\partial G}{\partial s_{ij}}\right)_E ds_{ij} + \left(\frac{\partial G}{\partial E_m}\right)_s dE_m. \quad \textbf{2.3}$$

Taking its relation with total internal energy density, $G = U - E_i D_i$ the Gibbs energy can also be written as:

$$dG = T_{ij} ds_{ij} - D_m dE_m. \quad \textbf{2.4}$$

Comparing the above two differential forms of the Gibbs energy gives

$$T_{ij} = \left(\frac{\partial G}{\partial s_{ij}}\right)_E \quad \textbf{2.5}$$

$$D_m = -\left(\frac{\partial G}{\partial E_m}\right)_s \quad \textbf{2.6}$$

which implies that $T_{ij} = T_{ij}(s_{ij}, E_m)$ and $D_i = D_i(s_{ij}, E_m)$.

The functional dependence of the mechanical stress and the electric displacement vector on strain and electric field leads to the differential forms

$$dT_{ij} = \left(\frac{\partial T_{ij}}{\partial s_{kl}}\right)_E ds_{kl} + \left(\frac{\partial T_{ij}}{\partial E_m}\right)_s dE_m; \quad \textbf{2.7}$$

$$dD_m = \left(\frac{\partial D_m}{\partial s_{kl}}\right)_E ds_{kl} + \left(\frac{\partial D_m}{\partial E_m}\right)_s dE_m. \quad \textbf{2.8}$$

The partial derivatives in the above differential equations are defined as:

$$\left(\frac{\partial T_{ij}}{\partial s_{kl}}\right)_E = C_{ijkl} \quad \textbf{2.9}$$

$$\left(\frac{\partial T_{ij}}{\partial E_m}\right)_s = -\left(\frac{\partial D_m}{\partial s_{kl}}\right)_E = -e_{ijm} \quad \textbf{2.10}$$

$$\left(\frac{\partial D_m}{\partial E_k}\right)_s = \varepsilon_{mk} \quad \textbf{2.11}$$

which are the fourth rank tensor of the elastic stiffness constants, the third rank tensor of the piezoelectric constant, and the second rank tensor of the dielectric permittivity constants respectively.

Integrating equations (2.7) and (2.8) at constant partial derivatives gives the constitutive relations that couple electrical and mechanical quantities as:

$$T_{ij} = C_{ijkl} s_{kl} - e_{ijm} E_m \quad \textbf{2.12}$$

$$D_m = e_{mij} s_{ij} + \varepsilon_{mk} E_k \quad \textbf{2.13}$$

Equation (2.12) describes the inverse piezoelectric effect by which mechanical stress is generated by electric polarization induced by applied electric field, where as equation

(2.13) describes the direct piezoelectric effect where a mechanical deformation induces an electric displacement.

2.2.3. SAW Propagation in Piezoelectric Materials

Generally elastic wave propagation in a piezoelectric material is governed by mechanical equations of motion and quasi-static electromagnetic Maxwell equations, together with the piezoelectric constitutive relations derived above. The equation of motion that governs how mechanical stress applied to an elastic medium of density ρ affects the time evolution of particle displacement is:

$$\frac{\partial T_{ij}}{\partial x_i} = \rho \frac{\partial^2 u_j}{\partial t^2}. \qquad \textbf{2.14}$$

Since the acoustic velocity in solids is much smaller than (five orders of magnitude smaller) the electromagnetic wave speed, a quasi-static approximation of the Maxwell's equation suffices to describe the electric field component of the elastic wave propagation in piezoelectric materials, which essentially means

$$\frac{\partial D_i}{\partial x_i} = 0. \qquad \textbf{2.15}$$

An analytical solution can be obtained by solving these equations for a simple medium. However, we used numerical analysis and equivalent circuit modeling techniques to analyze the synthesis and propagation of SAW.

2.3. SAW Excitation and Modeling

In 1965 White and Voltmer proposed and demonstrated the possibility of generating SAW by applying a time varying voltage on periodically arranged metal electrodes (called interdigital transducers, IDTs) deposited on piezoelectric materials [31]. Though piezoelectric material is required for transduction, the generated SAW can propagate in any solid material. The generated SAW will have a wavelength equal to the period of the IDT, and its frequency is determined by the acoustic velocity of the piezoelectric material. This simple, but clever, structure has become the main element of SAW devices, which have seen a wide range of applications in communication and microelectronics as signal processing units. Figure 2.1 shows a cartoon depicting the IDT structure on a piezoelectric substrate biased with a time varying voltage across its contact pads. The IDT period is designated as Λ.

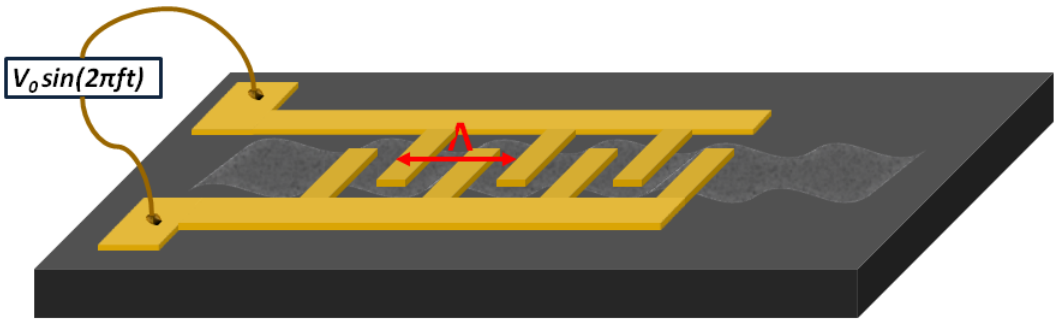

Figure 2.1 Schematic of an interdigital transducer (IDT).

For an IDT of period Λ and piezoelectric substrate acoustic velocity v_{sound}, the generated SAW will have a frequency of

$$f_{SAW} = \frac{v_{sound}}{\Lambda} = \frac{v_{sound}}{4d}, \qquad \textbf{2.16}$$

where d is the width (and spacing) of the IDT fingers. This implies that generation of high frequency SAW requires high acoustic velocity material or/and small period IDT. In this dissertation, we used state of the art nanofabrication technology to fabricate IDTs which generate SAW with frequencies over 10 GHz.

2.3.1. Equivalent Circuit Modeling of SAW Transducers

There are several analytical models that construct the properties of a SAW transducer in terms of circuit elements. One such simple model is the crossed-field model [27]. It is an extension of the Mason's equivalent circuit model that was primarily used for modeling bulk acoustic waves. The model assumes the electric field distribution under the IDT electrodes is perpendicular to the piezoelectric substrate. One limitation of the model is that it doesn't take into account SAW reflections from IDT finger electrodes. Nevertheless, its simplicity helps to extract important parameters like electromechanical coupling efficiency and IDT static capacitance from measured reflection spectra of IDTs.

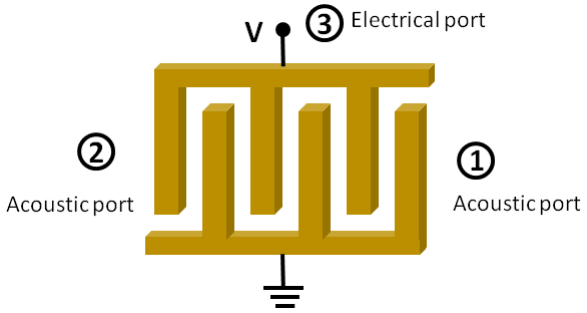

Figure 2.2 Interdigital transducer as a three port network.

As shown in the schematic of Figure 2.2 the SAW transducer can be envisaged as a three port network with one electrical port and two equivalent acoustic ports. The electrical port has a characteristic impedance that controls the current drawn by the IDT from a source. A 3×3 admittance matrix can characterize the current voltage relationship for the network. Of the 9 matrix elements, Y_{33} is the relevant one as it characterizes the electrical admittance of the IDT and is the quantity that can be directly probed during S_{11} measurement. The cross-field model predicts the admittance to have the form [32]:

$$Y_{33}(\omega) = G_a(\omega) + j\left[\omega C_T + B_a(\omega)\right] \qquad \textbf{2.17}$$

Here $G_a(\omega)$ and $B_a(\omega)$ are the IDT conductance and susceptance which vary with frequency as

$$G_a(\omega) = \frac{4}{\pi} N\kappa^2 C_T \omega_o \left| \frac{\sin(N\pi(\omega-\omega_o)/\omega_o)}{N\pi(\omega-\omega_o)/\omega_o} \right|^2 \qquad \textbf{2.18}$$

$$B_a(\omega) = \frac{4}{\pi} N\kappa^2 C_T \omega_o \left| \frac{\sin(2N\pi(\omega-\omega_o)/\omega_o) - (2N\pi(\omega-\omega_o)/} {2\left[N\pi(\omega-\omega_o)/\omega_o\right]^2} \right| \qquad \textbf{2.19}$$

where κ^2, C_T and ω_o are the piezoelectric material electromagnetic coupling coefficient, the IDT static capacitance and resonance angular frequency of the IDT respectively. Using these expressions, the IDT equivalent circuit can be drawn as a shunt circuit in series with a parasitic resistance R_n as shown in Figure 2.3. We used this model to extract the electromechanical coupling efficiency of the SAW devices realized in this thesis.

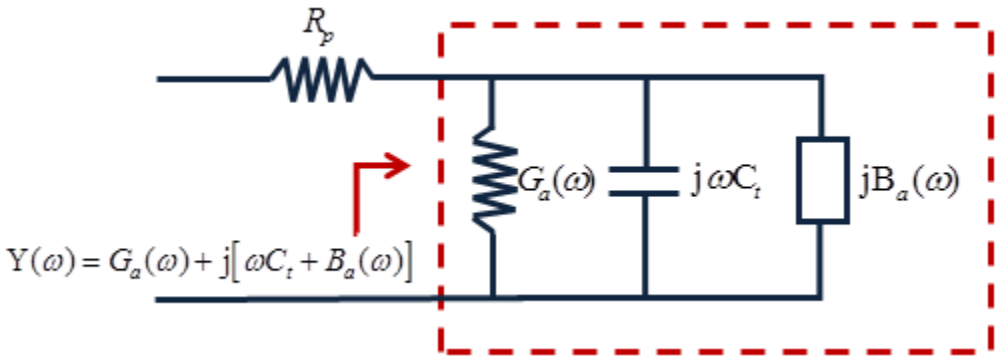

Figure 2.3 Interdigital transducer equivalent circuit.

2.3.2. Finite Element Method (FEM) Analysis of SAW Transducers

Several analytical methods are available to model and approximately characterize generation and propagation of SAW in piezoelectric and elastic materials. Coupling of modes (COM) analysis, equivalent circuit models, or delta function model are a few examples to mention [33]. However, a more accurate and detailed analysis can be obtained using rigorous analytical schemes like finite element method (FEM) and finite difference time domain (FDTD) methods. In this work, a FEM simulation scheme was employed to study the generation and propagation of SAW on piezoelectric substrate. The FEM simulation results were used in designing a high performance SAW devices.

FEM is a numerical technique widely used to solve boundary value problems governed by partial differential equations. It divides the problem domain into smaller parts, finite elements, and applies variational techniques to solve the problem by minimizing residual errors. There are a wide range of commercial tools that use FEM simulations to solve eigenvalue problems. In this thesis, COMSOL was used for the FEM analysis of SAW devices.

Since the IDT aperture (IDT finger length), which is the emitted SAW beam width, is orders of magnitude longer than the IDT periods, a two-dimensional analysis was done. To this end, the piezo-plane strain model of the COMSOL Multiphysics module was used. Due to the periodicity of the IDTs, only one unit cell containing a pair of IDT fingers was simulated. On the ends of the unit cell, Floquet bundary condition was imposed. The bottom layer was set mechanically fixed, while allowing the top boundary to vibrate freely. The structure was meshed to appropriate mesh sizes to increase the accuracy of the simulation. The simulation calculates the eigen frequencies and the corresponding field vectors such as displacement field, strain field, and electric potential. A simulation result for a typical SAW device is shown in Table 2-2.

2.4. Implementation of SAW Devices on Aluminum Nitride

2.4.1. Material System

The material choice in this dissertation was made taking into account piezoelectric and optical properties, fabrication compatibility with CMOS processes, and availability of wafers from foundries. The most common SAW and BAW devices were based on bulk single crystalline piezoelectric materials like quartz, LiNbO3, and LiTaO3. But, the advent of sophisticated deposition techniques and thin film technologies has enabled the realization of SAW devices based on polycystalline piezoelectric thin films like aluminum nitride (AlN), and zincoxide (ZnO). We chose aluminum nitride (AlN) as it combines good piezoelectric and optical properties, and is readily available from foundries. The material system is 330nm thick c-axis oriented polycrystalline aluminum nitride film sputter deposited on oxidized silicon wafer. The oxide thickness is 3 μm.

Aluminum nitride is a semiconducting material that has a wide band gap of 6.2eV and infrared dielectric constant 4.77. It has a wurtzite crystalline structure with lattice constants of 3.112 Å and 4.982 Å in the in-plane and out of plane directions respectively [34]. Table 2-1 shows the form and values of AlN piezoelectric, stiffness, and elasto-optic coefficient values. These values were used in the simulation, design, and analysis of the SAW device and photonic resonators.

Table 2-1 Aluminum nitride material constants [34]**.**

Piezoelectric constant	Stiffness constant	Elasto-optic constant
$\begin{bmatrix} 0 & 0 & 0 & 0 & e_{15} & 0 \\ 0 & 0 & 0 & e_{15} & 0 & 0 \\ e_{13} & e_{13} & e_{33} & 0 & 0 & 0 \end{bmatrix}$	$\begin{bmatrix} C_{11} & C_{12} & C_{13} & 0 & 0 & 0 \\ C_{12} & C_{11} & C_{13} & 0 & 0 & 0 \\ C_{13} & C_{13} & C_{33} & 0 & 0 & 0 \\ 0 & 0 & 0 & C_{44} & 0 & 0 \\ 0 & 0 & 0 & 0 & C_{44} & 0 \\ 0 & 0 & 0 & 0 & 0 & C_{66} \end{bmatrix}$	$\begin{bmatrix} p_{11} & p_{12} & p_{13} & 0 & 0 & 0 \\ p_{12} & p_{11} & p_{13} & 0 & 0 & 0 \\ p_{31} & p_{31} & p_{33} & 0 & 0 & 0 \\ 0 & 0 & 0 & p_{44} & 0 & 0 \\ 0 & 0 & 0 & 0 & p_{44} & 0 \\ 0 & 0 & 0 & 0 & 0 & p_{66} \end{bmatrix}$
e_{15} = -0.33; e_{13} = -0.38; e_{33} = 1.26;	C_{11}=410; C_{12}=149; C_{13}=99; C_{33}=389; C_{44}=125.	p_{11} = –0.1; p_{12} = –0.027; p_{13} = –0.019; p_{33} = –0.107; p_{44} = –0.032; p_{66} = –0.037

2.4.2. SAW Transducer Design

FEM simulation, as discussed above, was done to calculate the eigenmodes for an IDT period of 4.0 μm. Table 2-2 shows the out-of-plane displacement field distribution of the eigenvalues calculated. Three Rayleigh modes were identified, which were named as R-1, R-2 and R-3 modes. For the first order Rayleigh mode, the amplitude decreases exponentially into the substrate. But, the presence of AlN/SiO_2 boundary creates higher order modes that satisfy the vertical boundary conditions. As will be shown in chapter 3,

as the period of the IDT increases for a fixed AlN thickness, the number of Rayleigh modes supported by the structure increases.

Table 2-2 Calculated mode profile of 4.0 μm SAW transducer.

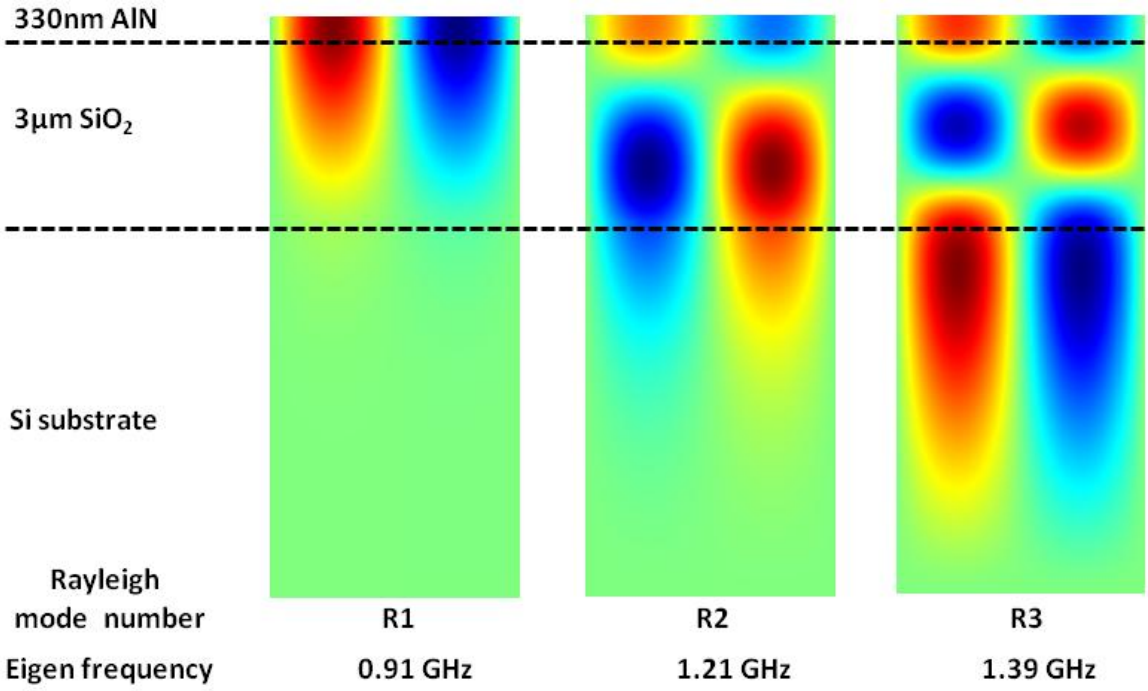

2.4.3. SAW Transducer Fabrication

We used a metal liftoff process to fabricate the SAW transducers. Figure 2.4 summarizes basic steps of the fabrication process. The AlN wafer was diced into square pieces of width 1 cm. The substrate was thoroughly cleaned by soaking in organic solvents and rinsing in a running deionized water. It was then dried using N2 gas dry blow, and baked for 5 minutes on a hot plate with surface temperature set at 180^{o}C. Electron beam lithography was used to pattern the IDT structure using a positive tone

resist - PMMA (poly methyl methacrylate). The PMMA, with molecular mass 950K, was diluted with the solvent chlorobenzene to a concentration that would give a resist thickness of 200 nm at a spin speed of 3000 rpm. After resist coating, the AlN was baked on a hot plate of temperature 180^{o}C for 5 minutes to drive off any solvent in the resist. Vistec EBPG 5000+ electron beam lithography tool was used to write the IDT pattern on the resist. The highly packed very sensitive IDT fingers were written using a low current beam that has a beam spot size of 5nm; whereas the less sensitive large area IDT pads were written with a high current beam. This beam current combination ensures good patterning resolution with reasonable write time. After the electron beam writing, the sample was developed for 30 seconds in a 3:1 solution of methyl isobutyl ketone (MIBK) and Isopropanol alcohol (IPA). The development was followed by a 60 sec rinse in IPA. After the rinse, the sample was soaked again in the developer solution for 5 seconds to remove any resist leftover in the exposed region.

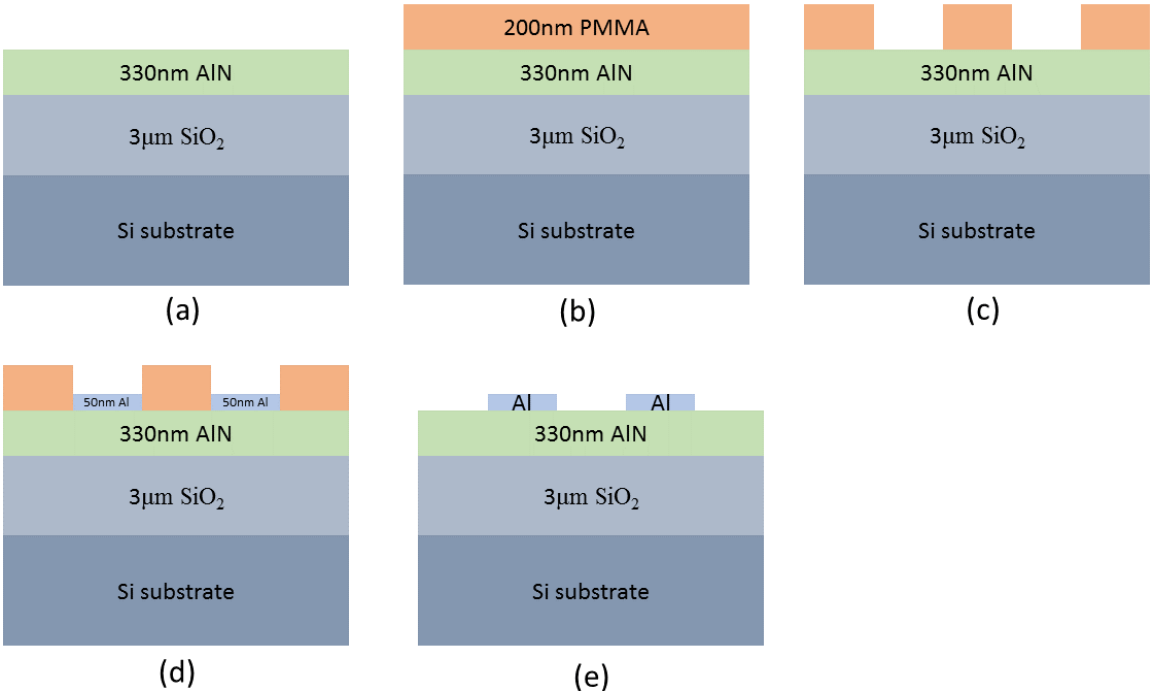

Figure 2.4 SAW transducer fabrication process flow.

a. Material system (330nm polycrystalline AlN film deposited on an oxidized Si wafer, which has an oxide thickness of 3μm). **b.** 200nm PMMA electron beam resist was deposited. **c.** Electron beam lithography was used to write the IDT pattern on the resist. **d.** 50 nm aluminum metal was deposited using electron beam evaporation. **e.** The sample was soaked in NMP to strip the resist.

In the metallization step, the CHA electron beam evaporation tool was used to deposit 50 nm aluminum metal on the sample. The evaporator chamber was pumped overnight to get a high vacuum level in the order of $4 \cdot 10^{-7}$ Torr. The metal was deposited at a rate of $0.3 A/s$. After metallization, the sample was soaked in N-methy pyrolidinone (NMP) solution for over an hour to get clean lift off. The NMP solution was kept at elevated temperature of $60^{o}C$ to facilitate resist stripping. To ensure clean liftoff, the

sample was sonicated for 5 seconds at low sonication power. Finally the sample was rinsed off with IPA and N_2 dry blown. Figure 2.5 shows an optical and scanning electron microscope image of a typical device fabricated in the experiment. The device consists of two IDTs separated by a 200 μm delay line. One of the IDTs serve as the SAW emitter whereas the other functions as SAW receiver. This structure allows us to characterize the SAW transduction as well as propagation characteristics of the AlN material system.

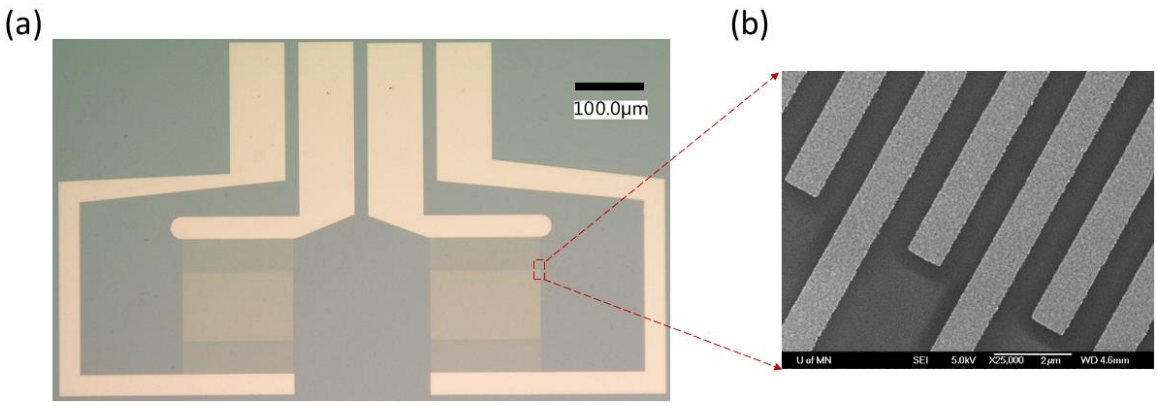

Figure 2.5 Optical and SEM image of transmitter-receiver SAW device.

a. Optical image of the fabricated transmitter-receiver SAW device. This device has two IDTs of period 4.0 μm separated by a 200 μm delay line. One IDT acts as the SAW emitter, and the other IDT serves as the SAW detector. **b.** Close-up scanning electron micrograph of the IDT fingers. The width and spacing between the IDT finger electrodes are 0.5 μm.

2.4.4. SAW Device Characterization

The SAW transducer devices were characterized by measuring the reflection spectrum for a microwave power input using a vector network analyzer (VNA). Microwave voltage from a VNA was applied to the IDT pads via a microwave picoprobe (from GGB Inc). To offset the effect of the coaxial cable and picoprobe, calibration was

done using calibration substrate (from GGB Inc) with known standards. This deembedding process moves the 50 Ω plane from the VNA port to the picoprobe tip. The input microwave power was set at 4 dBm, and the microwave frequency was swept while measuring the reflection S_{11} spectrum on the VNA. On the reflection spectrum, dips appear at frequencies matching the resonance frequency of the SAW transducer. As shown in Figure 2.6, three resonances at 0.84GHz, 1.24GHz and 1.32Ghz corresponding to R1 R2 and R3 modes respectively were measured. These resonances are in agreement with the eigen frequencies obtained from the FEM simulation result shown in Table 2-2. A close inspection of the R1 mode reveals the resonance has a line width of 0.5 MHz, which corresponds to a SAW resonance quality factor of 1700. In the polar plot, the resonance displays typical characteristics of a Lorenzian lineshape.

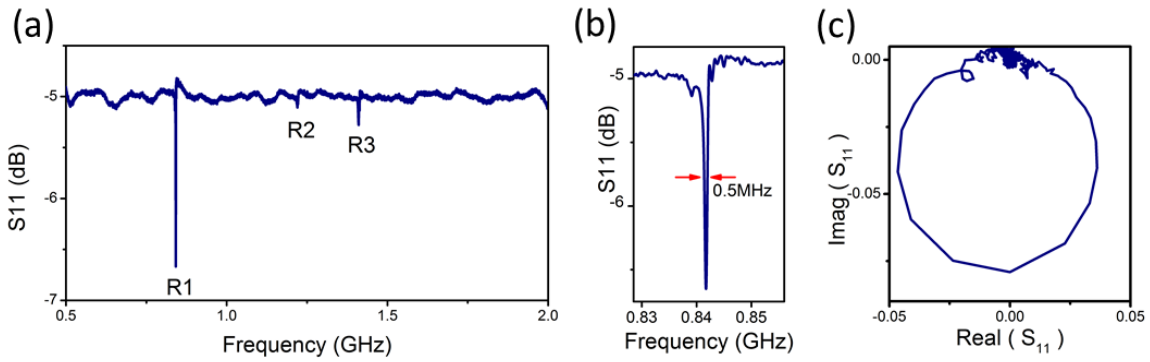

Figure 2.6 Measured reflection spectrum of the SAW transducer.

a. Measured spectra of S_{11} reflection coefficient of the fabricated 4.0 μm period IDT. The excited acoustic modes appear as dips in the spectra, which are labeled with the corresponding Rayleigh mode orders. **b.** Zoomed in S_{11} spectra of the R1 mode. **c.** Zoomed in polar plot of S_{11} spectra of the R1 mode.

We further analyzed the propagation of the SAW wave by measuring the transmission coefficient from the receiver IDT. Microwave voltage from the VNA was sent to one of the IDTs (called SAW transmitter), and voltage from the other IDT (called SAW receiver) was sent back to the VNA. On the VNA, the ratio of the received voltage to the input voltage was displayed as S_{21} coefficient. The transmission spectrum was measured by sweeping the input microwave frequency. Figure 2.7 shows the measured transmission spectrum. As expected transmission peaks were measured for frequencies matching the resonance frequencies of the three Rayleigh modes supported by the 4.0 μm IDT. The interference like pattern observed in the S_{21} spectrum inside the resonance bandwidth is due to the Fabry-Perot resonance formed between the IDTs.

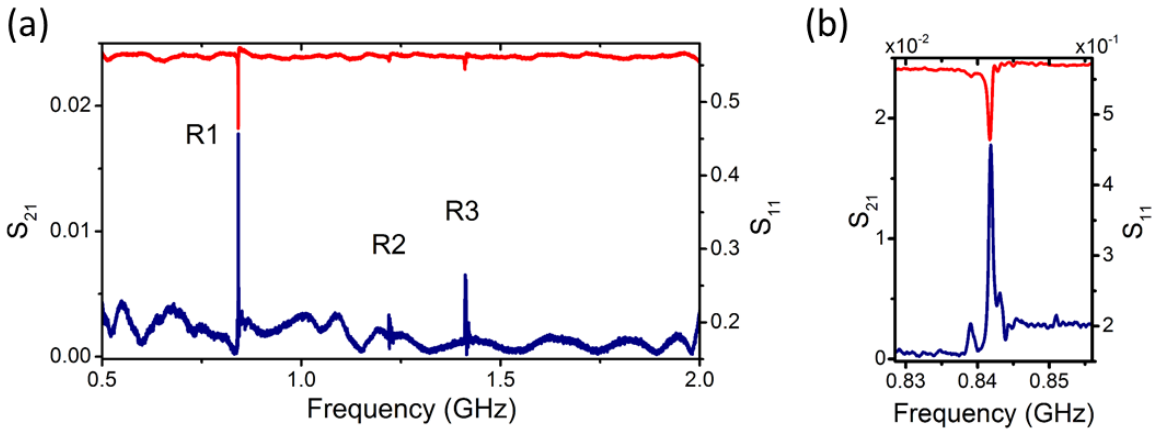

Figure 2.7 Measured transmission spectrum of the SAW transmitter-receiver device.

a. Measured spectra of S_{21} transmission coefficient of the fabricated 4.0 μm period transmitter-receiver IDTs (the blue trace is the S_{21} spectra; the red one is S_{11} spectra). The transmission spectrum shows peaks at three frequencies that correspond to the IDT resonance frequencies. **b.** Zoomed in S_{21} spectra of the R1 mode.

Chapter 3. Sub-optical Wavelength Acoustic Wave Modulation of Integrated Photonic Resonators at Microwave Frequencies [23]

Light-sound interactions have long been exploited for modulation, filtering and frequency shifting of light in various acousto-optic devices based on bulk crystalline materials. Conventionally these devices operate in megahertz frequency range where the acoustic wavelength is much longer than the optical wavelength and a long interaction length is required to attain significant coupling. With nanoscale transducers, acoustic waves with sub-optical wavelengths can now be excited to induce strong acousto-optic coupling in nanophotonic devices. Here we demonstrate microwave frequency surface acoustic wave transducers co-integrated with nanophotonic resonators on piezoelectric aluminum nitride substrates. Acousto-optic modulation of the resonance modes at above 10 GHz with the acoustic wavelength significantly below the optical wavelength is achieved. The phase and modal matching conditions in this paradigm are investigated for efficient modulation. The new acousto-optic platform can lead to novel optical devices based on nonlinear Brillouin processes and provides a direct, wideband link between optical and microwave photons for microwave photonics and potentially quantum optomechanics.

3.1. Introduction

Actively generated acoustic waves in optical materials, typically quartz, lithium niobate and tellurium dioxide, can act as a traveling phase grating to deflect incident lightwave through Bragg diffraction and shift its frequency through the Doppler effect

[35]. These mechanisms have been applied to build an important family of optical devices—acousto-optic (A/O) devices—that include modulators, frequency shifters, beam deflectors and scanners, tunable filters, spectral analyzers and Q-switches in pulsed lasers [36]. In addition to diffraction effects, nonlinear optical effects such as stimulated Brillouin scattering (SBS) and amplification, a three-wave mixing process between light and sound waves, are also in the realm of acousto-optics [37]–[40]. Conventional A/O devices based on bulk crystalline materials, however, are bulky, and their integration with highly integrated optical systems such as silicon photonics remains a challenge. Moreover, their operation frequencies are limited to megahertz range and thus insufficient for modern optical communication operating with bandwidth of many gigabits/sec. Past efforts to increase the frequency of A/O devices are hindered by the fabrication capability of acoustic transducers and the much reduced elasto-optic efficiency at higher frequencies.

To integrate acousto-optics, a new paradigm was introduced in the seventies which integrated surface acoustic wave (SAW) transducers with planar optical waveguides [27], [41]. In contrast to bulk acoustic waves, surface acoustic waves propagate on the surface of piezoelectric materials in acoustic modes confined within a depth on the order of the acoustic wavelength [42], [43]. SAW thus can have very high energy confinement and overlap with the optical modes of the planar waveguides to achieve efficient A/O modulation in a compact device. However, the highest operation frequency of such SAW based integrated A/O devices that have been achieved was still below one GHz so far [42]–[46].

With significant advances in nanofabrication, inter-digital acoustic transducers can now be readily fabricated with sub-micron linewidth to generate surface acoustic waves with ultrahigh frequency up to tens of GHz [47]–[52]. At the same time, nanophotonic waveguides and cavities with very high quality factors have been developed to confine light in sub-wavelength scale with extremely high optical power density [53], [54]. Combining above two advances, acousto-optics can enter an unprecedented regime in which the acoustic wavelength ($\Lambda=c_a/f_a$; c_a: sound velocity; f_a: acoustic frequency) can be reduced to much less than the optical wavelength λ/n (n: refractive index). In this sub-optical wavelength regime, nearly ideal mode overlapping and phase matching conditions between light and sound waves can be reached in a highly confined system to attain efficient acousto-optic interaction and induce strong nonlinear effects such as Brillouin scattering. Indeed, gigahertz surface acoustic waves have recently been used to modulate the emission of GaAs quantum dots embedded in a photonic crystal nanocavity with the modulation frequency reaching a record of 1.7 GHz [55]. The acoustic wavelength (~1.8 μm) generated in that device, however, is still many times the optical wavelength (~0.25 μm in GaAs). Here we demonstrate acoustic modulation of photonic cavities with surface acoustic wave of frequency up to 10.6 GHz. In this microwave X-band frequency range, the acoustic wavelength is reduced to less than the optical wavelength (~0.75 μm), for the first time to the best of our knowledge, reaching the sub-optical wavelength regime of integrated acousto-optics.

3.2. SAW-Optical Resonator Integrated Device Design

The proposed devices integrate both surface acoustic wave and photonic devices on 330 nm polycrystalline aluminum nitride (AlN) films sputtered on silicon wafers with 3 μm thick thermal oxide layers. Given its strong piezoelectricity, high sound velocity and high refractive index, AlN is an ideal active material for both the excitation of acoustic waves and the making of optical waveguides [56]–[58]. In the highly integrated acousto-optic devices, the wavelength Λ of ultrahigh frequency acoustic waves can be substantially smaller than the size of the optical mode in the waveguides. In this regime, the spatial overlap between the acoustic wave and the optical mode is critical to the efficiency of acousto-optic modulation and is more sophisticated than that in conventional A/O devices. Figure 3.1 (a) schematically illustrates the relative scales of the acoustic wave and the optical mode in such a regime. The acoustic wave generates a propagating strain field, tensile and compressive periodically, which modulates the phase of the optical mode by changing the refractive index through a combination of elasto-optic and electro-optical effects. As a result, the resonance frequency of the resonator is modulated which can be approximated by using the perturbation theory as [59]:

$$\frac{\Delta\omega}{\omega} \approx -\frac{\iint \Delta n(\mathbf{r})\left|E(\mathbf{r})\right|^2 d\mathbf{r}}{\iint n(\mathbf{r})\left|E(\mathbf{r})\right|^2 d\mathbf{r}} \qquad 3.1$$

where Δn is the elasto-optic change of the refractive index tensor

$$\Delta n_i = -\frac{1}{2} n_i^3 \sum_j p_{ij} S_j \quad \left(i, j = 1,2 \ldots 6 \right) \qquad 3.2$$

with p_{ij} and S_j representing the contracted effective elasto-optic coefficient tensor and the strain field tensor, respectively [60].

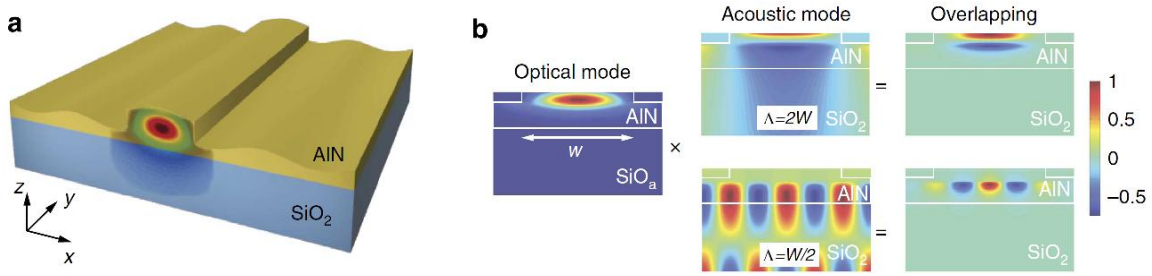

Figure 3.1 Acousto-optic modal overlap.

a. Schematics illustrating the relative scale and the interaction between the surface acoustic wave and the optical mode of the integrated waveguide made of AlN on a SiO_2 cladding layer. Overlaid on the facet of the waveguide is simulated optical mode. **b.** Numerical simulation results of the field distribution of the optical mode, the surface acoustic mode and their overlap as defined in the text for two representative situations when $\Lambda=2W$ and $\Lambda=W/2$.

Taking into account the polycrystalline nature of the AlN film and its contracted elasto-optic coefficient tensor, equation 3.1 can be reduced to a scalar expression which is proportional to an overlap factor Γ representing the spatial overlap between the strain field of the acoustic wave and the electrical field of the waveguide mode:

$$\Gamma = \frac{\iint \left[p'_{11} S_1(x,z) + p_{13} S_3(x,z) \right] \left| E_x(x,z) \right|^2 dxdz}{\iint \left| E_x(x,z) \right|^2 dxdz} \qquad 3.3$$

This overlap factor Γ determines the acousto-optic modulation efficiency. Simulation shows that Γ strongly depends on the acoustic wavelength Λ as it is reduced to be less than the waveguide width W. Figure 3.1(b) illustrates the simulated field distribution of the optical mode, the acoustic mode and their spatial overlap, which is integrated as in equation 3.3 to give Γ in two representative situations when $\Lambda=2W$ and

$\Lambda = W/2$, respectively. The simulation predicts that optimal overlap is achieved when the acoustic wavelength Λ is close to twice of the lateral size of the optical mode. In contrast, when the acoustic wavelength almost equals the mode size, the modulation by tensile and compressive strain will nearly cancel each other, leading to vanishing modulation. The situation varies periodically as Λ is continuously reduced for a given waveguide size. In the following we experimentally verify these relations in devices with varying acoustic wavelength Λ and optical waveguide width W.

Figure 3.2 shows optical and scanning electron microscopy images of a typical device, which features an inter-digital transducer (IDT) made of gold and an optical racetrack resonator made of AlN single-mode rib waveguide. Among the devices studied, the width of the waveguide is varied from 0.8 to 1.2 μm and its height is kept at 200 nm.

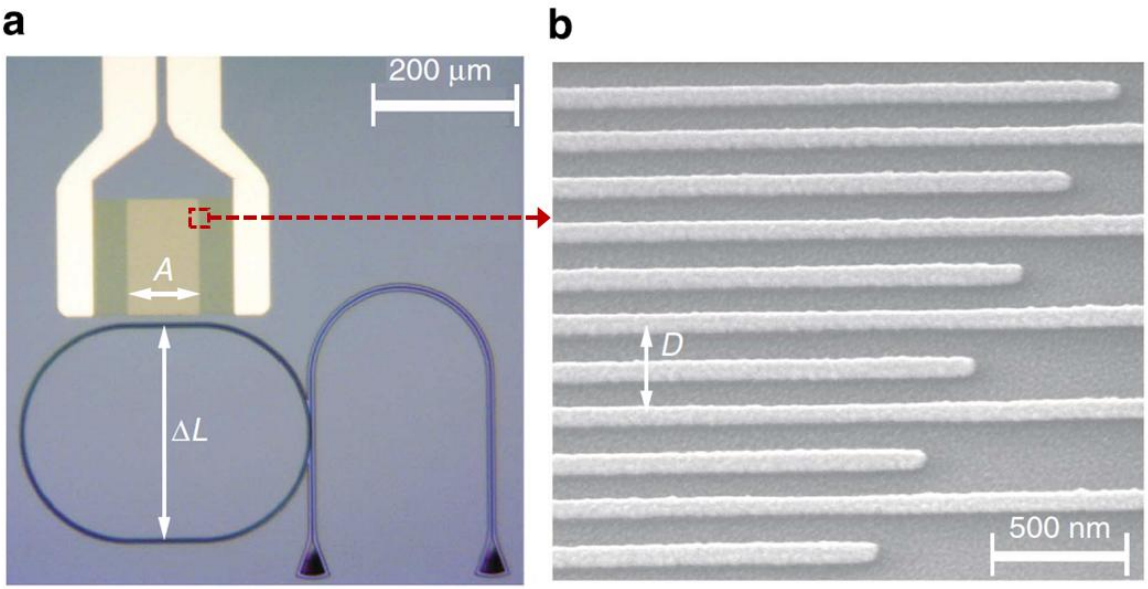

Figure 3.2 An integrated surface acousto-optic system.

a. Optical microscope image of a typical device, featuring a racetrack resonator made of AlN rib waveguide and an inter-digital transducer (IDT). The aperture size of the IDT is A and the distance between the front and back straight segments of the racetrack is ΔL as shown by the labels. **b.** Scanning electron microscope image of the electrode fingers of an IDT with a period D of 400 nm. The width of the fingers is 100 nm.

The IDTs have period D in the range of 0.4 to 1.6 μm, which corresponds to the wavelength (Λ) of the acoustic wave they excite. Figure 3.2(b) shows a zoom-in image of an IDT with D=0.4 μm; the width of each electrode finger is D/4=100 nm. The IDTs are placed to launch acoustic waves propagating in the direction transverse to the straight waveguide segments of the racetrack (Figure 3.2a), which are designed to have the same length as the aperture (A) of the IDTs in order to achieve maximal acousto-optic interaction.

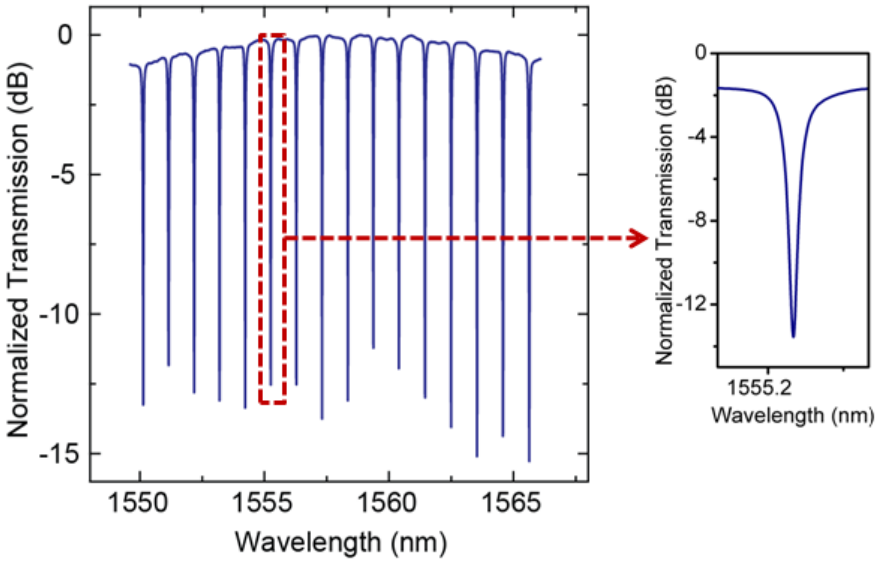

Figure 3.3 Transmission spectrum of the optical resonator.

The optical resonances of the racetrack resonator can be observed in the transmission spectrum measured from the feeding waveguide as shown in Figure 3.3. The best intrinsic optical quality factor with waveguide width of 0.8 μm is 8×10^4.

3.3. SAW Transducer Characterization

We first characterized the SAW devices by conducting microwave reflection measurements. The SAW IDT was contacted with a microwave coplanar probe and the reflection coefficient S_{11} of the device was measured with a network analyzer. In Figure 3.4a, we show a series of S_{11} parameters versus frequency measured from IDTs with Λ=1.6, 0.9, 0.7 and 0.5 μm. Acoustic modes with frequency up to 12 GHz into the microwave X-band can be observed in the reflection spectra as prominent dips. Numerical simulation confirms that these are the Rayleigh modes of different orders with the mode number *n* up to 12. They are labeled as *R*n in Figure 3.4a. It can be noted that for a given Λ, only a selective set of modes are excited and as Λ reduces, low order modes start to disappear and higher order modes begin to dominate. Simulation confirms that these are the allowable modes restricted by the boundary conditions of the AlN/SiO_2/Si multilayers.

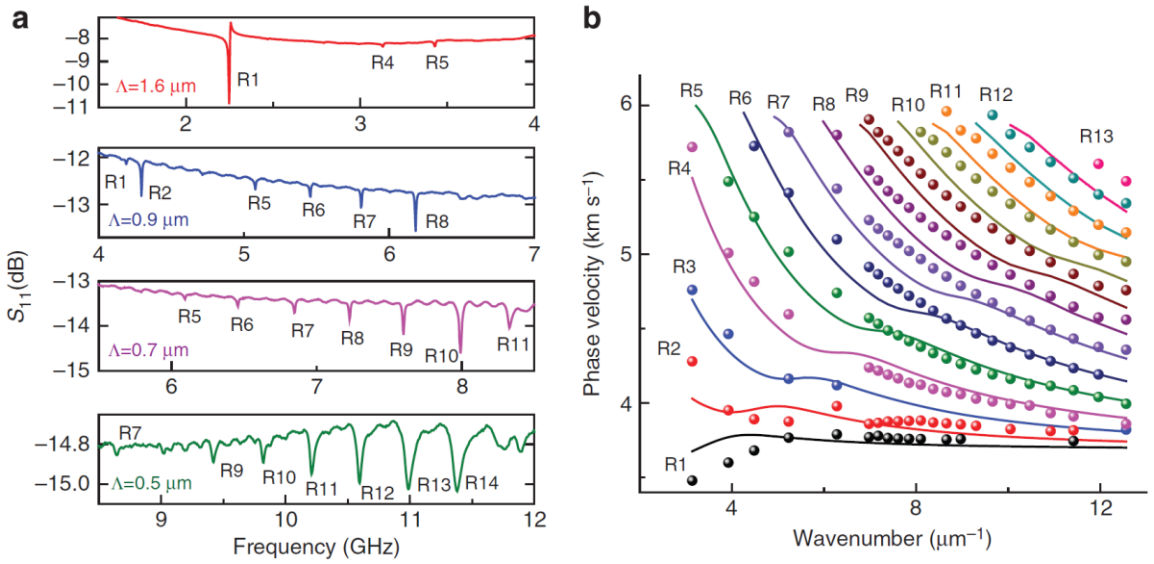

Figure 3.4 Surface acoustic wave characteristics.

a. Measured spectra of S_{11} reflection coefficient of IDTs with different wavelengths. The excited acoustic modes appear as dips in the spectra, which are labeled with the corresponding Rayleigh mode orders. **b.** Dispersion relation between the phase velocities of different Rayleigh modes and the wavenumber. Lines are simulated results and symbols are experimentally determined values.

The multilayer structure and the relatively thin AlN layer, as is necessary for making the photonic devices, also leads to strong dispersion of the acoustic waves because the modes extend over the layers with different sound velocities. Therefore, the dispersion relation between the phase velocities and the wavenumber of the acoustic waves is very important to the design of these acoustic devices. We experimentally determined the phase velocity of different modes from their frequency as $u_{\mathrm{p}} = \omega_{\mathrm{a}} / k_{\mathrm{a}}$, where ω_{a} is the angular frequency and $k_{\mathrm{a}} = 2\pi / \Lambda$ is the wavenumber of the acoustic modes. The results are displayed in Figure 3.4b along with the dispersion curves

calculated with numerical simulation. The experimental and the theoretical results show reasonable agreement with discrepancies attributed to the finite simulation space and the mass loading effect of the IDT electrodes. Because of their different mode profiles, different orders of Rayleigh modes show very distinct dispersion properties. As can be seen in Figure 3.4b, with reducing wavenumber the phase velocities of the low order modes approach the sound velocity of SiO_2 (c_{SiO2}= 3400 m/s) because the acoustic modes largely reside in the SiO_2 layer. In contrast, the phase velocities of the high order modes approach the sound velocity of AlN (c_{AlN}=6000 m/s*)* because the acoustic mode is more confined in the AlN layer.

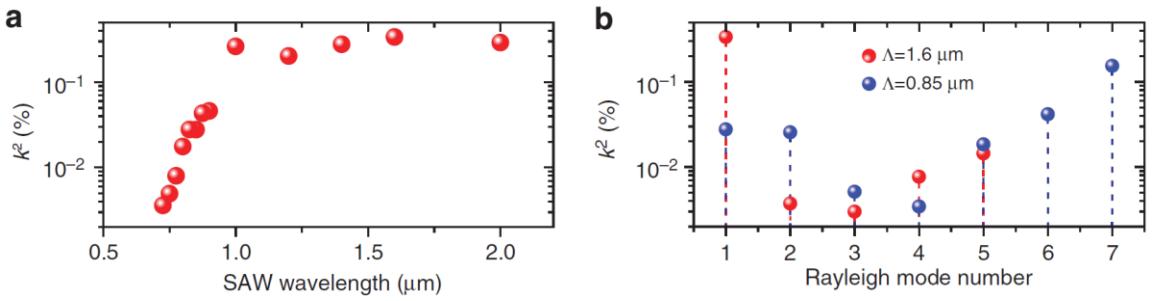

Figure 3.5 Measured electromechanical coupling efficiency.

a. Electromechanical coupling coefficient k^2 determined from the measured S_{11} reflection spectrum of the R1 modes of IDTs with various wavelengths. **b.** Electromechanical coupling coefficients of different modes of two IDT devices with Λ=1.6μm (red symbols) and 0.85μm (blue symbols).

Another important parameter of acoustic transducers is the electromechanical coupling coefficient k^2, which is defined as the ratio of the mechanical power of the acoustic wave and the input electrical power, and thus characterizes the transducers'

energy efficiency. In Fig. 2c, k^2 of the fundamental Rayleigh mode ($R1$) is plotted versus wavelength Λ, showing that at wavelength above 1 μm k^2 is around 0.4%, which is comparable with values of SAW devices made in similar thin films [61], [62]. However, when Λ is reduced to below 1 μm, k^2 decreases dramatically, making the fundamental mode more difficult to be excited as observed in Figure 3.5a. On the other hand, in Figure 3.5d the measured k^2 of different mode orders are compared for two fixed wavelengths (1.6 μM and 0.85 μm). The result reveals that at very short wavelength k^2 recovers for higher mode orders and becomes comparable with that of the fundamental mode at long wavelengths. The above results suggest that the high order modes are the dominant modes at the limit of short acoustic wavelengths (where $k_a h > 1$, h is the AlN film thickness) and advantageous in excitation efficiency and reaching ultrahigh frequency. In the following, we demonstrate ultrahigh frequency acousto-optic modulation of photonic resonators using these high order acoustic modes.

3.4. SAW Optical Resonator Modulation Experiment

To measure the acousto-optic modulation, a tunable laser is coupled into the feeding waveguide and the racetrack resonator through integrated grating couplers and the transmission out of the device is monitored with a high-speed photodetector connected to the port 2 of the network analyzer. With this configuration, the measured spectra of the transmission coefficient S_{21} reflect the frequency response of acousto-optic modulation in the system. To convert the acousto-optic phase modulation to the amplitude response of the transmitted optical signal, the input laser is detuned from the optical resonance to implement the slope detection scheme. In Figure 3.6 the results

obtained from the same set of devices as in Figure 3.4a are displayed. The width of the optical waveguide W is fixed at 0.8 μm in these devices. In the spectra of S_{21}, peaks induced by the acoustic modes with frequencies that match those in the S_{11} spectra of Figure 3.4a can be observed.

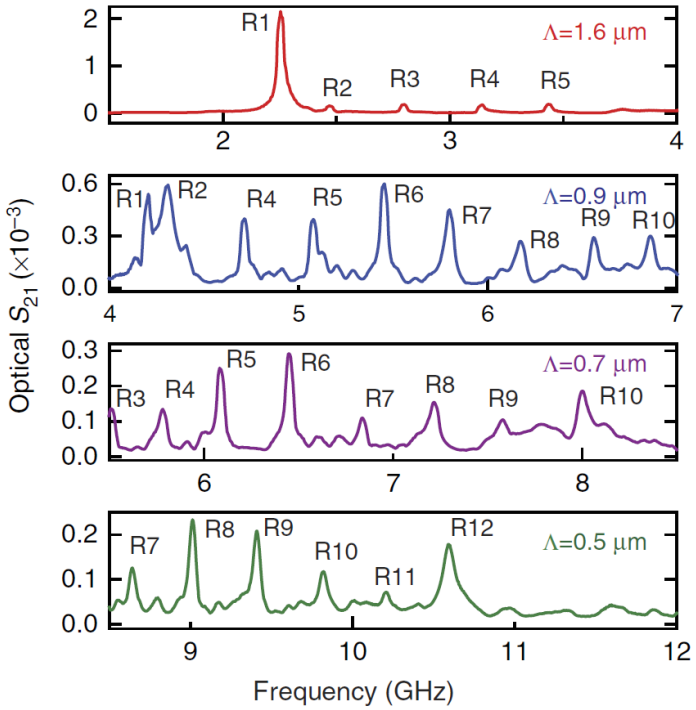

Figure 3.6 Ultrahigh frequency acoustic modulation of optical resonators.

Measured spectra of S_{21} transmission coefficient of the integrated acousto-optic devices that are the same as in Fig. 2a. Modulation of the photonic resonances shows as peaks in the spectra which are labeled with the corresponding Rayleigh mode orders. The width of the waveguide is constantly 0.8 μm in these devices.

The highest modulation frequency reaches 10.6 GHz for the 7th Rayleigh mode with acoustic wavelength Λ=0.5 μm. This demonstrated acousto-optic modulation

frequency is almost an order of magnitude higher than the previously reported result [53]. More importantly, our results represent the first demonstration of acousto-optic modulation in integrated photonic devices using acoustic waves with wavelength significantly smaller that the optical wavelength (~0.75 μm here).

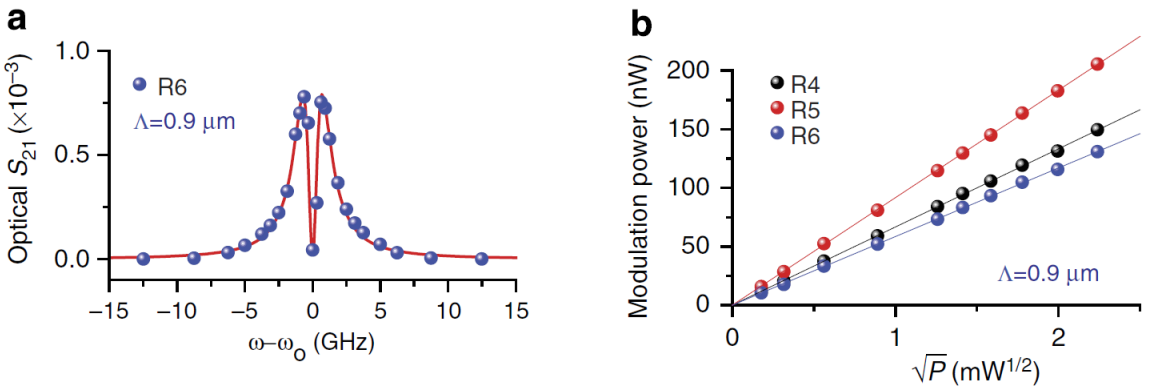

Figure 3.7 Acousto-optic modulation for different laser detuning and SAW power.

a. Acousto-optic modulation response versus laser detuning relative to the optical resonance for the R6 mode in the Λ=0.9 μm device. The response shows a line shape of the derivation of a Lorentzian resonance, indicating that the acoustic wave modulates the phase of the optical mode. **b.** Modulated optical signal power versus the square root of the input power and linear fittings for the R4, R5 and R6 modes of the Λ=0.9 μm device. The linear dependence indicates that the modulation is proportional to the amplitude of the acoustic wave.

The modulation amplitude was also measured with varying laser detuning relative to the optical resonance frequency. The result for the R6 mode of Λ=0.9 μm device is displayed in Figure 3.7a, showing that the optical S_{21} follows the derivative of a Lorentzian optical resonance lineshape, as expected from the phase modulation nature of the acousto-optic interaction. In addition, because the phase shift induced by the acousto-optic modulation is expected to be proportional to the amplitude of the acoustic wave, the

modulation amplitude should be linearly dependent on the square root of the input electrical power. This linear relation is clearly shown in Figure 3.7b, measured from three representative acoustic modes (R3, R4, R5) of the Λ=0.9 μm device. The actual input power P is calculated by taking into account the reflection coefficient of the IDT and the modulated optical power is calculated from the S_{21} coefficient after calibrating the gain and losses of all the optical and electrical elements in the setup.

3.5. Optomechanical Coupling Analysis

Comparing Figure 3.4a and Figure 3.6, it can be observed that the electrical reflection and the optical transmission measurements yield different relative amplitudes for different acoustic modes. For example, the R11 mode of the Λ=0.5 μm device is strong in the electrical S_{11} spectrum but suppressed in the optical S_{21} spectrum. It indicates that even though this mode can be efficiently excited, it does not modulate the optical mode effectively as compared with, for example, the R9 mode of the same device. This effect is attributed to the different acousto-optic overlap factors Γ for different modes, as well as their different electromechanical coupling efficiencies k^2. Γ is strongly dependent on both the acoustic wavelength Λ and the perpendicular mode profile of the acoustic mode (Figure 3.1b) for a given optical waveguide size. As Λ is reduced to below the optical wavelength, the strain field across the optical mode can no longer be approximated as uniform but rather is spatially periodic as illustrated in Figure 3.1.

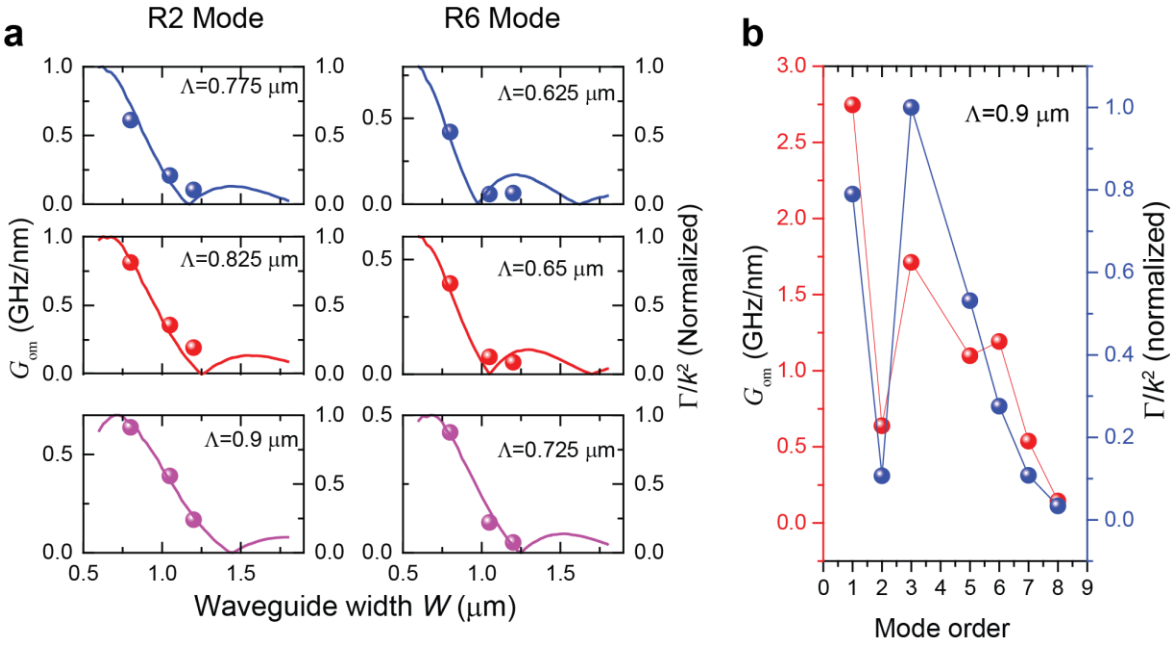

Figure 3.8 Optomechanical coupling rate and acousto-optic modal overlap.

a. Measured optomechanical coupling coefficient G_{om} and theoretically calculated overlap factor Γ of the acoustic and the optical modes after normalization by the electromechanical coupling coefficient k^2, for the R2 and R6 modes of devices with varying acoustic wavelength Λ. Note the experimental (symbols) and the theoretical results (lines) use different scales but qualitatively they agree very well. **b.** Measured G_{om} (red symbols) and theoretically calculated Γ/k^2 (blue symbols) of all the acoustic mode for the device with Λ=0.9 μm.

Therefore to evaluate the optomechanical modulation of the optical resonance, Γ has to be calculated for each given acoustic wavelength and optical waveguide size. To be consistent with other types of optomechanical systems, we define the opto-mechanical coupling coefficient $G_{om} = \Delta\omega/\Delta z$ as the ratio of the optical resonance frequency shift to the displacement amplitude (Δz) of the acoustic wave. G_{om} describes the efficiency of acousto-optic modulation in a specific device and can be determined experimentally. The

representative results of G_{om} for the second (R2) and the sixth (R6) Rayleigh modes measured from eighteen devices with different Λ and waveguide widths (W=0.8μm, 1.05μm and 1.2μm) are shown as symbols in Figure 3.8a. For comparison, the calculated overlap factors divided by k^2 to compensate for the different electromechanical coupling efficiencies are also plotted after being normalized. Qualitative agreement between the theory and the experiment can be observed. The results show that G_{om} reaches maximal value when W is smaller than the acoustic wavelength Λ and the effective width of the optical mode is close to $\Gamma/2$. In contrast, as W increases above Λ, G_{om} first decreases and then oscillates when the overlap integral changes periodically. Thus, to achieve efficient acousto-optical modulation, the optical waveguide width needs to be optimally designed to utilize a specific acoustic mode. In addition to the lateral modal overlap, the acousto-optic overlap in the vertical direction, which depends strongly on the mode orders, also plays an important role. In Figure 3.8b, we show the measured G_{om} of different acoustic modes in a Λ=0.9μm, W=0.8 μm device along with theoretical results. The experimental results agrees well with the theoretical prediction to show that at this particular wavelength, the fundamental and the third order modes are the most efficient in acousto-optical modulation but the third order mode can modulate at higher frequency with similar efficiency. As shown in Figure 3.5b, when the acoustic wavelength is further reduced, the higher order modes can be more efficient and thus more desirable for ultrahigh frequency modulation.

3.6. Broadband SAW Modulation of Optical Resonator

An important application of SAW devices is for front-end bandpass filters in wireless communication systems which often requires a wide passband width [27]. A wideband SAW transducer can be achieved with a slanted IDT design in which the period of IDT electrodes is varied linearly to generate SAW wave with frequencies spanning between the frequencies that correspond to the periods at the two ends of the IDT [63], [64]. To demonstrate broadband acousto-optic modulation, we designed a slanted IDT with a center period of 4μm (corresponding center frequency: 0.9 GHz) and 20% bandwidth. The acousto-optic modulation response of the device is shown in Fig. 5a. The modulation result demonstrates a -3dB bandwidth of 130 MHz and a side-lobe rejection ratio of over 30dB.

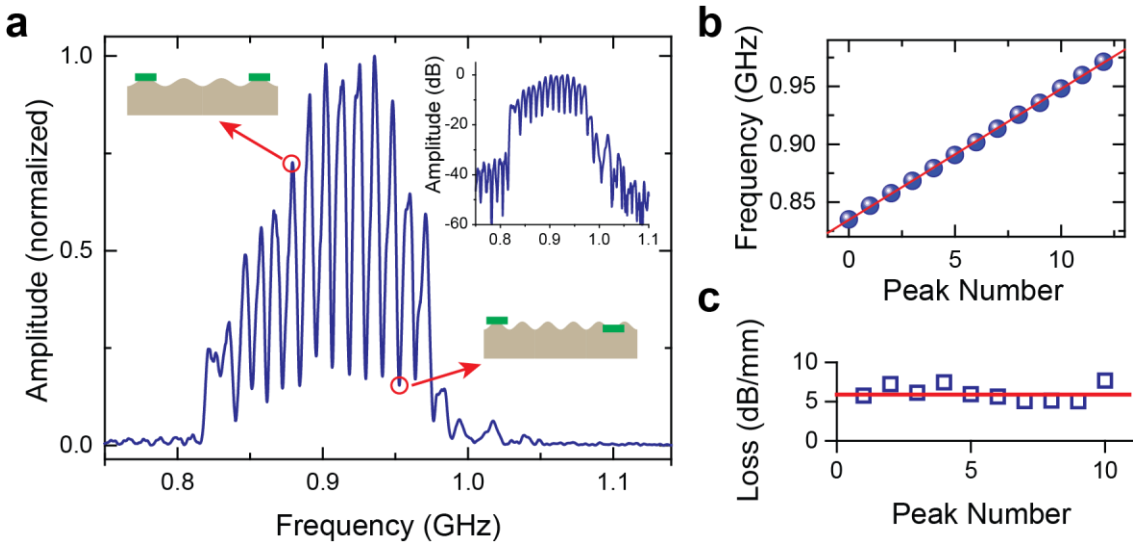

Figure 3.9 Broadband acousto-optic modulation.

a. Frequency response of the optical signal to broadband acoustic modulation generated by a slanted IDT with a center period of 4 μm. The -3 dB bandwidth of the modulation is 130 MHz

and the stopband rejection ratio is higher than 30 dB (upper-right inset). Strong ripples seen in the passband can be attributed to the delay of the acoustic wave at the front and back waveguide segments of the racetrack resonator (upper-left and lower-right insets) the interference of the modulation. **b.** The frequencies of the peaks in the passband ripples increase linearly with the peak number. Linear fitting yields the phase velocity of 3400 m/s for the fundamental Rayleigh mode, in agreement with previous results. **c.** From the extinction ratio of the ripple, the propagation loss of the acoustic wave can be estimated. The result suggests a loss of 6 dB/mm, which should be considered as an upper bound of the loss.

In the passband, however, strong passband ripples can be observed. These ripples are attributed to the phase delay between the modulation at the back and front straight segments of the racetrack due to the propagation of acoustic wave. As illustrated in Figure 3.9a, the peak modulation amplitude occurs when the phase delay $\Delta\phi = 2\pi f \Delta L/u_p$, where ΔL=300 μm is the distance between the waveguides, u_p is the phase velocity, equals $2N\pi$ (N, an integer) and thus the modulations at the two waveguide segments are in phase. Therefore, the frequencies at the peaks of the passband ripples are related to the phase velocity of the acoustic wave as $f_N = N u_p/\Delta L$. Linear fitting of the measurement result as shown in Figure 3.9b yields a phase velocity value of 3400 km/s, which agrees well with the result for the R1 mode of the same acoustic wavelength (Figure 3.4b). In addition to phase velocity, the broadband result can also reveal the propagation loss of the acoustic wave. Similar to other types of delay line interferometers, the extinction ratio η, defined as the ratio of the maximum and the minimum of the ripples, is related to the amplitude propagation loss α by $\exp(-\alpha\,\Delta L) = (\eta - 1)/(\eta + 1)$. The result of α determined with this method is shown in Figure 3.9c. An average value of 6 dB/mm is obtained, which should be considered as an

upper bound estimation of the propagation loss because effects such as the reflection of the acoustic wave by the waveguide are not considered in the calculation. With this apparently high value of linear loss [65], [66], the total acoustic loss, however, is insignificant considering that the footprint of photonic devices typically spans only a few tens of micrometers. Although the interference effect can be utilized to enhance acousto-optic modulation at a specific frequency, the large passband ripples are undesirable for signal processing applications. They can be easily removed by including an acoustic absorber in the center of the racetrack resonator to allow only the front waveguide segment to be modulated. Further optimization of the slanted IDT design can be done to improve its passband width, shape factor and stopband suppression so the device may be applied as an efficient broadband filter in radio-frequency photonics systems. Broadband IDT using Fourier synthesized design can also be used to generate sharp SAW pulses in a scheme which recently has been proposed as an ultrafast way to modulate quantum dots in photonic nanocavities for quantum photonics [67].

3.7. Summary

In conclusion, acousto-optic modulation of photonic resonators with surface acoustic wave at frequencies above 10 GHz has been demonstrated. The acousto-optic system is completely integrated on piezoelectric AlN film deposited on silicon based substrate so it is potentially compatible with the silicon photonics platform. With the achieved ultrahigh acoustic frequency, an unprecedented sub-optical wavelength regime of acousto-optics is reached. In this regime, the efficiency of light-sound interaction depends strongly on the modal and phase matching between the acoustic and optical

modes, and can be optimized with proper device design to achieve optimal modulation efficiency and ultrahigh modulation frequency. On this highly integrated acousto-optic platform, we expect that a wide range of novel device applications may be developed, including ultrafast optical modulators, non-reciprocal photonic devices based on Brillouin scattering [68]–[70] and side-band resolved cavity optomechanics utilizing actively excited travelling acoustic waves [71]–[73].

3.8. Methods

3.8.1. Device Fabrication

The integrated surface acousto-optic devices were fabricated on 330nm thick c-axis oriented polycrystalline piezoelectric AlN thin film sputtered (by OEM Group, AZ) on silicon wafers with a 3μm thermally grown oxide layer. The photonics layer was patterned with electron beam lithography (Vistec EBPG-5000+) using ZEP-520 resist and etched with Cl_2 based reactive ion etching. The AlN rib waveguides were etched 200nm deep with 130nm thick slabs. The slab allows the acoustic wave to propagate across the waveguide with reduced reflection and transmission loss. The IDTs to excite SAW were patterned with electron beam lithography using ZEP-520 resist followed by deposition of 40nm thick chrome/gold film and a liftoff process.

3.8.2. Measurement Methods

The racetrack resonator was characterized by measuring the transmission using a tunable diode laser (Agilent 81940A). The SAW IDTs were characterized with a PNA vector network analyzer (Agilent E8362B) via a microwave probe and measuring the

corresponding S_{11} reflection spectrum. Frequency response in both magnitude and phase were recorded in order to determine the electromechanical coupling efficiency of the devices. This measurement was performed on a spectrum of SAW devices of varying wavelengths to determine the dispersion relation of the devices. Before every measurement, a calibration substrate (GGB Inc.) was used to calibrate and null off the impedance of the cables and the microwave probes. Acousto-optic modulation was measured with the slope detection scheme with the laser wavelength detuned from the optical resonance. The optical signal from the device was first amplified by an erbium doped fiber amplifier (EDFA) and then filtered with a tunable optical filter to remove amplified spontaneous emission noise induced by the EDFA. Finally the signal was sent to a high speed photoreceiver (12 GHz bandwidth, New Focus 1554A). The photoreciever output was amplified using a low noise amplifier and then connected to the vector network analyzer to measure the optical S_{21} frequency response when the network analyzer source frequency was swept.

3.8.3. Electromechanical Coupling Coefficient Extraction

To extract the electromechanical coupling coefficient from the S_{11} spectra of the SAW devices, we used the equivalent circuit model discussed in chapter 2 of this thesis.

After measuring the complex impedance of the IDT using the network analyzer, we subtracted the real component values that lie well outside the SAW resonance linewidth. This subtracted frequency independent resistance corresponds to the parasitic resistance, R_p. The inverse of the remaining impedance gives the IDT admittance, $Y_a(f)$, whose real part is the IDT radiation conductance and its imaginary part comprising the

radiation susceptance and the susceptance contribution of the IDT electrodes' static capacitance. Since the radiation susceptance should vanish at the resonant SAW frequency, the susceptance value at this frequency gives the static capacitance of the IDT electrodes. This value, together with the radiation conductance value at the resonance SAW frequency, can be used to calculate the electromechanical coupling coefficient. Such analysis is done for R1 modes of IDTs of different SAW wavelengths and the results are shown in Figure 3.5a.

As an example, we presented the analysis we did on an R1 mode of a 1.6μm IDT, the S_{11} spectra of which is shown in Figure 3.4a. We calculated k^2 and C_t to be 0.27% and 2.81pF, respectively.

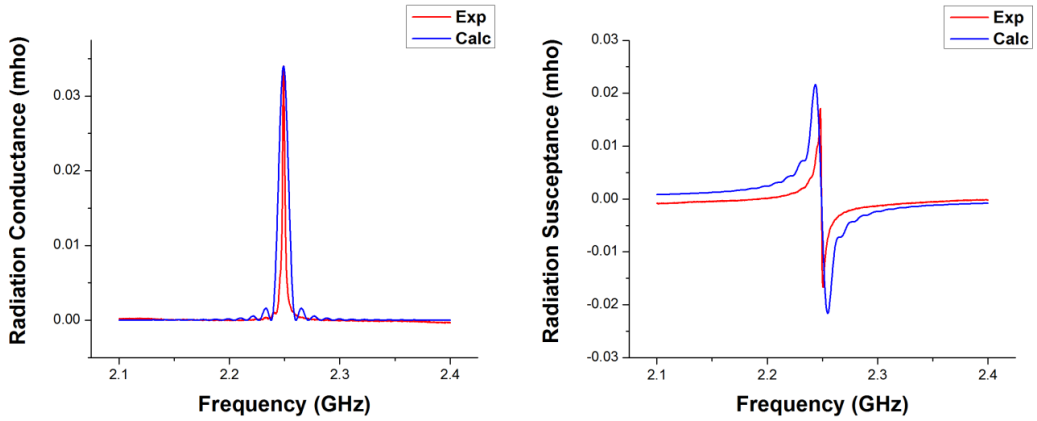

Figure 3.10 Radiation conductance and susceptance of 1.6μm period IDT.

We used these extracted values to calculate the radiation conductance and susceptance of the IDT. Figure 3.10 shows a comparison of the calculated and measured values. In the

calculated plot of the radiation conductance, the sinc function behavior is a signature of the finite size of the IDT transducer.

3.8.4. Acousto-Optic Overlap Factor Definition and Calculation:

We consider a TE waveguide mode with its dominant electric field pointing in the x-direction. The wave propagates along the *y*-axis and the *z*-axis pointing out of the plane along the *c*-axis of the AlN polycrystalline film. A travelling SAW wave modulates the dielectric constant of the material it propagates in through the elasto-optic effect directly, and electro-optic effect indirectly. The contribution of the indirect electro-optic effect can be lumped into the elasto-optic effect by defining an effective elasto-optic coefficient as [74]

$$p_{ij}^{eff} = p_{ij} - \frac{(r_{ik}l_k)(l_i e_{ij})}{(l_i \varepsilon_{ij}^S l_j)} \qquad \textbf{3.4}$$

where l_k is k^{th} component of the unit vector along the direction of SAW wave propagation, and r_{ij} represents the electro-optic coefficient, which can be written in the contracted form for crystalline material with 6mm symmetry as:

$$r_{ij} = \begin{bmatrix} 0 & 0 & r_{13} \\ 0 & 0 & r_{13} \\ 0 & 0 & r_{33} \\ 0 & r_{51} & 0 \\ r_{51} & 0 & 0 \\ 0 & 0 & 0 \end{bmatrix} \qquad \textbf{3.5}$$

with coefficiecnts r_{13}=0.67pm/V, r_{33}=-0.29pm/V, and r_{51}~0 in AlN [75]. For a SAW wave propagating along the *x*-axis (transverse to the optical waveguide), the only nonzero

electro-optic contributions comes from r_{51}. But, this value is quite small and can be ignored, leaving the elasto-optic coefficient unchanged.

Invoking the definition of index ellipsoid and using the contracted form of the elasto-optic coefficient, we can write the change in refractive index as:

$$\Delta\left(\frac{1}{n^2}\right)_i = \sum_j p_{ij} S_j \quad i, j = 1, 2, \ldots 6 \tag{3.6}$$

where p_{ij} is the elasto-optic coefficient tensor, and S_j is the strain field tensor. A simple differentiation reduces the above expression to:

$$\Delta n_i = -\frac{1}{2} n_i^3 \sum_j p_{ij} S_j \tag{3.7}$$

For a hexagonal crystal system like AlN, the elasto-optic coefficient tensor takes the form

$$p_{ij} = \begin{bmatrix} p_{11} & p_{12} & p_{13} & 0 & 0 & 0 \\ p_{12} & p_{11} & p_{13} & 0 & 0 & 0 \\ p_{31} & p_{31} & p_{33} & 0 & 0 & 0 \\ 0 & 0 & 0 & p_{44} & 0 & 0 \\ 0 & 0 & 0 & 0 & p_{44} & 0 \\ 0 & 0 & 0 & 0 & 0 & p_{66} \end{bmatrix}$$

with values $p_{11} = -0.1$, $p_{33} = -0.107$, $p_{12} = -0.027$, $p_{13} = -0.019$, $p_{44} = -0.032$, and $p_{66} = -0.037$ for AlN thin films [76]. Since the film is polycrystalline, we can approximate the in-plane elasto-optic coefficients as the average of the a- and b-direction coefficients of the crystal: $p'_{11} = p'_{12} = \left(p_{11} + p_{12}\right)/2 = -0.063$. Ignoring the shear components of the strain field tensor (S_4, S_5, S_6), which are much weaker than the normal components, one can write the elasto-optic refractive index change as:

$$\Delta n_{x,y} \approx -\frac{1}{2} n_o^3 \left(p'_{12} S_1 + p_{13} S_3 \right), \qquad \textbf{3.8}$$

where S_1 and S_3 correspond to the normal strain fields in the *x*- and *z*-directions respectively. This change in refractive index induces a change in mode frequency of the optical resonator. Since the SAW-induced refractive index change is very small ($\Delta n/n$ <<1), one can use perturbation theory to estimate this change in frequency to the first order in Δn as [59]:

$$\frac{\Delta\omega}{\omega} = -\frac{\iint \Delta n(\mathbf{r}) \left|E(\mathbf{r})\right|^2 d\mathbf{r}}{\iint n(\mathbf{r}) \left|E(\mathbf{r})\right|^2 d\mathbf{r}} \approx -\frac{\iint \Delta n(\mathrm{x,z}) \left|E_1(\mathrm{x,z})\right|^2 \mathrm{dxdz}}{\iint n(\mathrm{x,z}) \left|E_1(\mathrm{x,z})\right|^2 \mathrm{dxdz}} \qquad \textbf{3.9}$$

where E_1 is the dominant electric field of the TE mode waveguide. This implies that the change in mode frequency is proportional to an overlap integral of the SAW strain field with the waveguide mode electric field, which can be written as:

$$\Gamma = \frac{\iint \left[p'_{12} S_1(x,z) + p_{13} S_3(x,z) \right] \left|E_1(x,z)\right|^2 dxdz}{\iint \left|E_1(x,z)\right|^2 dxdz}. \qquad \textbf{3.10}$$

This overlap factor can be calculated to optimize the geometry of a waveguide for maximum SAW-optics interaction.

3.8.5. Optomechanical Coupling Coefficient Extraction

Analogous to optomechanical systems, the strength of acousto-optic interaction in an optical cavity can be quantified by an optomechanical coupling rate (G_{om}). We define this coupling rate as:

$$\Delta\omega = G_{om} < A >, \qquad \textbf{3.11}$$

where $\Delta\omega$ is the change in resonance frequency of the optical cavity due to acousto-optic modulation, and <*A*> is the mean amplitude of the SAW displacement field. This displacement field amplitude is a measure of the acoustic energy, which depends on the electromechanical coupling coefficient and the microwave power input to the IDT.

The acoustic elastic energy density is given as:

$$U = \frac{1}{2}\sum_{i,j=1}^{3} S_i C_{ij} S_j, \qquad \textbf{3.12}$$

where S_i is the strain field tensor component and C_{ij} is an element of the elastic module tensor which can be written in its reduced form as [77]

$$C = \begin{bmatrix} C_{11} & C_{12} & C_{13} & 0 & 0 & 0 \\ C_{12} & C_{11} & C_{13} & 0 & 0 & 0 \\ C_{13} & C_{13} & C_{33} & 0 & 0 & 0 \\ 0 & 0 & 0 & C_{44} & 0 & 0 \\ 0 & 0 & 0 & 0 & C_{44} & 0 \\ 0 & 0 & 0 & 0 & 0 & C_{66} \end{bmatrix},$$

with element values C_{11}=410 GPa, C_{12}=149 GPa, C_{13}=99 GPa, C_{33}=389 GPa, and C_{44}=125 GPa for AlN. The strain field vector of the surface acoustic wave propagating along the *z*-axis can be expressed as: $S = \begin{pmatrix} S_1 & 0 & S_3 & 0 & S_5 & 0 \end{pmatrix}$, where S_1 and S_3 are the normal strain fields along the *x* and *z*-directions, respectively, and S_5 is the shear strain field. Ignoring the relatively weak shear component of the strain field and taking

into account the fact that S_1 and S_3 are 90^o out of phase (where cross-terms vanish upon averaging over a SAW wavelength), the energy density reduces to:

$$U = \frac{1}{2}\left(C_{11}S_1^2 + C_{33}S_3^2\right) \approx C_{33}S_3^2, \qquad \textbf{3.13}$$

where in the last step we took the upper bound of the energy density for the case of simplicity. The *z*-component strain field can be expressed as:

$$S_3 = \frac{\partial u_z}{\partial z} = \frac{\partial}{\partial z}(Ae^{-z/\Lambda}\sin\frac{2\pi}{\Lambda}x) = -\frac{A}{\Lambda}e^{-z/\Lambda}\sin\frac{2\pi}{\Lambda}x, \qquad \textbf{3.14}$$

where the out-of-the-plane displacement u_z with amplitude A is assumed to decay exponentially at a rate of $1/\Lambda$ into the substrate for surface waves. Thus, the energy averaged over a SAW wavelength can be written as:

$$E = \iint U dxdydz = \frac{A^2W}{\Lambda^2}C_{33}\iint \mathrm{e}^{-2z/\Lambda}\sin^2\left(\frac{2\pi}{\Lambda}\mathrm{x}\right)dxdz, \qquad \textbf{3.15}$$

which integrates to

$$E = \frac{1}{4}C_{33}W < A >^2, \qquad \textbf{3.16}$$

where W is the SAW beam width and <A> represents 'average' amplitude of the SAW displacement field. The electromechanical coupling coefficient k^2 and the IDT reflection coefficient S_{11} relate the SAW wave power, P_{SAW}, to the microwave power input to the IDT, P_{in}, as:

$$P_{SAW} = (1 - |S_{11}|^2)k^2 P_{in} = Ef_o, \qquad \textbf{3.17}$$

where f_o is the SAW resonance frequency. Substituting the energy E expression into this power equation gives the approximate relation of the SAW displacement field amplitude with the microwave power input to the IDT as:

$$< A >= \sqrt{\frac{4(1-|S_{11}|^2)k^2}{C_{33}Wf_o}}\sqrt{P_{in}}. \qquad \textbf{3.18}$$

From the measurement data analysis, we determined that the frequency modulation has a linear relationship with the square root of the microwave power input to the IDT. The slope of this linear plot, coupling coefficient quantified with respect to microwave input voltage, can be converted into the optomechanical coupling rate, G_{om}, using the equation derived above.

3.8.6. SAW Mode Calculation

We employed a finite element method to calculate the eigenfrequencies of the IDT structure. The periodicity of the IDT allowed the use of only one unit cell with periodic boundary conditions set at the ends of the unit cell. Appropriate material parameters and boundary conditions were imposed and the geometry was solved for an optimally meshed IDT structure. All the possible eigen modes allowed by the geometry were calculated, and this led to the mapping of the SAW dispersion curve as shown in Fig. 2b of the main paper. The calculated strain field distribution was used in a post-processing recipe to calculate the acousto-optic overlap factor. Representative results are shown in Figure 3.8. In Table 3-1 and Table 3-2, we showed the eigen mode profiles calculated for 1.6μm and 0.5μm wavelength IDTs. The plots are shown for the out of plane displacement field.

Table 3-1 Simulated SAW mode profiles for 1.6 µm IDT.

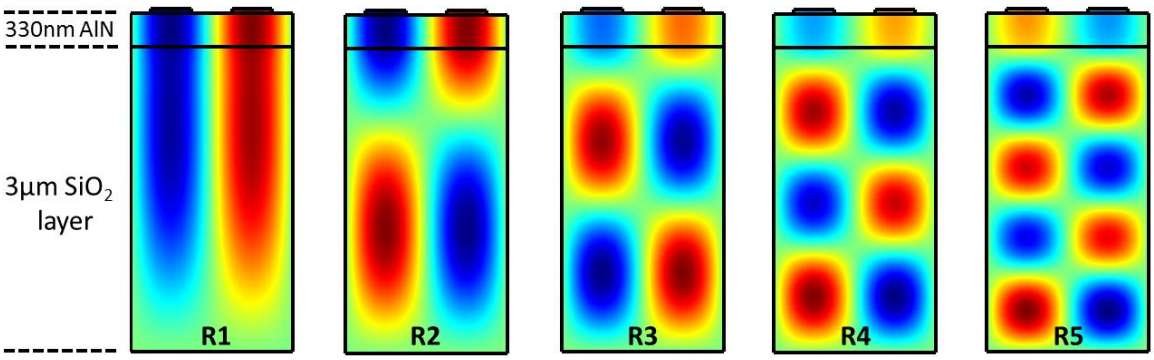

Table 3-2 Simulated SAW mode profiles for 0.5 µm IDT.

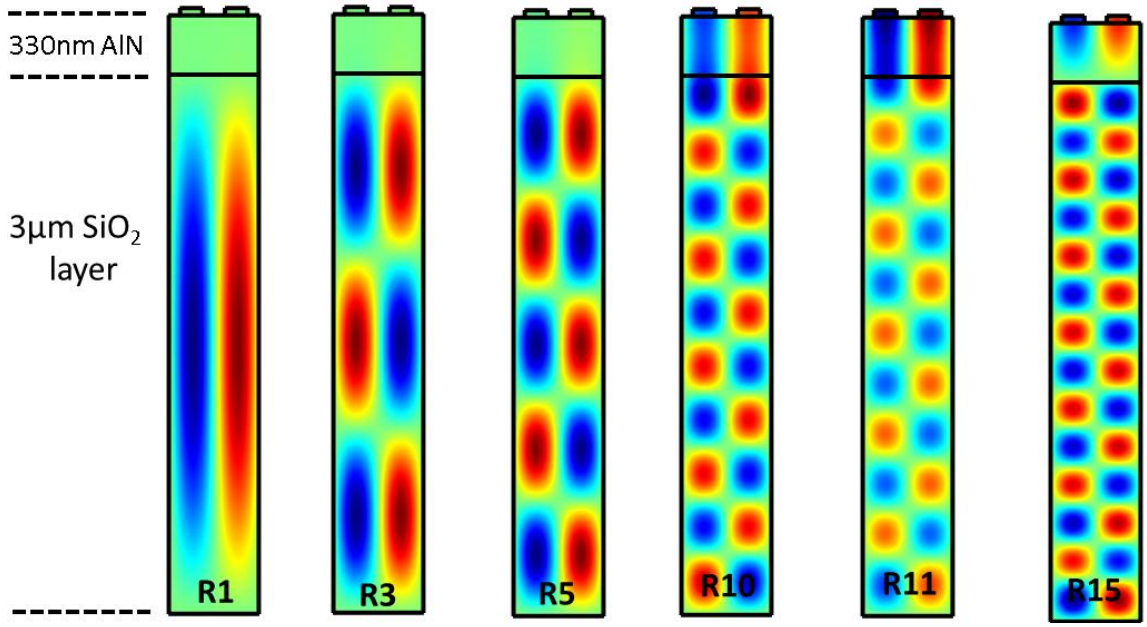

The 1.6 µm IDT supports only five modes, while the 0.5µm IDT has 15 modes. This is in line with the fact that the SAW amplitude decays exponentially into the substrate and hence limiting the number of R-modes of large wavelength IDTs to fewer than those of smaller wavelength IDTs. The AlN and silicon dioxide film thickness determines the possible number of modes supported for a particular wavelength IDT.

3.8.7. Modulation Measurement Setup

The measurement scheme is shown in Figure 3.11. A microwave signal from port-1 of the vector network analyzer was input to the IDT to excite the SAW. Laser light with wavelength set half the linewidth off the optical resonance was sent to the input grating couple. The resonator's transmitted light was collected from the output grating coupler and split into 0.1 & 0.9 ratio using a fiber coupler. The 10% output was used to monitor and optimize the fiber arrays position with respect to the grating couplers. The 90% output was sent to an erbium doped fiber amplifier (EDFA). The amplified light signal was sent to a tunable optical filter to remove any amplified spontaneous emission noise induced by the EDFA. Finally the light signal was sent to a high-speed photoreceiver for detection. The electrical signal from the detector was fed back to port-2 of the vector network analyzer and the optical S21 spectrum was measured by sweeping the network analyzer frequency.

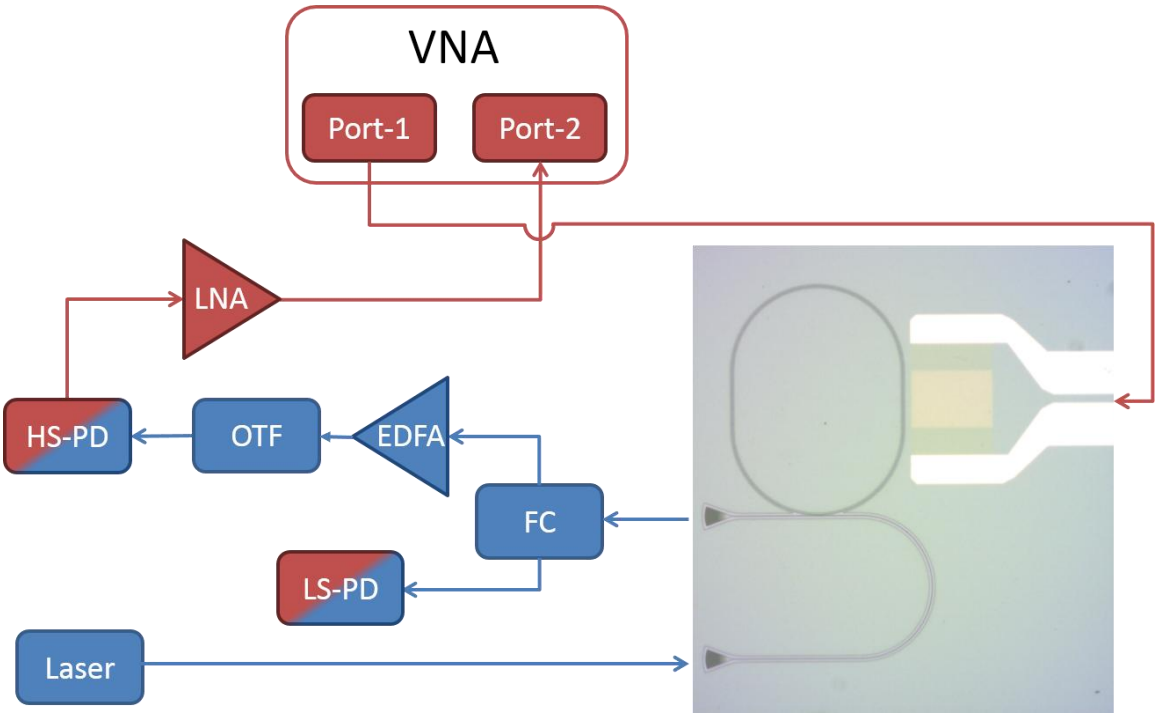

Figure 3.11 Acousto-optic modulation measurement schematics.

Modulation measurement schematics. VNA: Vector Network Analyzer, EDFA: Erbium-Doped Fiber Amplifier, OTF: Optical Tunable Filter, LS-PD: Low speed Photo Detector, HS-PD: High-speed Photo Detector, LNA: Low Noise Amplifier, FC-Fiber Coupler.

Chapter 4. Nanophotonic Cavity Optomechanics with Propagating Phonons in Microwave Ku Band [24]

Strong coherent interactions between colocalized optical and mechanical eigenmodes of various cavity optomechanical systems have been explored intensively toward quantum information processing using both photons and phonons. In contrast to localized modes, propagating mechanical waves are another form of phonons that can be guided and manipulated like photons in engineered phononic structures. Here, we demonstrate sideband-resolved coupling between multiple photonic nanocavities and propagating surface acoustic waves up to 12 GHz. Coherent and strong photon–phonon interaction is manifested with electro-optomechanically induced transparency, absorption, and amplification, and phase-coherent interaction in multiple cavities. Inside an echo chamber, it is shown that a phonon pulse can interact with an embedded nanocavity multiple times. Our device provides a scalable platform to optomechanically couple phonons and photons for microwave photonics and quantum photonics.

4.1. Introduction

Strong coherent interactions between co-localized optical and mechanical eigenmodes of various cavity optomechanical systems have been intensively explored toward quantum information processing using both photons and phonons [71], [73], [78]–[80]. To achieve this, optomechanically induced transparency [18], [19], [81], backaction cooling [82], [83] and light squeezing [84], [85] have been demonstrated. To this end, optomechanical interaction between localized mechanical modes and confined optical

modes of the cavity system is exploited to obtain strong photon-phonon coupling. In contrast to localized motion, however, the more ubiquitous form of phonons is various types of mechanical waves that freely propagate in the bulk or on the surface of solids. Propagating mechanical waves can interact with light strongly through elasto-optic effects and have been utilized in various acousto-optic devices [35], [60]. In optical fibers [38], [86]–[88] and more recently in integrated waveguides [69], [89]–[92], mechanical waves can also be optically stimulated and lead to strong Brillouin scattering between phase-matched optical modes. Much like photons, these mechanical waves, or itinerant phonons, can be confined and guided in planar phononic waveguides to propagate over long distances so that their coupling with photonic modes are highly scalable [93]–[95]. Furthermore, phononic crystals and cavities can also be implemented to confine and store phonons to achieve extended lifetime [96]–[98]. The quantum nature of those itinerant mechanical states has recently been revealed [99].

While both propagating and localized mechanical modes can be optically stimulated, they can be more efficiently excited electromechanically so that the amplitude or number of phonons can be pumped to a very high level without the need of a strong pump laser. Such an approach has been employed in electro-optomechanical systems that can directly couple microwave signals with optical signals [55], [100], [101]. Mechanical waves can also be excited with electromechanical transducers in monolithic devices. Representative types of mechanical waves include bulk acoustic waves (BAW), Rayleigh surface acoustic waves (SAW), Lamb waves and flexural plate waves. Rayleigh SAW are particularly interesting because the displacement is confined on the surface of the

substrate and it can be conveniently excited with planar transducers. Acoustic wave devices have long been applied for wireless communication and signal processing applications [27], [102]. In quantum physics, single quanta of SAW wave has been detected with single electron transistors and superconducting qubits, manifesting that propagating phonon can be a viable quantum information carrier [99], [103]. In photonics, we previously showed that microwave frequency SAW wave can efficiently modulate photonic waveguide modes [23]. In this work, we present a new type of cavity optomechanical system consisting of high-Q photonic crystal nanocavities integrated with SAW transducers working at frequency above 12 GHz, entering the microwave Ku-band. At this unprecedentedly high frequency, optomechanical interaction in the new system reaches the sideband resolved regime and enables optomechanically induced transparency and absorption. To establish the propagating feature of mechanical waves, we demonstrate phase-coherent optomechanical modulation of multiple nanocavities and that an acoustic pulse travels insides an echo chamber for multiple rounds to interact with an embedded nanocavity.

4.2. Device Design and Characterization

Both the photonic crystal nanocavities and the SAW transducers are integrated on 330 nm thick aluminum nitride (AlN) film, which provides strong piezoelectricity for efficient excitation of SAW and high refractive index for optical confinement. As illustrated in Figure 4.1, the nanocavity is formed in a nanobeam inscribed with one dimensional photonic crystal shallow etched in the AlN layer. The nanocavity can be coupled with a waveguide either on the side or at the ends. An interdigital transducer

(IDT) is configured to launch surface acoustic wave propagating in the transverse direction to the nanobeam. The aperture of the IDT (100 μm) is designed to be much larger than the mode size of the nanocavity with 24 μm full-width at the half-maximum (FWHM) of the Gaussian intensity profile, as seen in Figure 4.1b.

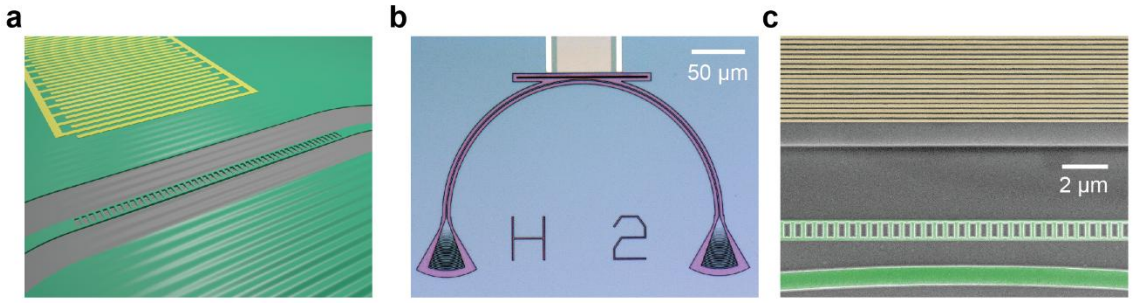

Figure 4.1 Planar integrated photonic crystal nanocavity and microwave frequency SAW wave transducer on AlN film.

a) 3D illustration of the device configuration, featuring the interdigital transducer and the excited SAW wave propagating in the transverse direction to the nanobeam photonic crystal nanocavity. **b)** Optical microscope image of a device. The nanocavity is side-coupled to a waveguide connected with two grating couplers. **c)** Scanning electron microscope image of the nanobeam cavity (green) and the IDT (yellow). The linewidth of the IDT figures is 112.5 nm.

Therefore the nanocavity undergoes approximately uniform deformation when the acoustic wave passes. The wavelength of the acoustic wave that is excited is determined by the period of the IDT transducer while the frequencies of the modes are strongly dependent on their dispersion properties in the multilayer substrate. The scanning electron microscope image in Figure 4.1c shows the IDT electrodes with period of 450 nm and linewidth of 112.5 nm. To achieve high optical quality factor and strong

optomechanical interaction, we optimized the photonic crystal nanocavity design such that the electric field of the fundamental dielectric mode [104] is well confined inside the AlN structures with an effective mode index of $n_{eff} \approx 1.54$. (The design of the photonic crystal nanocavity is discussed in the methods part of this chapter)

To characterize the photonic nanocavity, light from tunable laser is sent to the input grating coupler, and the transmitted light is collected from the output grating coupler and send to a photodetector. The photodetector response is measured while sweeping the laser light wavelength sent to the nanocavity. Figure 4.2a displays measured transmission spectrum of the nanocavity side coupled with a waveguide, showing the fundamental and the first order cavity modes as dips. The quality factor of the waveguide loaded fundamental mode is 5×10^4, corresponding to a linewidth of $\kappa=(2\pi)\cdot3.88$ GHz (Figure 4.2b).

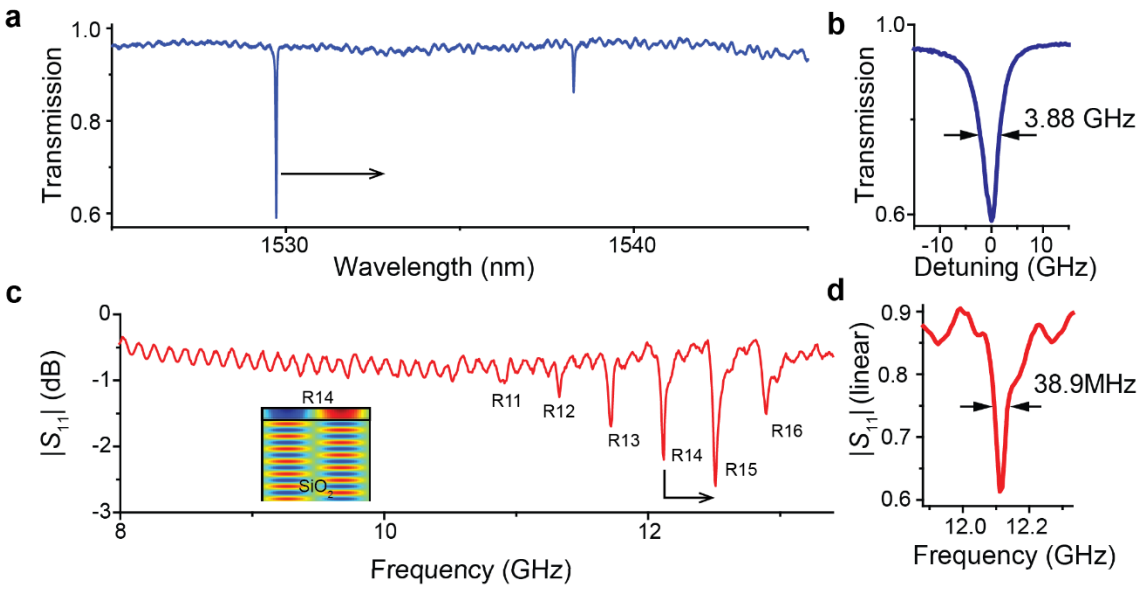

Figure 4.2 Photonic nanocavity and SAW wave tarnsducer device characteristics.

a. Transmission spectrum measured from the nanocavity showing the fundamental (at 1529.7 nm) and the first order (at 1538.3 nm) resonance modes. **b.** Zoom-in of the fundamental resonance of the nanocavity, showing a linewidth of 3.88 GHz. **c.** Spectrum of de-embedded and normalized reflection coefficient S_{11} of the SAW IDT. High order Rayleigh modes from R11 to R16 can be observed as resonance dips. Inset: Simulated displacement field of R14 mode, showing the displacement is more confined in the top AlN layer. **d.** Zoom-in of the normalized S_{11} spectrum of R14 mode plotted in linear scale, showing a linewidth of 38.9 MHz.

To characterize the SAW modes, reflection coefficient (S_{11}) of the IDT was measured with a vector network analyzer (VNA) and plotted in Figure 4.2c. When an acoustic wave is excited, the reflection spectrum also shows a negative peak as the microwave signal is converted to outgoing waves so less reflected. Prominent resonance peaks corresponding to high order Rayleigh modes, as marked in Fig. 1f, can be observed in the reflection spectrum. These high order modes are more interesting than the low order modes because mechanical energy is more confined in the AlN layer rather than the SiO_2 so that their overlap with the cavity optical mode is more significant, inducing stronger optomechanical coupling [23]. The inset of Figure 4.2c shows the simulated mode profile of Rayleigh mode R14, with more than 20% mechanical energy confined in the AlN layer. Its frequency is $\Omega_{14}=(2\pi)\cdot 12.1$ GHz, entering the microwave Ku band. The linewidth of the mode resonance is $\Gamma_{14}=(2\pi)\cdot 38.9$ MHz (Figure 4.2d). We note that one feature of our platform is that the electromechanical transducer is separated from the photonic cavity, allowing the mechanical frequency to be freely engineered and the photonic cavity to be optimized independently. (More simulation results of the SAW modes are included in the Methods section of this chapter.)

4.3. Sideband-resolved Optomechanical Coupling

To characterize the optomechanical coupling between the nanocavity and the SAW, a laser source, with a variable detuning from the fundamental cavity mode, was sent into the input waveguide with 22 μW power. The transmitted optical power was measured with a high-speed photodetector which was connected to the VNA and the overall system transmission coefficient S_{21} was measured as a function of the excitation frequency at the IDT. The broadband optical S_{21} spectrum is shown in Figure 4.3a.

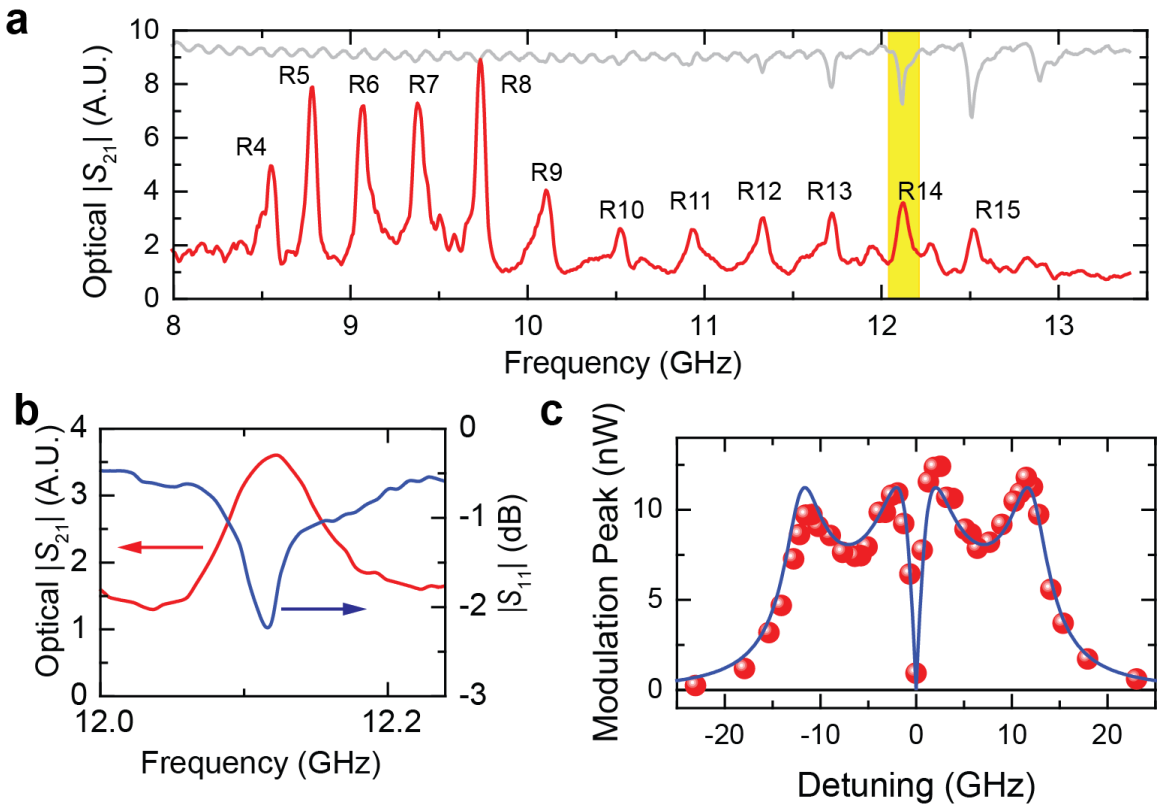

Figure 4.3 Optomechanical modulation of the nanocavity by SAW wave in sideband resolve regime.

a. Spectrum of system transmission coefficient S_{21} (red line) on a linear scale, measured using optical detection with the nanocavity and electromechanical excitation of the SAW. Rayleigh modes (R4-R10) not visible in the reflection spectrum (grey line) can be detected with high sensitivity by the nanocavity. **b.** Zoom-in of the reflection and transmission spectra of R14 mode (inside the yellow box in panel a). **c.** Amplitude (peak value) of the oscillating optical power at the S_{21} peak of R14 mode when laser detuning relative to the cavity resonance is varied. The data (red symbols) are fitted with theoretical model (blue line) of cavity optomechanical system in the sideband resolved regime.

It can be seen that in addition to the Rayleigh modes (R11−R16) observable in S_{11}, optical S_{21} also detects additional modes (R4–R10) that are not visible in the S_{11} spectrum. Comparison of the two spectra demonstrates that the high-Q nanocavity provides optical detection of acoustic waves with broader bandwidth and higher sensitivity. The amplitude of the S_{21} peaks are proportional to the modal overlaps of the Rayleigh modes with the cavity mode. Figure 4.3b shows zoom-in of the S_{11} and S_{21} of mode R14. Since the frequency of the mechanical mode ($\Omega_{12}=(2\pi)\cdot 12.1$ GHz) is considerably greater than the dissipation rate of the nanocavity mode $\kappa=(2\pi)\cdot 3.88$ GHz, their optomechanical coupling is in the sideband resolved regime, a prerequisite condition for phenomena such as induced transparency and strong coupling. Figure 4.3c shows the S_{21} peak amplitude of mode R14 as a function of varying laser-cavity detuning, displaying the characteristic lineshape of sideband resolved cavity optomechanical coupling. Fitting the results with theoretical model and calibrating the transducing factors

of the system provide the optomechanical coupling coefficient of the system, $G=(2\pi)\cdot 53$ GHz/nm, or expressed in the power of SAW, $(2\pi)\cdot 23$ MHz/$\mu W^{1/2}$.

4.4. Electro-optomechanically Induced Transparency, Absorption, and Amplification by a SAW

Coherent interaction between cavity photons and propagating phonons generates Stokes and anti-Stokes photons, which can interfere with probe photons constructively (destructively) to induce optical transparency (absorption). This three-wave nonlinear process is illustrated in the diagram of Figure 4.4a. Different from optically stimulated phonons in conventional cavity optomechanics and stimulated Brillouin scattering (SBS), here the phonons are electromechanically excited non-locally and propagating.

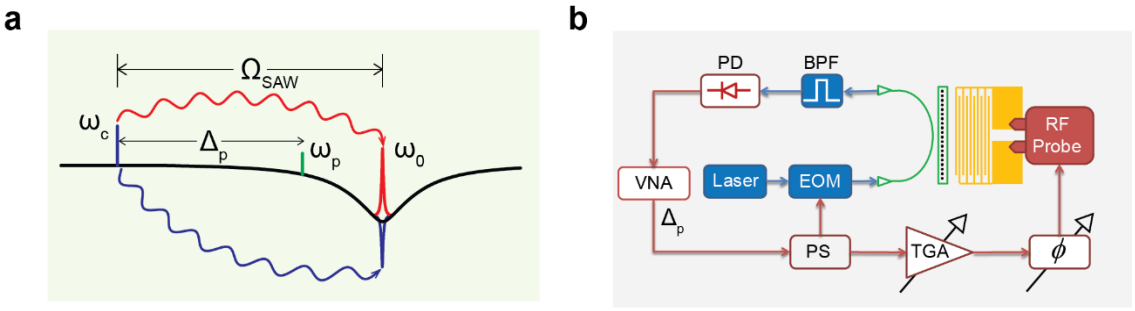

Figure 4.4 Three wave mixing process between control and probe light, and SAW.

a. Diagram illustrating the three-wave mixing process of control (ω_c), probe (ω_p) and SAW (Ω_{SAW}). The cavity resonance frequency is ω_0 with a decay rate of κ. **b.** Homodyne measurement scheme used in the experiment. The probe light is derived from the control light when it is modulated at frequency ω_p, which is scanned to obtain the transmission spectrum. (NA: network analyzer; PS: power splitter; PD: photodetector; EOM: electro-optic modulator; TGA: tunable gain amplifier; ϕ: phase shifter; BPF: band-pass filter.)

We investigate coherent photon-phonon interaction in our system using the setup depicted in Figure 4.4b. Briefly, a laser is detuned from the cavity resonance by exactly the SAW mode frequency (Ω_{SAW}) to provide the control light at frequency ω_c, and modulated with an electro-optic modulator to generate sidebands with the upper one at frequency $\omega_p=\omega_c+\Delta_p$ used as the probe light. With this scheme, the transmission spectrum of the cavity can be measured by varying the modulation frequency to scan Δ_p and detecting the beating signal between the transmitted probe light and the control light. The result is displayed as the grey symbols in Figure 4.5a showing a transmission dip which can be understood as cavity absorption. When the modulation signal is also sent to drive the IDT, a SAW wave of the same frequency is excited and propagates to the nanocavity to couple with the control light. This optomechanical coupling leads to three-wave mixing between the control, the probe and the SAW wave. Depending on the SAW phase which can be controlled with a phase shifter, the interference of waves leads to transparency or absorption.

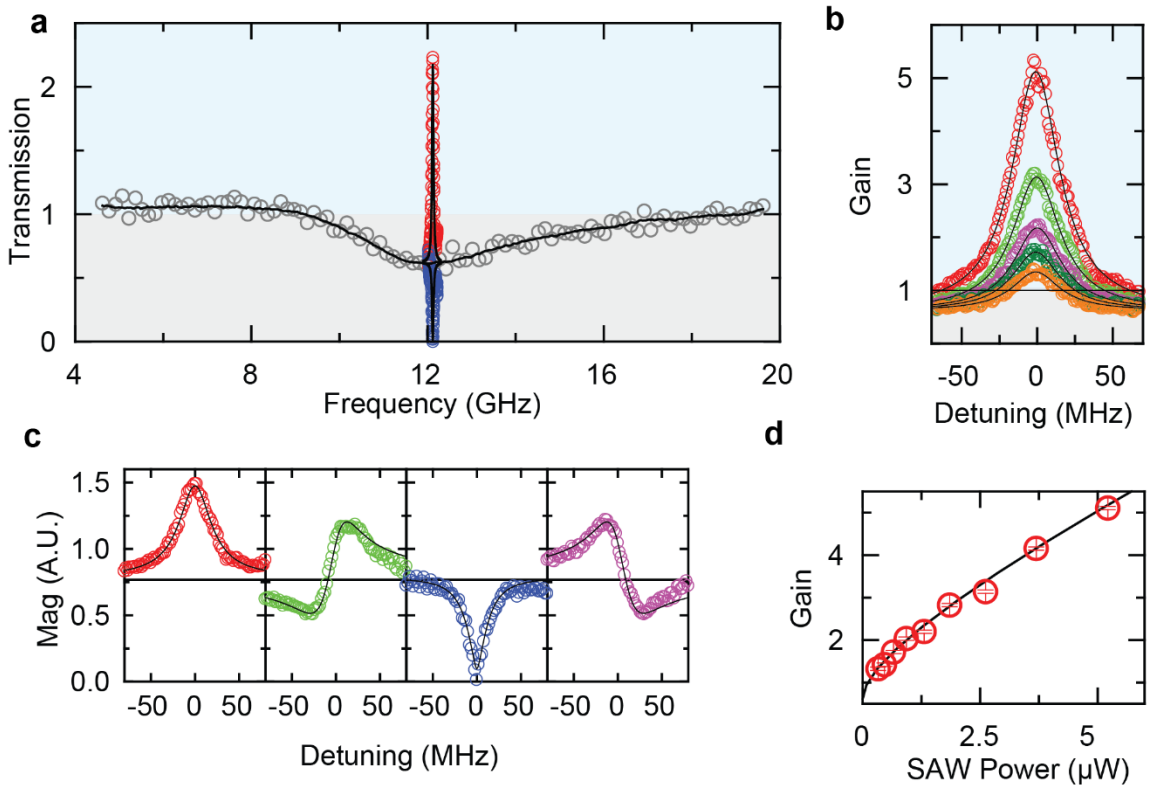

Figure 4.5 Optomechanically induced transparency and absorption.

a. Transmission spectrum of the probe light when the SAW is off (grey symbols) and on (red, blue symbols). Cavity absorption is shown as the dip in the grey region. When the SAW wave induced anti-Stokes light is in-phase with the probe, constructive interference leads to transparency and gain as shown by the peak above unity transmission (the blue region). When the anti-Stokes light is π out-of-phase with the probe, destructive interference enhances cavity absorption (the grey region), leading to high extinction of the probe. **b.** Gain of the system in the transparency region when the SAW power is increasing (orange: 0.33 μW, olive: 0.66 μW, purple: 1.3 μW, green: 2.6 μW, red: 5.2 μW). **c.** Transmitted probe light when the phase shift ϕ is set at 0 (red), π/2(green), π(blue), 3π/2 (purple). When the phase is at π/2 and 3π/2, the lineshapes imitate that of Fano resonances. **d.** The dependence of the system gain on the SAW power. The red symbols are experimental data while the black curve is the theoretical fitting.

When the interference is constructive (destructive), a transparency (absorption) window is observed within the cavity resonance, seen as the red peak (blue dip) in Figure

4.5a. Because in this homodyne measurement scheme the mechanical frequency and the probe detuning are synchronized, the transparency (absorption) window width agrees with the SAW IDT bandwidth (Figure 4.2d). Fixing the control light power, the SAW wave can be excited to a high amplitude to compensate the cavity loss and even amplify the probe light with a considerable gain, as shown in Figure 4.5b. When the gain is high so the cavity absorption is negligible, it is proportional to the SAW power (or number of propagating phonons), as shown in Figure 4.5d. In addition to transparency or absorption, the three-wave mixing process is controlled by the phase of the SAW wave relative to the probe. Columns in Figure 4.5c show the situations when the phase shift ϕ is set to 0, $\pi/2$, π and $3\pi/2$, respectively, so that the interference is tuned from constructive to destructive and displays Fano-resonance-like lineshape in between. We note that in our system SAW electro-optomechanically induces transparency and absorption [100], [101], which is different from OMIT where mechanical motion is stimulated optically [18], [19].

4.5. Coherent SAW Interaction with Multiple Photonic cavities

Besides the phenomena observable in sideband resolved cavity optomechanics, an important feature of our new platform is that the propagating mechanical wave can interact with multiple cavities in a coherent fashion. This scalability will be important, for example, to wavelength multiplexed coupling and conversion between microwave and optical photons. We demonstrate scalability by placing three nanocavities in the path of the SAW wave as shown in Figure 4.6a.

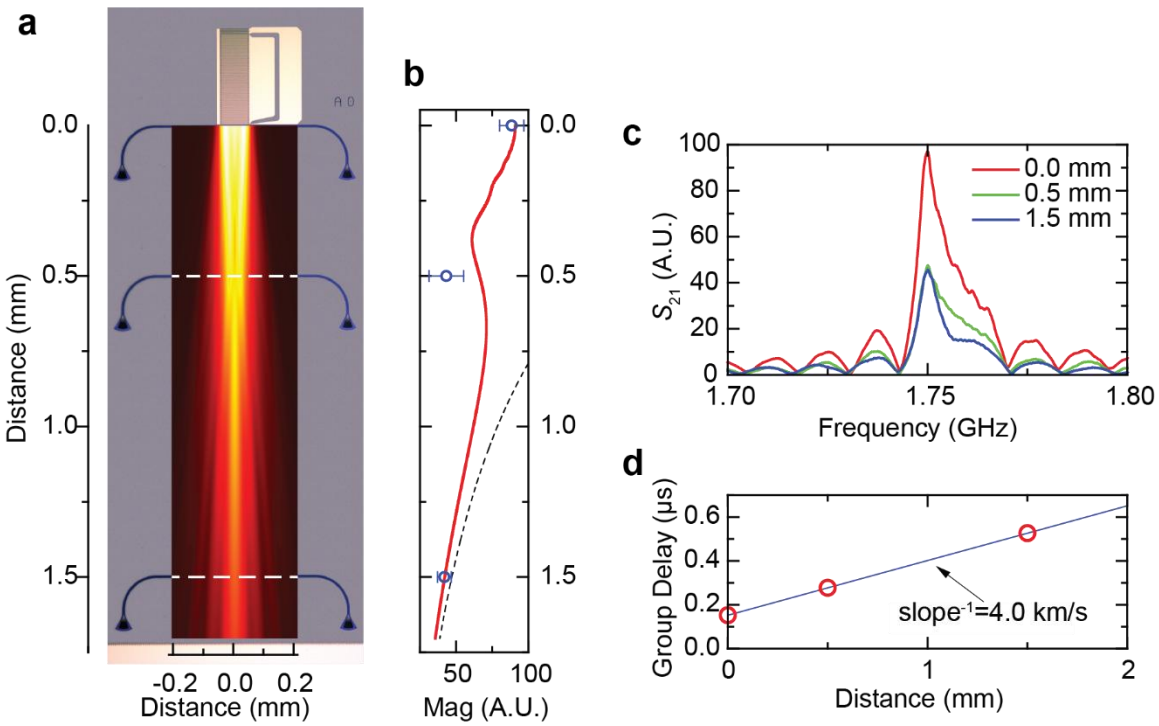

Figure 4.6 SAW wave coupling with multiple cavities and its diffraction.

a. Optical image of a device with three nanocavities in the path of SAW wave propagation. The photonic cavities are end-coupled with the waveguides and the SAW operates at a lower frequency of 1.75 GHz. Overlaid on the image is the calculated amplitude distribution of the diffraction pattern of the SAW wave. **b.** The calculated displacement amplitude along the center line of the SAW beam, showing non-monotonic variation along the propagation direction. Symbols are S_{21} magnitude measured from the three nanocavities. Dashed line is $e^{-\alpha r}/r^{1/2}$ asymptote of far-field amplitude of the wave for comparison, where α is the material loss assumed to be $(1.5\text{mm})^{-1}$. **c.** S_{21} spectra measured from the three nanocavities at a distance of 0, 0.5 and 1.5 mm to the IDT. **d.** Group delay of the three cavities' responses to the SAW wave as a function of their distance to the IDT. The inverse of the slope gives group velocity of 4.0 km/s.

These cavities are end-coupled with the waveguides and SAW transducers operate at a lower frequency of 1.75 GHz. As the beam of SAW wave propagates, it also undergoes diffraction that can be described by integrating Lamb's point source solution

along all the IDT finger pairs [105], each of which is treated as an effective line source. Overlaid in Figure 4.6a is the calculated displacement field amplitude of the propagating SAW wave, showing its diffraction pattern. Counter-intuitively, as shown in Fig. 4b, the displacement amplitude of the SAW wave changes non-monotonically along the central line of the IDT where the nanocavities lie. This is confirmed in the optical S_{21} spectra measured from the three cavities, as shown in Figure 4.6c, in which the farthest cavity (1.5 mm from the IDT) shows almost equally strong modulation as the second cavity (0.5 mm from the IDT). On the other hand, the phases of the optomechanical modulation of the three cavities are coherent with incremental time delays due to the propagating of the SAW wave. The phase delay and the distance of the three cavities to the IDT transducers are plotted in Figure 4.6d. The slope in the plot indicates the group velocity of the SAW wave to be 4.0 km/s. The demonstrated coupling between multiple cavities and SAW wave with well understood diffraction can be utilized to implement multiplexed microwave signal processing in the optical domain.

4.6. SAW Interaction with a Photonic Cavity in an Acoustic Echo Chamber

Finally, propagating phonons can be guided and confined in a fashion much like photons, with phononic structures such as one or two dimensional phononic crystals. Here we use acoustic Bragg reflectors (grating lines) to build a planar phononic cavity, or acoustic echo chamber, inside which a photonic nanocavity is inserted to investigate photon-phonon interaction. An optical image of the device is displayed in Figure 4.7a.

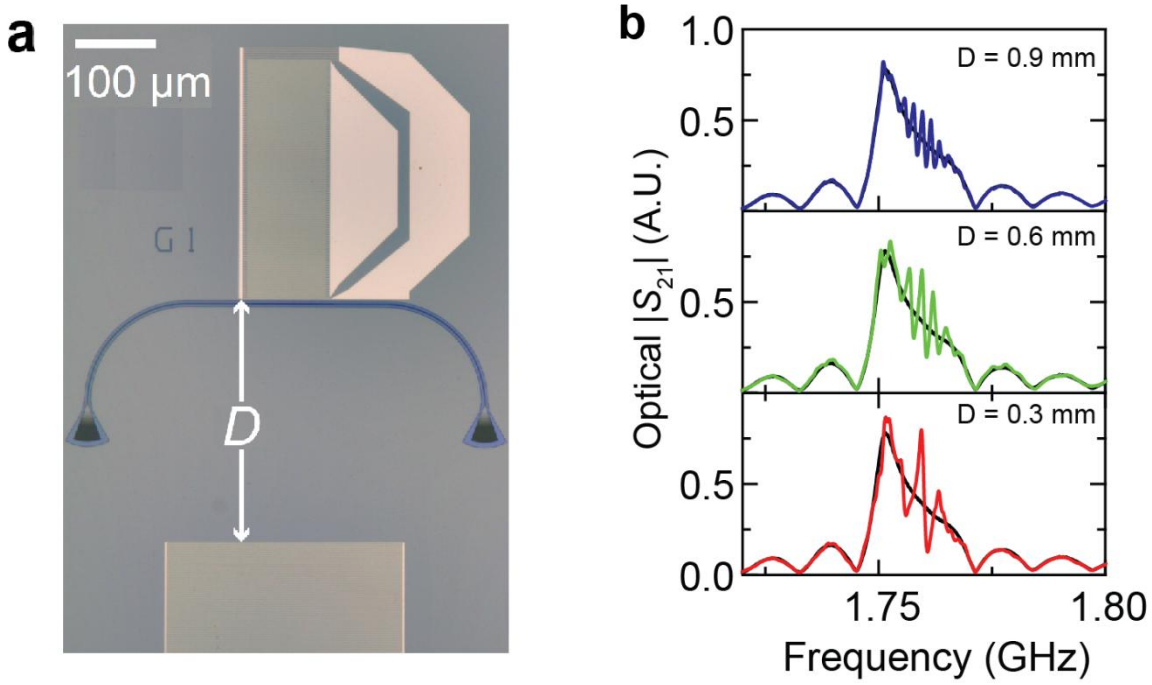

Figure 4.7 Photonic cavity inside a phononic cavity or acoustic echo chamber.

a. Optical image of the device. The distance between the IDT and the Bragg reflector is D. **b.** S_{21} spectra of devices with varying length D of the phononic cavities (red, green blue lines), compared with a device without the Bragg reflector (black line). The spectra show peaks corresponding to the resonances of the phononic cavity with decreasing peak spacing (or free spectral range) when the cavity length is increased.

Figure 4.6b shows the optical S_{21} spectra measured with the nanocavity inside phononic cavities of different lengths D=0.3, 0.6 and 0.9 mm. Similar to an optical Fabry-Perot cavity, the spacing between the peaks, or the free-spectral range, $\Delta\Omega$, decreases with increasing cavity length as given by $\Delta\Omega=2\pi/T=\pi c/(D+d)$, where T is the round-trip time, c is the group velocity of the SAW wave and d is the effective extra cavity length due to the Bragg reflectors. The nanocavity provides highly sensitive and broadband detection of acoustic wave travelling inside the chamber.

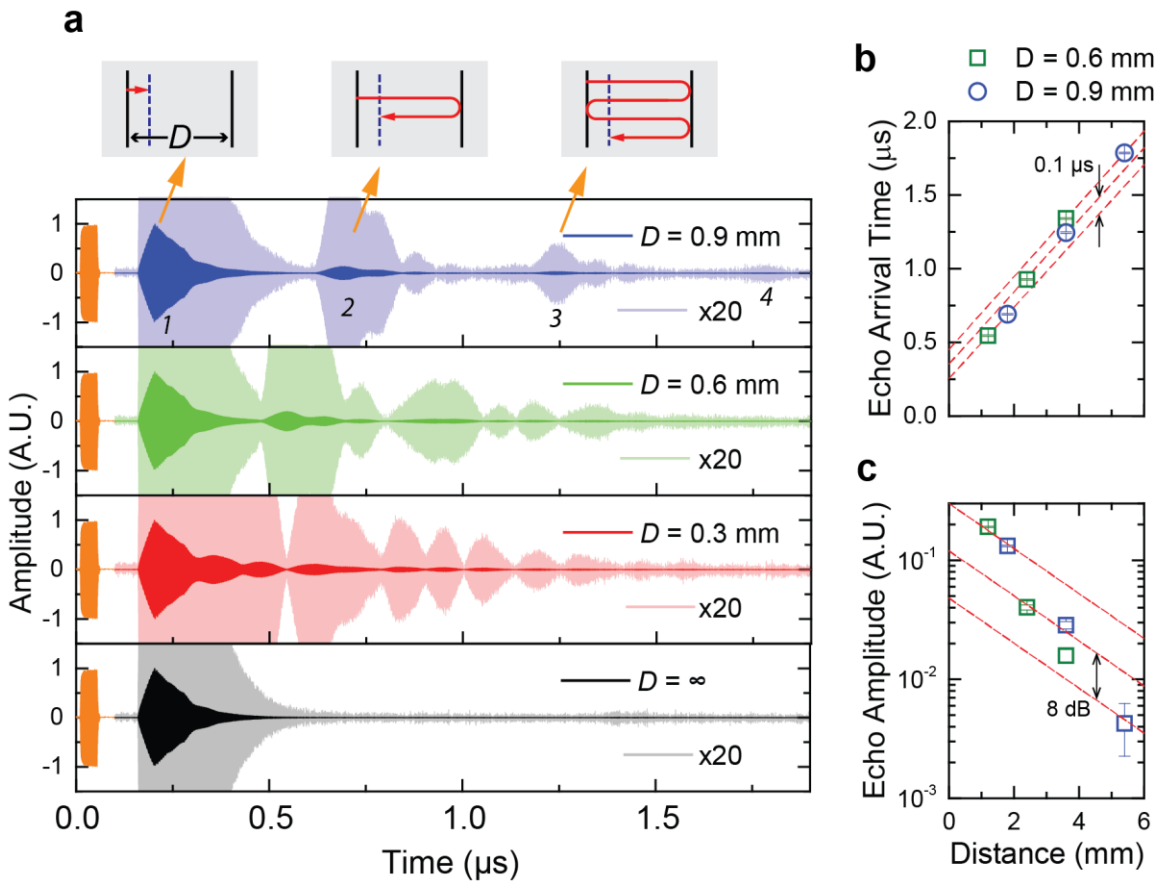

Figure 4.8 Time domain characterization of nano cavity-phonon pulse interaction.

a. Time-domain echo measurement of an acoustic pulse travelling inside phononic cavities of varying length D. Light colored traces are 20 times magnification of the dark colored traces. The acoustic pulse is excited by a 40 ns long burst of microwave at 1.75 GHz (orange). Up to four echoes of the pulse can be detected by the nanocavity. **b.** and **c.** The arrival time (b) and amplitude (c) of the detected echoes as a function of the apparent travel distance of the acoustic pulse. Red dashed lines are guides to eye assuming constant group velocity of 4.0 km/s (b) and exponential loss (c). The data deviate from the linear propagation due to extra delay (~0.1 μs) and loss (~8 dB) at the Bragg reflector of finite length.

By performing time domain measurement, we show that the nanocavity can "hear" multiple echoes of an acoustic pulse bouncing inside the chamber, as displayed in

Figure 4.8a. The acoustic pulse is first excited by a 40 ns microwave burst sent to the IDT (orange). Due to the electrical and optical delay, after ~160ns, the pulse was detected by the nanocavity for the first time. The pulse then propagates back and forth between the reflector and the IDT. It passes and is detected by the nanocavity for four times, is most obvious in the top panel, before its amplitude decays below the noise floor. From the arrival time and signal amplitude of multiple echoes, shown in Figure 4.8b and c, we observe that, other than linear propagation delay and loss, an extra delay of 100 ns (corresponding to d=200 μm) and loss of 8 dB occur during each round trip. Those are attributed to the Bragg reflector of finite length and can be optimized with more advanced design of low-loss phononic reflectors.

4.7. Summary

In conclusion, we have demonstrated a planar cavity optomechanical platform on which propagating acoustic waves can be generated, confined, and guided to interact with photonic cavities integrated in the same layer of AlN. By using high-resolution electron-beam lithography, IDTs can be patterned to excite acoustic waves at frequencies into the microwave Ku band. We expect it to be straightforward to further increase the frequency by using more advanced nanofabrication techniques such as nanoimprint lithography. In addition to high frequency, an important feature of a propagating mechanical wave is its scalability—multiple photonic cavities can be coupled. In contrast to other cavity optomechanical systems that include a mechanical resonator, the SAW in our current system is freely propagating and is not confined in a high-Qcavity. As a result, prominent optomechanical backaction effects such as optical spring, cooling, and amplification

cannot be achieved with such an open SAW system. However, high-Q acoustic cavities can be obtained if the acoustic loss can be reduced by removing substrate leakage, reducing diffraction via acoustic waveguides [97], [106], and suppressing intrinsic material loss at cryogenic temperatures [107]. More recently, a SAW cavity with a quality factor of up to 10^5 has been demonstrated at a cryogenic temperature [98]. Therefore, it is promising to achieve photon–phonon interaction in the regime of strong coupling on a SAW-based platform as a scalable modality of quantum optomechanics.

4.8. Methods

4.8.1. Device Fabrication

The devices were fabricated from a c-axis oriented, 330 nm thick piezoelectric aluminum nitride thin film sputtered (OEM Group, AZ) on a silicon wafer with a 3 μm buried silicon dioxide layer. The photonics layer was first patterned by electron beam lithography (Vistec EBPG-5000+) using ZEP-520A resist followed by chlorine based reactive ion etching. The AlN layer was etched down by 200 nm, leaving 130 nm thick AlN slab for the SAW wave to propagate without significant reflection and loss. The SAW IDT electrodes and contact pads were fabricated by electron beam lithography, followed by a 35 nm Ti/Au deposition and a liftoff process.

4.8.2. Measurement Setup

An external cavity tunable semiconductor laser was used as the laser source with its output power stabilized using a feedback loop. A 20 GHz electro-optic power modulator (EOM) was used to generate the probe sidebands for the observation of

optomechanically induced transparency and absorption. The laser (and the probe sidebands, if present) was further conditioned with a fiber polarization controller (FPC) and a variable optical attenuator (VOA) before being coupled into and out of the photonic crystal nanocavity via the on-chip grating couplers and waveguides. The output laser from the nanocavity was amplified with an erbium doped fiber amplifier (EDFA), filtered with an optical tunable band-pass filter (OTF) and measured with a high-speed photodetector (PD, New Focus 1474-A).

In frequency domain measurement, a vector network analyzer (VNA) (Agilent E8362B) was used to measure frequency response of the system. For S_{11} measurement, the VNA Port 1 was directly connected to the on-chip IDT through a microwave probe. For S_{21} measurements, the RF power output from VNA Port 1 was split into two paths with an RF power splitter. One path was connected to the on-chip IDT through the RF probe. The other path was connected to the EOM to generate the optical probe sidebands. Both paths were properly conditioned with RF amplifiers, tunable attenuators and/or tunable delay lines as phase shifters. The output from the PD was amplified before being sent into the VNA Port 2. In time domain measurements, RF bursts were generated by gating a continuous wave (CW) RF source with a pulse generator and a high-speed RF switch. The RF source and the pulse generator were properly synchronized to minimize phase jitter, which was crucial to ensure excellent identicalness of all the RF bursts. The generated RF bursts were sent to the on-chip IDT through the RF probe. The output of the PD was amplified and measured with an oscilloscope which was synchronously

triggered by the pulse generator. To achieve high signal to noise ratio, the device responses shown in Figure 4.8 were averaged for 2 seconds.

4.8.3. Photonic Crystal Nanocavity Design

In order to reduce loss of the propagating acoustic wave, the photonic crystal nanocavity is shallow etched, leaving an AlN slab. Therefore, the radiative loss channels for the shallow-etched photonic crystal nanocavity include radiation into the air, the substrate and the slab mode supported by the surrounding remaining AlN film. To achieve a high optical quality factor, the radiative loss should be minimized by maximizing the effective index contrast between the fundamental nanocavity mode (n_{c0}) and the AlN slab mode (n_{slab}), because n_{slab} is higher than the refractive indices of the substrate (n_{sub}) and the air.

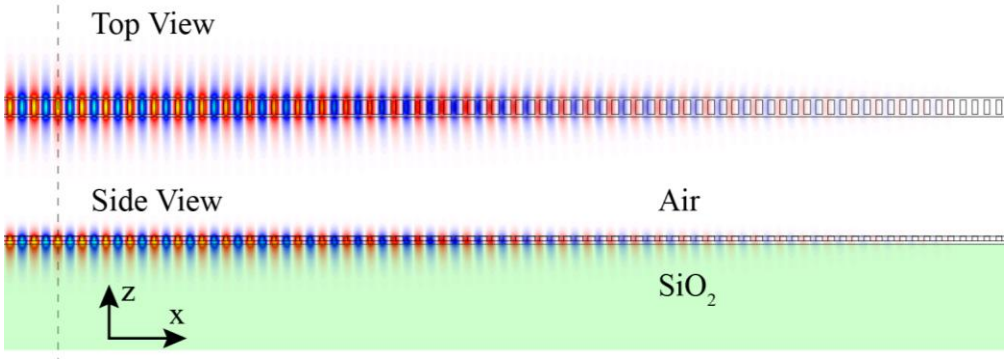

Figure 4.9 Photonic crystal nanocavity fundamental dielectric mode Ey profile.

The vertical dashed line is the center of the nanocavity. The E_y profile is symmetric with respect to the center.

To achieve strong optomechanical interaction, the overlap between the electric field distribution of the fundamental nanocavity mode and the mechanical strain field of the propagating SAW modes should be maximized. This indicates that the nanocavity should support dielectric modes [108] and n_{c0} should be maximized so that electric field is well confined inside the AlN structures.

The optimized nanocavity designs (subject to fabrication considerations) and coupling schemes are summarized as the follows. The cavity and the coupling waveguide are etched 200 nm deep into a 330 nm thick AlN film on top of a 3 μm thick silicon dioxide layer. The etched AlN sidewall is tilted by 15°, so all the dimensions here on refer to those at half the etching depth. The cavity lattice constant and width are 500 nm (corresponding to $n_{c0} \approx 1.54$) and 800 nm, respectively. The rectangular hole in each unit cell is 600 nm long (in the transverse direction of the cavity), while the hole width varies gradually from 242 nm at the cavity center to 108 nm across 90 unit cells away from the cavity center, and then remains 108 nm from there to the two ends of the cavity [108]. The coupling waveguide is 800 nm wide. For the cavity side-coupled to the waveguide, the total cavity length is 120 μm (240 unit cells) and the minimum coupling gap is 1.6 μm, resulting in high loaded and intrinsic quality factors suitable for sideband resolved optomechanical experiments. For the cavity embedded inside the waveguide (i.e. end coupled), the total cavity length is reduced to 100 μm (200 unit cells) to facilitate the coupling to the waveguide, resulting in enhanced on-resonance transmission and moderate loaded quality factor suitable for sideband unresolved optomechanical transduction. The simulated mode profiles are shown in Figure 4.9.

4.8.4. SAW IDT Eigen Mode Calculation

We employed a finite element method simulation to calculate the eigenmodes of the SAW IDT. The calculation was done using the piezo-plane strain model of the commercial FEM software, COMSOL Multiphysics. Due to the periodicity of the IDTs, only a unit cell, containing a pair of fingers, was simulated. A periodic boundary condition was imposed on the ends of the unit cell. The bottom boundary was set fixed, while the top boundary was allowed to displace freely. The calculation used experimentally reported material parameters [109]. The structure was meshed using appropriate parameters to increase the accuracy of the simulation.

Table 4-1 Summary of the SAW IDT eigen modes.

	IDT Period = 3 µm			**IDT Period = 0.45 µm**			
Rayleigh Mode Number	R1	R2	R3	R1	R6	R9	R14
Eigen Frequency (GHz)	1.22	1.48	1.74	8.39	9.20	10.11	11.76
Out of Plane Displacement Field Profile **Top Layer: AlN (330 nm)** **Middle Layer: SiO_2 (3 µm)** **Bottom Layer: Si**	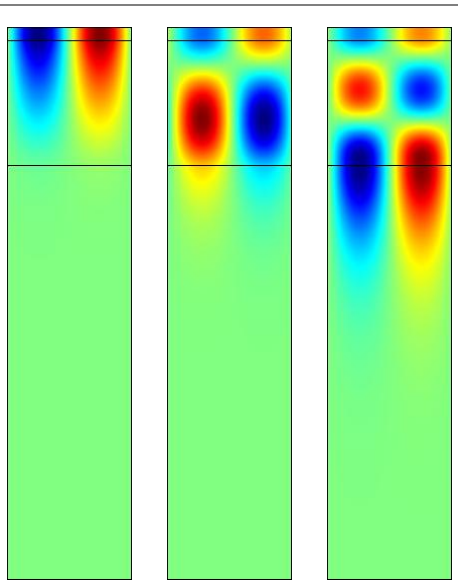			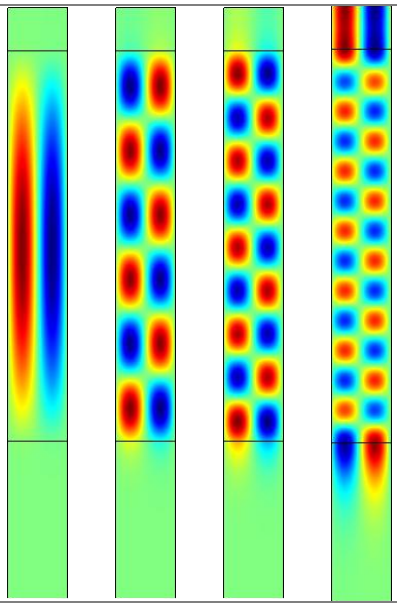			

This calculation was done for the 3 μm and 0.45 μm IDTs that were implemented in the experiment. The calculation showed that in the AlN/SiO2/Si multilayers, the 3 μm IDT can excite three Rayleigh modes, whereas the 0.45 μm IDT can excite as many as sixteen Rayleigh modes. The eigenfrequencies of these modes agree well with the measured S_{11} spectra of the IDTs (Figure 4.2c). The simulation results are summarized in Table 4-1.

4.8.5. Calculation of the SAW Power

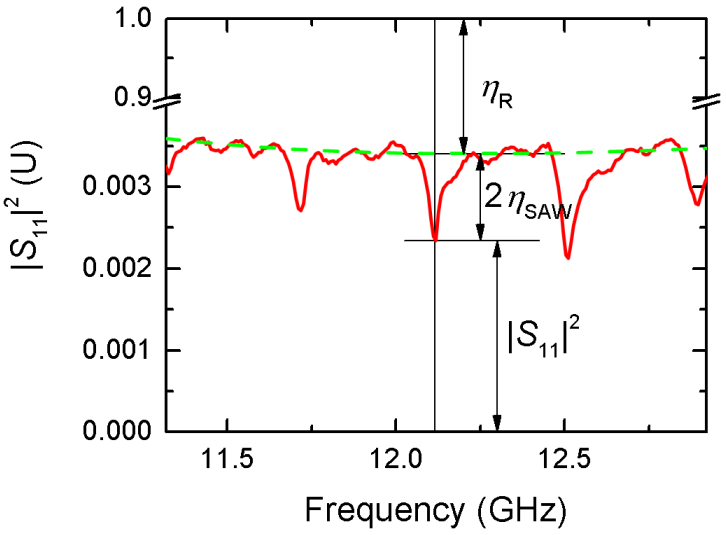

Figure 4.10 Estimation of the SAW power from S11 spectrum.

The resonance dip at 12.1 GHz is the R14 mode of the 0.45 μm period IDT.

The power of SAW wave that is electromechanically excited can be calculated from the S_{11} measurement of the IDT and the input RF power. Figure 4.10 shows the measured spectrum of $|S_{11}|^2$ centered at the frequency of the R14 mode of the 0.45 μm period IDT. At any frequency Ω, the total power dissipated at the IDT is

$$P_{\text{dis}} = P_{\text{in}}\left(1-\left|S_{11}(\Omega)\right|^2\right) = 2P_{\text{SAW}}(\Omega) + P_{\text{R}}(\Omega) = P_{\text{in}}\left[2\eta_{\text{SAW}}(\Omega) + \eta_{\text{R}}(\Omega)\right] \quad \textbf{4.1}$$

so,

$$1-\left|S_{11}(\Omega)\right|^2 = 2\eta_{\text{SAW}}(\Omega) + \eta_{\text{R}}(\Omega) \quad \textbf{4.2}$$

where P_{in} is the total input RF power, P_{SAW} (η_{SAW}) is the power (electromechanical coupling efficiency) of the SAW traveling through the photonic crystal nanocavity. The factor of 2 accounts for the fact that the IDTs launch SAW in both directions. P_{R} (η_{R}) is the power loss (power loss ratio) at the IDT due to various mechanisms (e.g. Joule heating and electromagnetic radiation loss) other than conversion to SAW. Generally, η_{R} is slowly varying with respect to frequency, while η_{SAW} is negligibly small outside the narrow resonance dips. Therefore, on the resonance frequency (Ω_{14}) of the R14 mode, $\eta_{\text{R}}(\Omega_{14})$ can be estimated from the interpolation of the adjacent $|S_{11}|^2$ data points outside the resonance dip as shown in Figure 4.10. In this case, $|S_{11}(\Omega_{14})|^2 = 2.34\times10^{-3}$, $\eta_{\text{SAW}}(\Omega_{14}) = 5.3\times10^{-4}$ and $\eta_{\text{R}}(\Omega_{14}) = 0.9965$.

The excitation of SAW is generally determined by the overlap integral between the stress field of the SAW mode and the stress field induced by the voltage actually present on the specific IDT design [23]. The propagation loss of the SAW and the efficiency of the RF power delivery from the RF source to the IDT also play important roles in determining the actual excitation of the SAW. Therefore, in our system where piezoelectric material (AlN) is only a thin layer on top of other non-piezoelectric materials (SiO2 and Si), the SAW modes whose stress field (or almost equivalently, the

mechanical energy) distribution is more confined in the AlN layer generally can be more strongly excited.

It is worth noting that, although R15 seems to be the most strongly excited SAW mode, as shown in Figure 4.10, we used R14 for the experiments because R14 provides the overall strongest modulation of the photonic cavity among all the SAW modes near 12 GHz, as shown in Figure 4.3a.

4.8.6. Optomechanical Coupling Coefficient Definition

The strength of optomechanical interactions in the optical cavity can be quantified using an optomechanical coupling coefficient, *G*, which is conventionally defined as the shift of the angular resonance frequency per unit displacement. This definition, however, requires that an effective SAW mode amplitude be defined, such that

$$\Delta\omega(t) = \delta\omega\cos(\Omega t) = GA_{\text{eff}}\cos(\Omega t) \qquad \textbf{4.3}$$

where $\Delta\omega(t)$ is the SAW induced sinusoidally time-varying shift of the optical cavity angular resonance frequency, $\delta\omega$ is the amplitude of $\Delta\omega(t)$, Ω is the SAW mode angular frequency and A_{eff} is the effective SAW mode displacement amplitude. Generally, A_{eff} can be arbitrarily defined as long as for any given SAW mode,

$$A_{\text{eff}} \propto \sqrt{P_{\text{SAW}}} \qquad \textbf{4.4}$$

where P_{SAW} is the traveling power of the SAW mode. In this work we define A_{eff} as

$$A_{\text{eff}} \equiv \sqrt{|A_x|^2 + |A_z|^2}\Big|_{\text{Max in AlN}} \qquad \textbf{4.5}$$

where A_x (A_z) is the displacement amplitude along the longitudinal (transverse, surface normal) direction of SAW wave. We note in Rayleigh modes, the particle motion in the substrate is in an elliptical trajectory. The right hand side of Eq. 4.5. is evaluated in the AlN layer at the depth where it reaches its maximum.

The power of the SAW mode is related to the SAW mechanical energy E by

$$P_{\mathrm{SAW}} = \frac{\Omega}{2\pi} E = \frac{\Omega}{2\pi} \gamma W A_{\mathrm{eff}}^2 , \qquad \textbf{4.6}$$

where E is the total mechanical (including potential and kinetic) energy contained in one period Λ of the SAW wave and it is proportional to the IDT aperture W. γ is a proportional factor relating A^2_{eff} to the total energy of SAW and defined as

$$\gamma \equiv \frac{E}{W A_{\mathrm{eff}}^2} = \frac{1}{W A_{\mathrm{eff}}^2} \int_{x,y,z=0}^{x,y,z=\Lambda,W,\infty} U(x, y, z, A_{\mathrm{eff}}) dxdydz. \qquad \textbf{4.7}$$

where U is the total mechanical (including potential and kinetic) energy density distribution of a particular mode excited to amplitude A_{eff}. The value of γ for a given SAW mode is calculated from FEM simulation results and the aperture size used in the experiments.

Therefore, the expression of A_{eff} for a given SAW power is

$$A_{\mathrm{eff}} = \sqrt{\frac{2\pi P_{\mathrm{SAW}}}{\gamma W \Omega}}. \qquad \textbf{4.8}$$

Consequently,

$$G = \delta\omega \sqrt{\frac{\gamma W \Omega}{2\pi P_{\mathrm{SAW}}}}. \qquad \textbf{4.9}$$

Alternatively, a more general and convenient way to quantify the interaction between an optical cavity and a traveling SAW mode is

$$\delta\omega = G'\sqrt{P_{\mathrm{SAW}}} = G'A'_{\mathrm{eff}}, \qquad \textbf{4.10}$$

where

$$A'_{\mathrm{eff}} = \sqrt{P_{\mathrm{SAW}}}. \qquad \textbf{4.11}$$

The coefficient *G*' defined in Eq. 4.10 can be determined and used experimentally without the need to solve the SAW mode profile and the ambiguous definition of SAW amplitude. The optomechanical coupling coefficients *G* and *G*' are related by

$$G = G'\sqrt{\gamma W \frac{\Omega}{2\pi}}. \qquad \textbf{4.12}$$

4.8.7. Theoretical Analysis of the Optomechanical Modulation in the Sideband Resolved Regime

Similar to conventional optomechanical systems [82], the SAW modulated photonic crystal nanocavity transmission spectrum can be derived using temporal coupled mode theory analysis [110]–[112].

The system can be modeled as a single mode cavity side-coupled to a continuous waveguide. There are three ports in the system: the input and output waveguides, and the cavity loss channel. Under the modulation of the SAW wave, the intra-cavity field amplitude, *a*, evolves with time as

$$\frac{da}{dt} = \left\{ j\left[\omega_0 + \delta\omega\cos(\Omega t)\right] - \frac{1}{\tau} \right\} a + \sqrt{\frac{1}{\tau_e}} s_{in} e^{j\omega t}, \qquad \textbf{4.13}$$

where ω_0 and τ are the center frequency and the lifetime of the resonance mode, respectively, $1/\tau_e$ is the total decay rate due to the coupling to both the input and output waveguides. The amplitude a is normalized such that $|a|^2$ corresponds to the energy inside the resonator. The resonance mode is excited (detected) by the incoming (outgoing) wave s_{in} (s_{out}) from the input (output) waveguide, which is normalized in such a way that $|s_{in}|^2$ ($|s_{out}|^2$) corresponds to the input (output) power. The quantities in the expression $\delta\omega\cos(\Omega t)$ has been defined in Eq. 4.3. Without any loss of generality, we assume that s_{in} is the phase reference, namely, s_{in} is real and positive,

$$s_{in} = |s_{in}|. \qquad \textbf{4.14}$$

The SAW modulation induces sidebands. One can write the intra-cavity field amplitude as a Fourier superposition of these sidebands as

$$a = \sum_m a_m e^{j(\omega + m\Omega)t}. \qquad \textbf{4.15}$$

Substituting Eq. 4.15 into Eq. 4.13 and rearranging, we get

$$\begin{aligned} \sum_m j(\omega + m\Omega) a_m e^{j(\omega+m\Omega)t} = &\left(j\omega_0 - \frac{1}{\tau} \right) \sum_m a_m e^{j(\omega+m\Omega)t} \\ &+ \frac{1}{2} j\delta\omega \left(e^{j\Omega t} + e^{-j\Omega t} \right) \sum_m a_m e^{j(\omega+m\Omega)t} \\ &+ \sqrt{\frac{1}{\tau_e}} s_{in} e^{j\omega t} \end{aligned} \qquad \textbf{4.16}$$

In the sideband resolved limit, only the first order sidebands will have significant amplitude in addition to the carrier amplitude. Comparing terms proportional to $e^{j\omega t}$, and taking into account the fact that $|a_0|^2 >> |a_{\pm 1}|^2$, we get

$$a_0 = \frac{\sqrt{1/\tau_e}}{j\Delta + 1/\tau} s_{in}, \qquad \textbf{4.17}$$

which is the carrier component of the intra-cavity field amplitude. $\Delta = \omega - \omega_0$ is the cavity detuning. Doing the same for terms proportional to $e^{j(\omega \pm \Omega)t}$, we get the sideband amplitudes as

$$a_{\pm 1} = \left(\frac{j\,\delta\omega/2}{j(\Delta \pm \Omega) + 1/\tau} \right) a_0 = \left(\frac{j\,\delta\omega/2}{j(\Delta \pm \Omega) + 1/\tau} \right) \left(\frac{\sqrt{1/\tau_e}}{j\Delta + 1/\tau} \right) s_{in} \equiv |a_{\pm 1}| e^{j\phi_{\pm 1}} \qquad \textbf{4.18}$$

which implies that (note that s_{in} is assumed to be real and positive)

$$|a_{\pm 1}| = \frac{\delta\omega/2}{\left((\Delta \pm \Omega)^2 + 1/\tau^2\right)^{1/2}} \frac{\sqrt{1/\tau_e}}{\left(\Delta^2 + 1/\tau^2\right)^{1/2}} |s_{in}|, \qquad \textbf{4.19}$$

$$\cos(\phi_{\pm 1}) = \frac{(2\Delta \pm \Omega)/\tau}{\left((\Delta \pm \Omega)^2 + 1/\tau^2\right)^{1/2} \left(\Delta^2 + 1/\tau^2\right)^{1/2}}, \text{ and} \qquad \textbf{4.20}$$

$$\sin(\phi_{\pm 1}) = \pm \frac{1/\tau^2 - \Delta(\Delta \pm \Omega)}{\left((\Delta \pm \Omega)^2 + 1/\tau^2\right)^{1/2} \left(\Delta^2 + 1/\tau^2\right)^{1/2}}. \qquad \textbf{4.21}$$

The amplitude and power of the outgoing wave in the output waveguide are, respectively,

$$s_{out} e^{j\omega t} = -s_{in} e^{j\omega t} + \sqrt{1/\tau_e}\, a \qquad \textbf{4.22}$$

$$|s_{out}|^2 = \left| T_0 + \sqrt{1/\tau_e} \left(a_{-1} e^{-j\Omega t} + a_{+1} e^{j\Omega t} \right) \right|^2, \qquad \textbf{4.23}$$

where

$$T_0 = -s_{\text{in}} + \sqrt{1/\tau_{\text{e}}}\, a_0 \equiv |T_0| e^{j\theta}, \tag{4.24}$$

$$\theta = \arctan\left(\frac{\Delta/\tau_{\text{e}}}{-\left(\Delta^2 + 1/(\tau\tau_{\text{i}})\right)} \right) + \pi. \tag{4.25}$$

Taking into account the fact that $|a_0|^2 >> |a_{\pm 1}|^2$ and retaining the dominant terms, $|s_{\text{out}}|^2$ reduces to

$$\begin{aligned} |s_{\text{out}}|^2 &\approx |T_0|^2 + 2\,\text{Re}\left[T_0 \sqrt{1/\tau_{\text{e}}} \left(a_{-1}^* e^{j\Omega t} + a_{+1}^* e^{-j\Omega t} \right) \right] \\ &= |T_0|^2 + 2|T_0| \sqrt{1/\tau_{\text{e}}} \left(|a_{-1}| \cos\left(-\phi_{-1} + \Omega t + \theta\right) + |a_{+1}| \cos\left(\phi_{+1} + \Omega t - \theta\right) \right) \end{aligned} \tag{4.26}$$

Lumping together the quadrature components, the total output power takes the expression

$$|s_{\text{out}}|^2 \approx |T_0|^2 + B\cos\left(\Omega t + \varphi\right), \tag{4.27}$$

where

$$B = 2|T_0| \sqrt{1/\tau_{\text{e}}}\, C, \text{ and} \tag{4.28}$$

$$C = \left\{ \left[|a_{-1}| \cos\left(-\phi_{-1} + \theta\right) + |a_{+1}| \cos\left(\phi_{+1} - \theta\right) \right]^2 + \left[\begin{matrix} |a_{-1}| \sin\left(-\phi_{-1} + \theta\right) + \\ |a_{+1}| \sin\left(\phi_{+1} - \theta\right) \end{matrix} \right]^2 \right\}^{1/2}. \tag{4.29}$$

where $1/\tau_{\text{i}}$ is the intrinsic decay rate of the cavity. In the under-coupled regime where $\tau_{\text{e}} << \tau \approx \tau_{\text{i}}$, $\theta \approx 0$, the above expressions for C and φ can be further simplified to

$$C = \left\{ \left[|a_{-1}| \cos\left(-\phi_{-1}\right) + |a_{+1}| \cos\left(\phi_{+1}\right) \right]^2 + \left[|a_{-1}| \sin\left(-\phi_{-1}\right) + |a_{+1}| \sin\left(\phi_{+1}\right) \right]^2 \right\}^{1/2}, \tag{4.30}$$

$$\varphi = \arctan\left[\frac{|a_{-1}|\sin(-\phi_{-1}) + |a_{+1}|\sin(\phi_{+1})}{|a_{-1}|\cos(-\phi_{-1}) + |a_{+1}|\cos(\phi_{+1})}\right] + \begin{cases} 0 & \text{if denominator} \geq 0 \\ \pi & \text{if denominator} < 0 \end{cases}. \quad \textbf{4.31}$$

The first term of the right hand side of Eq. 4.27 is the cavity transmission spectrum without SAW modulation, and the second term (the cosine term) is the oscillating power at the SAW frequency due to the beating between the carrier and the two sidebands. The coefficient *B* of the second term in Eq. 4.27 is used to fit the experimental data in Figure 4.3.

4.8.8. Determination of Optomechanical Coupling Coefficient in the Sideband Resolved Regime

In order to determine *G* and *G*' from the experimental data shown in Figure 4.3 in the main text, we first calculate the amplitude of the oscillating optical power (*B*) in the output waveguide of the device, using the calibrated lumped RF optical gain of our experimental setup. The lumped gain takes into account the gain and loss of all the experimental equipment from the output grating coupler of the device to the RF amplifiers between the photo detector and the network analyzer. Then the full expression for *B*, including Eq. 4.28 and Eq. 4.29 are used to fit the experimental data with $\delta\omega$ as the only free parameter. Meanwhile, the power and effective amplitude of the SAW used in the experiment is estimated using Eq. 4.1. Subsequently Eq. 4.3 and Eq. 4.10 are used to determine *G* and *G*'. The important device parameters used for data processing are summarized in Supplementary Table 4-2.

Table 4-2 Summary of the device parameters for sideband resolved optomechanical experiments.

Photonic Crystal Nanocavity	Resonance Wavelength	1529.7 nm
	Linewidth ($2/\tau$)	$(2\pi)\cdot 3.88$ GHz
	Extinction Ratio	1.64
	Loaded Q	5.1×10^4
	Intrinsic Q	6.5×10^4
	Total Lifetime τ	82 ps
	Intrinsic Lifetime τ_i	105 ps
	External Lifetime τ_e	375 ps
Optical Power	Input Waveguide (DC, On-Chip)	22 μW
	Output Waveguide (RF, On-Chip)	Data in Fig. 2c
SAW Excitation for R14 (IDT Period = 0.45 μm)	Conversion Efficiency η_{SAW}	5.3×10^{-4}
	Power P_{SAW}	0.88 μW
	Aperture W	100 μm
	Peak Frequency	12.12 GHz
	Coefficient γ**	5.7×10^{12} N/m^2
	Effective Displacement Amplitude	0.40 pm
Optomechanical Interaction	Amplitude of Optical Resonance Frequency Oscillation $\delta\omega$	$(2\pi)\cdot 21$ MHz
	Coupling Coefficient G	$(2\pi)\cdot 53$ GHz/nm
	Coupling Coefficient G'	$(2\pi)\cdot 23$ MHz$\cdot(\mu W)^{-1/2}$

** From FEM simulation.

Chapter 5. Acousto-optic Modulation of a Photonic Crystal Nanocavity with Lamb Waves in Microwave K Band [25]

Integrating nanoscale electromechanical transducers and nanophotonic devices potentially can enable acousto-optic devices to reach unprecedented high frequencies and modulation efficiency. Here, we demonstrate acousto-optic modulation of a photonic crystal nanocavity using Lamb waves with frequency up to 19 GHz, reaching the microwave K band. The devices are fabricated in suspended aluminum nitride membrane. Excitation of acoustic waves is achieved with interdigital transducers with period as small as 300 nm. Confining both acoustic wave and optical wave within the thickness of the membrane leads to improved acousto-optic modulation efficiency in these devices than that obtained in previous surface acoustic wave devices. Our system demonstrates a scalable optomechanical platform where strong acousto-optic coupling between cavity-confined photons and high frequency traveling phonons can be explored.

5.1. Introduction

Exploitating of light-sound interactions in various types of media has led to a plethora of important optical technologies ranging from acousto-optic devices for optical communication [35] to photo-acoustic imaging in biomedicine [113]. Particularly, in the widely used acousto-optic devices, electromechanically excited acoustic waves in crystals are used to deflect, modulate and frequency-shift light to achieve optical signal processing [114]. Despite affording unique optical functionalities, conventional acousto-optic devices built on bulk crystals provide operation bandwidth only in the sub-gigahertz

range, which is insufficient for the need of modern optical communication, and consequently has not been as widely employed as electro-optic devices [115]. With advances of integrated photonics and nanofabrication technology, it is now more feasible to miniaturize and integrate acousto-optic devices to augment their speed and performance so they can assume indispensable roles in integrated photonic systems for chip-scale optical communication [43]. Moreover, in addition to electromechanical excitation, acoustic waves or localized mechanical vibrations can also be optically stimulated through optomechanical forces including radiation pressure, gradient force and electrostriction. Such optomechanical effects recently have been extensively investigated in various optomechanical systems with dimensional scales ranging from meters to nanometers [1], [78]. Therefore, with these recent developments, acousto-optics is entering a new era with plenty of research opportunities [55], [23], [116], [117]. In the realm of nonlinear optics, stimulated Brillouin scattering (SBS) is also mediated by optomechanical and acousto-optic effects and recently has been demonstrated in various on-chip devices [69], [118], [119].

To enable strong and efficient acousto-optic interaction, one strategy is to simultaneously confine light and sound to optimize the spatial overlap of their modes. While three dimensional optical waveguides and cavities can be readily designed and fabricated, acoustic waves can be more conveniently excited electromechanically and confined in thin films which provide two dimensional confinement. In contrast to optically excitation, exciting acoustic waves electrically decouples the design of the photonic and phononic devices, giving more flexibility in device design and fabrication.

And importantly, it avoids the need of high power optical pump which would otherwise affect the photonic system by inducing unwanted nonlinearities. Types of acoustic waves that are commonly employed for radio-frequency and microwave signal processing applications include bulk acoustic waves (BAW), surface acoustic waves (SAW), and in free-standing thin plates, Lamb waves (LW) and flexural plate waves (FPW) [120]. Among these, SAW and Lamb waves can be excited with periodically arranged planar electrodes named inter-digital transducers (IDTs), and thus are more suitable for integration with planar photonic systems [31], [121]. The generated acoustic wave has a well-defined wavelength and frequency. The wavelength is determined by the IDT period (Λ), while the frequency depends on the wavelength and the sound velocity of the materials that constitute the structure in which acoustic wave propagates. Therefore, to achieve acoustic wave devices operating at ultrahigh frequency, the period of the IDT needs to be very small [52] and the materials with ultrahigh sound velocity, such as diamond[122], need to be used as the substrate.

To combine acoustic and photonic devices, the material platform needs to afford both piezoelectricity for excitation of acoustic waves and high refractive index contrast to enable optical confinement. Previously, we and other groups have used piezoelectric aluminum nitride (AlN) film deposited on silicon wafers with a layer of silicon dioxide (SiO_2) [57], [23]. Since AlN has a relatively high refractive index of about 2.1, photonic waveguides and cavities can be fabricated in AlN with the SiO_2 layer as the cladding. At the same time, acoustic waves can be exited in the AlN layer. On this platform, we have demonstrated SAW wave with frequency up to 12 GHz and its acousto-optic modulation

of optical ring resonators and photonic crystal nanocavities [23], [24]. However, an important drawback of above devices based on SAW is that the SiO_2 layer has a lower sound velocity than both the top AlN layer and the bottom silicon substrate. As a result, the excited acoustic waves in the AlN layer tend to leak into and be guided in the SiO_2 layer whereas the optical modes are highly confined in the top AlN layer because of its high refractive index. Consequently, the modal overlap between the optical and acoustic modes is low, leading to relatively weak acousto-optic coupling efficiency. To circumvent this problem, in this work, we implement integrated acousto-optic devices on a suspended AlN membrane. When the membrane thickness is less than or comparable to the acoustic wave, the generated acoustic wave will propagate as a Lamb wave mode with very high acoustic velocity. The removal of the substrate enforces the optical mode and the acoustic wave to maximally overlap within the thickness of the membrane. With this approach, we demonstrate acousto-optic modulation of a photonic crystal nanocavity at frequency up to 19 GHz with improved modulation efficiency.

5.2. Device Design and Fabrication

The device consists of a photonic crystal nanobeam cavity and an IDT as shown in Figure 5.1a. The nanocavity is designed to support the fundamental dielectric mode to enhance the acousto-optic interaction in AlN [108]. The nanobeam is 800 nm wide and 46.8 μm long, inscribed with a nanocavity formed by an array of 600 nm wide rectangular holes arranged with a lattice constant of 520 nm. The length of the holes is varied adiabatically from 221 nm in the cavity center to 127 nm at the start of the mirror section of the nanocavity. An 800 nm wide waveguide is placed 1.0 μm away from the

nanobeam to couple light into and out of the cavity. Input and output of light to/from the waveguide are through a pair of grating couplers. Two sets of IDTs with periods of 2.0 and 0.3 μm (corresponding to electrode linewidth of 500 nm and 75 nm), with 150 and 250 pairs of electrode fingers, respectively, are fabricated. The IDTs are placed to launch acoustic waves propagating in the direction transverse to the nanobeam and their apertures are designed to be the same as the nanocavity length of 46.8 μm to maximize acousto-optic overlap.

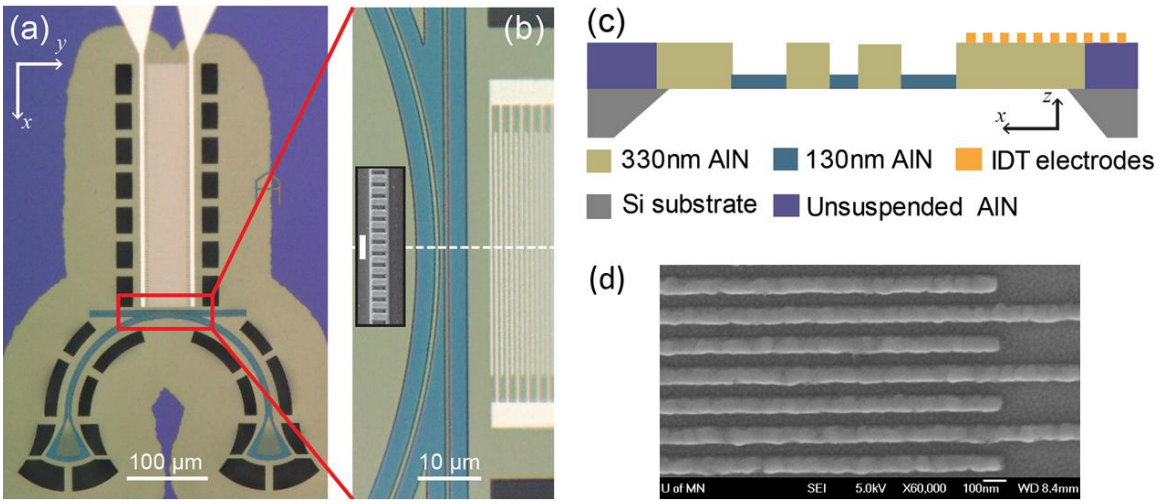

Figure 5.1 Photonic crystal nanocavity integrated width Lamb wave transducer on aluminum nitride membrane.

a. Optical microscope image of a fabricated device including IDT, photonic waveguide and nanocavity on a suspended AlN membrane (gray yellow regions). The unsuspended area of AlN is purple. **b.** Zoomed in optical image of the area around the photonic crystal nanobeam cavity and IDT electrodes. The dark green region is the 130 nm AlN slab. Inset: scanning electron microscope image of the photonic crystal cavity. Scale bar: 1 μm. **c.** Cross-sectional view of the device structure along the white dashed line in (b). (d) Close up SEM image of the 0.3 μm LW transducer electrodes.

The devices were fabricated on an AlN (330 nm)/Si substrate. Figure 5.1(a) and (b) show optical microscope images of a device with 2.0 μm period IDT. The photonic structure was first patterned in the AlN layer using electron beam lithography (EBL) and plasma etching processes. The 330 nm thick AlN layer was etched by 200 nm in depth, leaving a 130 nm slab to facilitate acoustic wave propagation and reduce acoustic reflection. Subsequently, the IDT electrodes were patterned using EBL and electron beam evaporation of 50 nm thick aluminum followed by a liftoff process. Another step of EBL and plasma etching was done to open windows (dark rectangular holes in Fig. 1(a)) for releasing the membrane. Finally, a XeF_2 dry etching process was used to release the membrane. A cross-sectional view illustrating the structure of the IDT, the waveguide and the nanocavity on the suspended membrane is shown in Figure 5.1c.

5.3. Device Characterization

The nanocavity side-coupled to the waveguide was characterized by measuring its transmission spectrum using a tunable laser. The result is shown in Figure 5.2, displaying several resonance modes of the nanocavity. We focus on the fundamental resonance mode (a symmetric mode) at 1543.94 nm with a loaded quality factor of 6.3×10^3 (corresponding to linewidth of 31 GHz) and an extinction ratio of over 25 dB (inset, Figure 5.2). The corresponding intrinsic quality factor is 1.1×10^5.

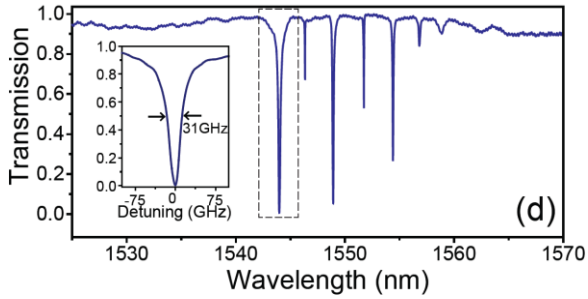

Figure 5.2 Transmission specrum of the photonic nanocavity.

The inset displays a zoom-in view of the fundamental resonance mode, showing a linewidth of 31 GHz.

5.3.1. Lamb Wave Transducer Characterization

The IDT transducers were characterized by measuring the spectrum of reflection coefficient S_{11} using a vector network analyzer (VNA, Agilent E8362B). The VNA Port 1 was directly connected to the IDT through a microwave probe. As shown in Figure 5.3a and b, for the device with 2.0 μm period IDT, four prominent acoustic modes with frequencies of 1.35 GHz, 5.40 GHz, 10.12 GHz, and 14.46 GHz, respectively, can be observed; for the device with 0.3 μm period IDT, two modes with frequencies of 16.37 GHz and 19.20 GHz, respectively, can be observed. The resonance frequencies agree well with the eigenfrequencies calculated for a 330 nm thick AlN membrane using finite element method (FEM) simulation package. The calculation yielded two fundamental Lamb wave modes (A0 and S0) and many higher order modes (A1, S1, A2, S2, etc.). The nomenclature of the modes is based on the symmetry of the displacement field profile and the number of nodes, with respect to a plane dissecting and in the plane of the

membrane. The simulated displacement profile and strain field distribution of each mode are shown in Figure 5.3c.

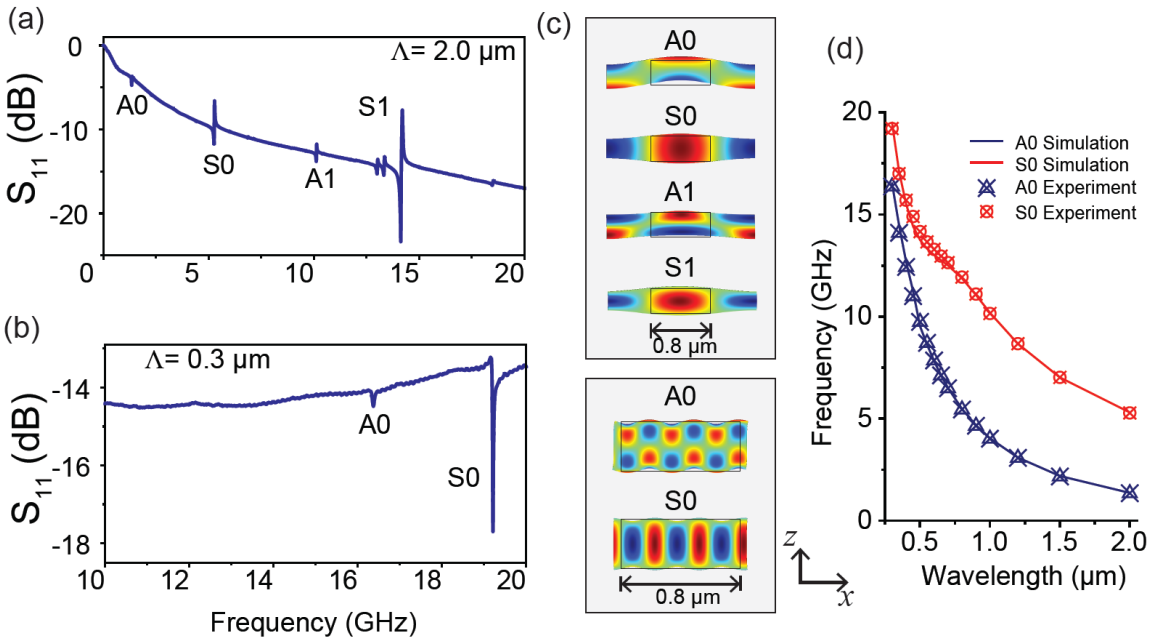

Figure 5.3 Lamb wave transducer characterization.

a. and **b.** Measured spectra of the reflection coefficient S_{11} of two devices with IDT periods of 2.0 μm and 0.3 μm, respectively. **c.** Simulated Lamb wave modes for both devices. The deformation of the shape indicate the displacement and the color map illustrate the strain field. Red (blue) color indicates positive (negative) strain. The black box illustrates the cross-section of the nanocavity (800 nm×330 nm). "A" and "S" stand for "antisymmetric" and "symmetric". The coordinate system is marked and consistent with that used in Fig. 1. **d.** The dispersion relation of Lamb wave in 330 nm thick AlN membrane. The solid lines are calculated results and the symbols depict experimentally measured values.

Within the measurable frequency range limited by the maximum frequency (20 GHz) of our VNA, the A0, S0, A1 and S1 modes can be observed in the device with 2.0 μm period IDT, whereas only the A0 and S0 modes can be observed in the device with

0.3 μm period IDT. Compared with the SAW wave generated with the same 2.0 μm period IDT but on unsuspended AlN layer on the SiO_2 (3 μm)/Si substrate, the frequency of Lamb wave on suspended membrane is almost an order of magnitude higher because the acoustic wave only propagates in AlN which has a high sound velocity. In addition, because the displacement and strain fields (hence the mechanical energy) of the Lamb wave are confined in the membrane that is completely decoupled from the substrate, the propagation loss is expected to be much less than SAW which has high loss to the substrate. Accurate measurement of propagation loss should be performed with acoustic delay line devices with various lengths but is out of the scope of this letter.

To study the frequency-wavelength dispersion relation of the Lamb wave in the AlN membrane, IDTs with a wide range of periods were fabricated, measured and simulated, as shown by the results in Figure 5.3d. Excellent agreement was obtained between experiment and theory. It can be observed that, for IDT periods much longer than the AlN film thickness (330 nm), the S0 mode has a much higher frequency (more than double) than that of the A0 mode. But as the IDT period deceases to a value comparable or less than the thickness of the membrane, the A0 and S0 mode frequencies both approach a value expected for a Rayleigh-type surface wave. Therefore, to support a Lamb wave of very high frequency, the membrane thickness can be further reduced and the S0 Lamb mode has the advantage of higher frequency than the A0 mode.

5.3.2. Lamb Wave Photonic Crystal Nanocavity Modulation

To characterize the acousto-optic interaction between the Lamb wave and the optical mode of the nanocavity, the probe laser was blue-detuned to the nanocavity's

fundamental resonance mode. The output optical signal was amplified with an erbium doped fiber amplifier (EDFA) and then filtered with a tunable optical filter to suppress amplified spontaneous emission noise introduced by the EDFA. The amplified and filtered optical signal was then sent to a high speed photoreceiver and the output electrical signal was returned to the VNA Port 2. The VNA Port 1 remained connected to the IDT. In this measurement configuration, the response of the nanocavity resonance to the acousto-optic modulation induced by the Lamb wave was characterized by measuring the spectrum of the system's transmission coefficient S_{21}, which was obtained by sweeping the frequency of the VNA output signal from Port 1 to the IDT. During the measurement, the VNA output power was fixed at 10 μW (-20 dBm) to minimize heating of the membrane, which can cause frequency shift of the nanocavity's resonance. The measured transmission spectra for the two devices are shown in Figure 5.4. The S_{11} spectra are also plotted for comparison. As can be seen from the plots, the acousto-optic response spectra show peaks at frequencies matching those of the Lamb wave modes measured in the S_{11} spectra. Comparing the amplitudes of the peaks reveals the different acousto-optic modulation strength of the various acoustic modes. Specifically, for the device with 2.0 μm period IDT, it can be observed that the higher order modes A1 and S1 induce much weaker (almost 30 times weaker) modulation than the fundamental modes A0 and S0. For the device with 0.3 μm period IDT, only the modulation of A0 and S0 modes was measured within the 20 GHz bandwidth of the VNA.

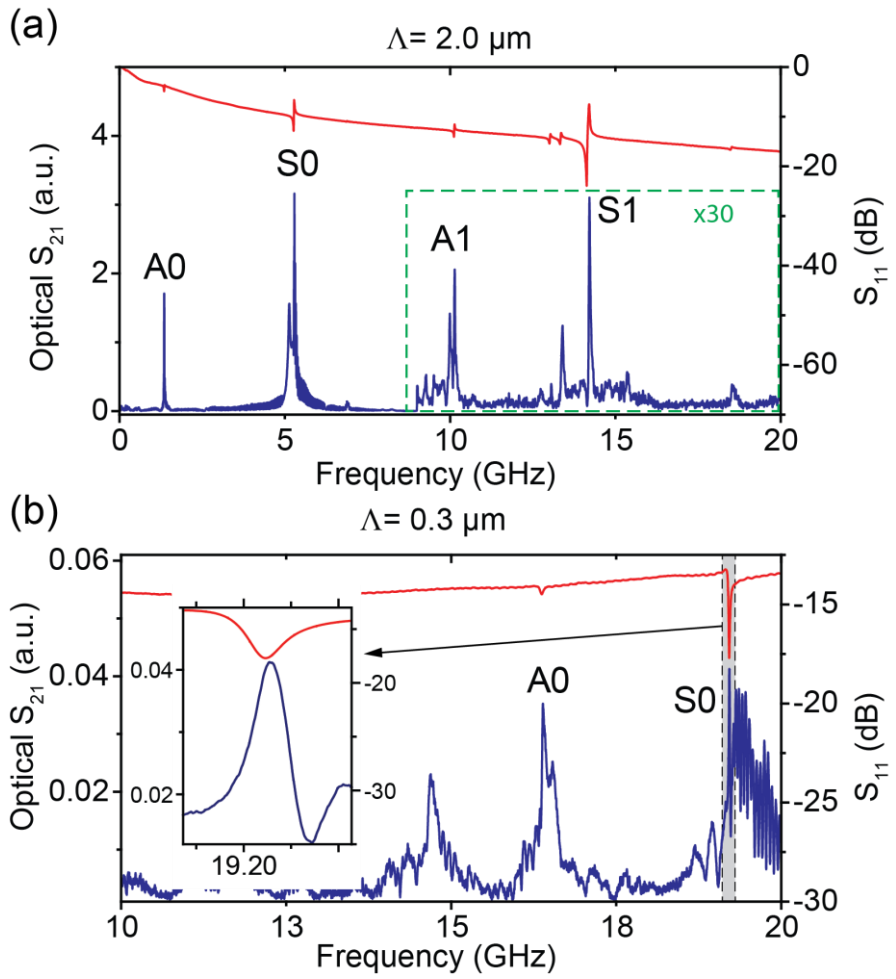

Figure 5.4 . Measured responses of the nanocavity to acousto-optic modulation induced by the Lamb wave.

The system's transmission coefficient S_{21} (blue traces, left axes), for the devices with IDT period of, **a.** 2.0 μm, and, **b.** 0.3 μm. In (a), the spectrum in the dashed box is scaled up by 30 times for clarity. The spectra of S_{11} (red traces, right axes) are also plotted for comparison. Inset of (b) is a zoom-in of the S0 mode at 19.20 GHz, of the device with 0.3 μm IDT.

The acoustic wave modulates the nanocavity's resonance mode mainly through elasto-optic effect, in which the strain field of the acoustic wave dynamically changes the material's refractive index. Therefore, the variation of the acousto-optic modulation

strength among the various Lamb wave modes is related to the different modal overlap between their strain field distribution and the electric field distribution of the nanocavity's resonance mode. More detailed theory of the acousto-optic modal overlap can be found in our previous work [23]. In addition, the varying excitation efficiency and propagation loss of the different acoustic modes also play a role in the overall efficiency. For example, as shown in Figure 5.3c, the A-modes have a strain field distribution that is antisymmetric with respect to a lateral plane dissecting the membrane, resulting in cancellation of elasto-optic effect when its overlap with the optical mode integrated over the thickness of the membrane. This is in contrast to the S-modes where the symmetric strain field distribution results in enhanced elasto-optic overlap integral with the optical mode, and thus enhanced acousto-optic modulation. On top of that, the S-modes have relatively higher excitation efficiency by the IDT than the A-modes, as can be seen from the S_{11} spectra (S-modes have deeper dips than A-modes). This trend, however, is counteracted by the fact that the S-modes have higher frequencies than the A-modes and hence higher propagation loss. The dramatically reduced modulation strength of the higher order modes (A1 and S1) is attributed to their high propagation loss, since propagation loss of acoustic waves scales approximately as the square of the frequency [123]. Among Lamb waves of different wavelengths (0.3 and 2.0 μm), the modulation strength is highly dependent on the ratio of the acoustic wavelength to the width of the nanocavity, which is fixed at 0.8 μm in our devices. Acousto-optical modal overlap is non-vanishing if the acoustic wavelength is more than twice the nanocavity width, which is the case for the device with 2.0 μm period IDT. For the device with 0.3 μm period IDT,

the acousto-optic modulation is much weaker due to the vanishing modal overlap for it is integrated over the nanocavity's width of several acoustic wavelengths, as shown in Figure 5.3c. In addition to the main peaks corresponding to the well-defined acoustic modes, in the optical S_{21} spectra shown in Figure 5.4, there are several unidentified peaks and many ripples. We currently attribute them to the reflection of the acoustic wave at the complicated boundary of the suspended membrane (see Figure 5.1a) and the interference it has caused. By introducing efficient absorbing structures around the devices, undesired reflection of acoustic waves can be reduced and those spurious peaks can be eliminated.

5.3.3. Lamb Wave Photonic Crystal Cavity Optomechanical Coupling Efficiency

We quantify the devices' overall acousto-optic modulation efficiency (G) by performing a calibrated modulation measurement [23]. The efficiency is defined as the change in the optical cavity's resonance frequency per square root of the microwave power sent to the IDT:

$$G = \Delta\omega / \sqrt{P_{\mathrm{RF}}} \qquad \textbf{5.1}$$

where $\Delta\omega$ is the change in resonance frequency of the optical nanocavity due to acousto-optic modulation, and P_{RF} is the microwave power sent to the Lamb wave transducer. The change in resonance frequency is extracted from the modulation S_{21} spectrum taking into account the slope of the optical cavity resonance at the probe laser wavelength. The results are summarized in Table 5-1.

Table 5-1 Measured acousto-optic modulation efficiency G.

Mode	Λ = 2.0 μm		Λ = 0.3 μm	
	f [GHz]	$G/2\pi$ [MHz/mW$^{1/2}$]	f [GHz]	$G/2\pi$ [MHz/mW$^{1/2}$]
A0	1.35	760	16.39	6.35
S0	5.28	1570	19.20	7.4
A1	10.14	26		
S1	14.21	37		

For the device with 2.0 μm period IDT, the fundamental modes A0 and S0 have an order of magnitude higher efficiency than the higher order modes A1 and S1. The S0 mode, with its combined high efficiency and high frequency, thus is more ideal for cavity optomechanical experiments. Although much weaker than its fundamental counterpart, the S1 mode is also interesting for its ultra-high frequency. For the device with 0.3 μm period IDT, the modulation efficiency for both A0 and S0 modes is much lower than that of the 2.0 μm period IDT. This is expected as the Lamb wavelength is a small fraction (almost a third) of the nanocavity's width, leading to a very small acousto-optic modal overlap integral. This problem can be solved by designing a nanocavity with a very small effective mode width, such as the dumbbell slot cavity design [124]. Previously, on unsuspended AlN on oxidized SiO_2 substrate, we have demonstrated SAW modulation of photonic nanocavity at 12.12 GHz with efficiency of 16.7 MHz·mW$^{-1/2}$ [24]. For comparison, in the current scheme, for the S0 mode at 5.28 GHz, the modulation efficiency is improved by two orders of magnitude, for the S1 mode at 14.14 GHz, the modulation efficiency is two times as high. This highlights the importance of the suspended platform in enhancing acousto-optic interaction and achieving high frequency

modulation. Similar work on SAW modulation of photonic crystal cavity was reported with modulation efficiency as high as 12.6 GHz/mW$^{1/2}$ but at much lower frequency of 1.7 GHz [55].

5.4. Summary

In summary, we have demonstrated an optomechanical system on a suspended AlN membrane on which very high frequency acoustic transducers and photonic crystal nanocavities are integrated. The system overcomes the limitation of the unsuspended AlN platform where the acoustic wave leaks into the substrate layer without contributing to the acousto-optic interaction. The platform is promising for studying interaction between cavity confined photons and propagating phonons of microwave frequency. In additional, the strong and high frequency acoustic waves realized in this platform can provide spatially-coherent time-domain modulation to induce non-reciprocity and break time-reversal symmetry in photonic systems [70], [125]. At this high acoustic frequency, this system can also be applied for microwave photonics technology where optical and microwave channels of communication can be linked and interchanged [126].

Chapter 6. Conclusion

The motivation of the doctoral research was introduced in line with the research trend in the field of cavity optomechanics.

Basic physics and generation mechanisms of surface acoustic waves is discussed. Implementation issues like design and modeling techniques, fabrication processes, and characterization schemes are discussed. Measurement results from a typical device that illustrates the surface acoustic wave transduction and propagation properties is presented.

Acousto-optic modulation of optical racetrack resonator with surface acoustic wave at frequencies above 10 GHz is demonstrated. With the achieved ultrahigh acoustic frequency, an unprecedented sub-optical wavelength regime of acousto-optics is reached. The dependence of the optomechanical coupling strength on modal and phase matching between the acoustic and optical modes is investigated. Design rules to improve the optomechanical coupling strength is presented.

Optomechanical coupling in the sideband resolved regime is achieved by integrating the high frequency surface acoustic wave transducers with photonic crystal nanocavity. This device was used to demonstrate optomechanically induced transparency and absorption. The scalability of the system is demonstrated by realizing coherent interaction of the surface acoustic wave with multiple photonic cavities. On the same platform, a photonic nanocavity placed inside an acoustic echo-chamber was used to demonstrate photonic cavity interaction with acoustic pulse.

The optomechanical coupling strength was further improved by implementing the surface acoustic wave photonic cavity integrated system on suspended aluminum nitride

membrane. The system overcomes the limitation of the unsuspended aluminum nitride platform where the acoustic wave leaks into the oxidized silicon substrate without contributing to the optomechanical interaction. Optomecahnical coupling strength an order of magnitude better than the unscescpended platform is achieved. Ultra small period transducers and the acoustic dispersion property of the membrane was utilized to push the generated acoustic wave frequency to over 19 GHz.

To conclude this thesis, I highlight three main features of our SAW/Lamb wave based optomechanical system and its merits compared to traditional optomechanical systems.

First, the photonic and mechanical systems design is uncoupled giving flexibility to optimize the components independently for improved performance. For example, state of the art nanofabrication techniques can be used to fabricate small period IDTs that can generate ultrahigh frequency acoustic waves. This enables reaching deep sideband resolved optmechanical coupling regime where interesting dynamical processes of photon-phonon interaction can be explored. From application point of view, such system can be used as a link for optical and very high frequency microwave domain signals.

Secondly, the propagating nature of the mechanical modes allows coherent interaction of the phonons with spatially separated multiple nanocavities. This highlights scalability of our system.

Third, the acoustic wave induced spatial and temporal optical modulation can be utilized to realize nonreciprocal photonic structures using the principles of Brillioun scattering and indirect interband photonic transitions. This is an ongoing effort in our research group.

Chapter 7. Bibliography

[1] M. Aspelmeyer, T. J. Kippenberg, and F. Marquardt, "Cavity optomechanics," *Rev. Mod. Phys.*, vol. 86, no. 4, pp. 1391–1452, Dec. 2014.

[2] "MAXWELL, James Clerk. A Treatise on Electricity and Magnetism. Oxford: Clarendon Press, 1873.

[3] R. Frisch, "Experimenal demonstration of Einstein's radiation recoil," *Zeitschrift for Phys.*, vol. 86, no. 1–2, pp. 42–48, Jan. 1933.

[4] R. A. Beth, "Mechanical Detection and Measurement of the Angular Momentum of Light," *Phys. Rev.*, vol. 50, no. 2, pp. 115–125, Jul. 1936.

[5] A. Ashkin, "Acceleration and Trapping of Particles by Radiation Pressure," *Phys. Rev. Lett.*, vol. 24, no. 4, pp. 156–159, Jan. 1970.

[6] T. W. Hänsch and A. L. Schawlow, "Cooling of gases by laser radiation," *Opt. Commun.*, vol. 13, no. 1, pp. 68–69, Jan. 1975.

[7] H. D. Wineland, D. J., "No Title," *Bull. Am. Phys. Soc*, vol. 20, no. 637, 1975.

[8] V. B. Braginskiĭ and A. B. Manukin, "Ponderomotive Effects of Electromagnetic Radiation," *Sov. Phys. JETP*, vol. 25, 1967.

[9] V. B. Braginskiĭ, A. B. Manukin, and M. Y. Tikhonov, "Investigation of Dissipative Ponderomotive Effects of Electromagnetic Radiation," *Sov. J. Exp. Theor. Phys.*, vol. 31, 1970.

[10] A. Dorsel, J. D. McCullen, P. Meystre, E. Vignes, and H. Walther, "Optical Bistability and Mirror Confinement Induced by Radiation Pressure," *Phys. Rev. Lett.*, vol. 51, no. 17, pp. 1550–1553, Oct. 1983.

[11] K. J. Vahala, "Optical microcavities.," *Nature*, vol. 424, no. 6950, pp. 839–46, Aug. 2003.

[12] T. Carmon, H. Rokhsari, L. Yang, T. J. Kippenberg, and K. J. Vahala, “Temporal behavior of radiation-pressure-induced vibrations of an optical microcavity phonon mode.,” *Phys. Rev. Lett.*, vol. 94, no. 22, p. 223902, Jun. 2005.

[13] T. J. Kippenberg, H. Rokhsari, T. Carmon, A. Scherer, and K. J. Vahala, “Analysis of Radiation-Pressure Induced Mechanical Oscillation of an Optical Microcavity,” *Phys. Rev. Lett.*, vol. 95, no. 3, p. 033901, Jul. 2005.

[14] H. Rokhsari, T. J. Kippenberg, T. Carmon, and K. J. Vahala, “Radiation-pressure-driven micro-mechanical oscillator,” *Opt. Express*, vol. 13, no. 14, p. 5293, Jul. 2005.

[15] A. Schliesser, P. Del’Haye, N. Nooshi, K. J. Vahala, and T. J. Kippenberg, “Radiation Pressure Cooling of a Micromechanical Oscillator Using Dynamical Backaction,” *Phys. Rev. Lett.*, vol. 97, no. 24, p. 243905, Dec. 2006.

[16] O. Arcizet, P.-F. Cohadon, T. Briant, M. Pinard, and A. Heidmann, “Radiation-pressure cooling and optomechanical instability of a micromirror.,” *Nature*, vol. 444, no. 7115, pp. 71–4, Nov. 2006.

[17] S. Gigan, H. R. Böhm, M. Paternostro, F. Blaser, G. Langer, J. B. Hertzberg, K. C. Schwab, D. Bäuerle, M. Aspelmeyer, and A. Zeilinger, “Self-cooling of a micromirror by radiation pressure,” *Nature*, vol. 444, no. 7115, pp. 67–70, Nov. 2006.

[18] S. Weis, R. Rivière, S. Deléglise, E. Gavartin, O. Arcizet, A. Schliesser, and T. J. Kippenberg, “Optomechanically induced transparency.,” *Science*, vol. 330, no. 6010, pp. 1520–3, Dec. 2010.

[19] A. H. Safavi-Naeini, T. P. Mayer Alegre, J. Chan, M. Eichenfield, M. Winger, Q. Lin, J. T. Hill, D. E. Chang, and O. Painter, “Electromagnetically induced transparency and slow light with optomechanics.,” *Nature*, vol. 472, no. 7341, pp. 69–73, Apr. 2011.

[20] G. Anetsberger, O. Arcizet, Q. P. Unterreithmeier, R. Rivière, A. Schliesser, E. M. Weig, J. P. Kotthaus, and T. J. Kippenberg, “Near-field cavity optomechanics with nanomechanical oscillators,” *Nat. Phys.*, vol. 5, no. 12, pp. 909–914, Oct. 2009.

[21] A. Schliesser, G. Anetsberger, R. Rivière, O. Arcizet, and T. J. Kippenberg, "High-sensitivity monitoring of micromechanical vibration using optical whispering gallery mode resonators," *New J. Phys.*, vol. 10, no. 9, p. 095015, Sep. 2008.

[22] T. Westphal, D. Friedrich, H. Kaufer, K. Yamamoto, S. Goßler, H. Müller-Ebhardt, S. L. Danilishin, F. Y. Khalili, K. Danzmann, and R. Schnabel, "Interferometer readout noise below the standard quantum limit of a membrane," *Phys. Rev. A*, vol. 85, no. 6, p. 063806, Jun. 2012.

[23] S. A. Tadesse and M. Li, "Sub-optical wavelength acoustic wave modulation of integrated photonic resonators at microwave frequencies.," *Nat. Commun.*, vol. 5, p. 5402, Jan. 2014.

[24] H. Li, S. A. Tadesse, Q. Liu, and M. Li, "Nanophotonic cavity optomechanics with propagating acoustic waves at frequencies up to 12 GHz," *Optica*, vol. 2, no. 9, p. 826, Sep. 2015.

[25] S. A. Tadesse, H. Li, Q. Liu, and M. Li, "Acousto-optic modulation of a photonic crystal nanocavity with Lamb waves in microwave K band," *Appl. Phys. Lett.*, vol. 107, no. 20, p. 201113, Nov. 2015.

[26] Lord Rayleigh, "On Waves Propagated Along the Plane Surface of an Elastic Solid," *Proc. London Math. Soc.*, vol. 1, pp. 4–11, Jan. 1885.

[27] C. Campbell, *Surface Acoustic Wave Devices for Mobile and Wireless Communications*. Academic Press, 1998.

[28] and P. C. Jacques Curie, "Development, via compression, of electric polarization in hemihedral crystals with inclined faces.," *Bull. Soc. minéral. Fr.*, vol. 3, p. 90, 1880.

[29] G. Lippmann, "No Title," *Ann. Chim. Phy.*, vol. 24, pp. 145–178, 1881.

[30] P. Dineva, D. Gross, R. Müller, and T. Rangelov, *Dynamic Fracture of Piezoelectric Materials: Solution of Time-Harmonic Problems via BIEM*. Springer Science & Business Media, 2014.

[31] R. M. White and F. W. Voltmer, “DIRECT PIEZOELECTRIC COUPLING TO SURFACE ELASTIC WAVES,” *Appl. Phys. Lett.*, vol. 7, no. 12, p. 314, Nov. 1965.

[32] J. H. Hines and D. C. Malocha, “A simple transducer equivalent circuit parameter extraction technique,” *Proc. IEEE Ultrason. Symp.*, pp. 173–177 vol.1, 1993.

[33] C. Campbell, *Surface acoustic wave devices and their signal processing applications*. Academic Press, 1989.

[34] S. L. RUMYANTSEV, M. S. SHUR, and M. E. LEVINSHTEIN, “MATERIALS PROPERTIES OF NITRIDES: SUMMARY,” *Int. J. High Speed Electron. Syst.*, vol. 14, no. 01, pp. 1–19, Mar. 2004.

[35] A. Korpel, *Acousto-optics /*. Marcel Dekker, 1997.

[36] Berg, *Acousto-Optic Signal Processing: Theory and Implementation, Second Edition*, vol. 17. CRC Press, 1995.

[37] R. Y. Chiao, C. H. Townes, and B. P. Stoicheff, “Stimulated Brillouin Scattering and Coherent Generation of Intense Hypersonic Waves,” *Phys. Rev. Lett.*, vol. 12, no. 21, pp. 592–595, May 1964.

[38] E. P. Ippen, “Stimulated Brillouin scattering in optical fibers,” *Appl. Phys. Lett.*, vol. 21, no. 11, p. 539, Oct. 1972.

[39] T. Schneider, M. Junker, and D. Hannover, “Generation of millimetre-wave signals by stimulated Brillouin scattering for radio over fibre systems,” *Electron. Lett.*, vol. 40, no. 23, p. 1500, Nov. 2004.

[40] P. T. Rakich, C. Reinke, R. Camacho, P. Davids, and Z. Wang, “Giant Enhancement of Stimulated Brillouin Scattering in the Subwavelength Limit,” *Phys. Rev. X*, vol. 2, no. 1, p. 011008, Jan. 2012.

[41] K. Hashimoto, *Surface Acoustic Wave Devices in Telecommunications*. Berlin, Heidelberg: Springer Berlin Heidelberg, 2000.

[42] C. Gorecki, F. Chollet, E. Bonnotte, and H. Kawakatsu, “Silicon-based integrated interferometer with phase modulation driven by surface acoustic waves,” *Opt. Lett.*, vol. 22, no. 23, p. 1784, Dec. 1997.

[43] M. M. de Lima and P. V Santos, “Modulation of photonic structures by surface acoustic waves,” *Reports Prog. Phys.*, vol. 68, no. 7, pp. 1639–1701, Jul. 2005.

[44] M. M. de Lima, M. Beck, R. Hey, and P. V. Santos, “Compact Mach-Zehnder acousto-optic modulator,” *Appl. Phys. Lett.*, vol. 89, no. 12, p. 121104, Sep. 2006.

[45] M. Beck, M. M. de Lima, E. Wiebicke, W. Seidel, R. Hey, and P. V. Santos, “Acousto-optical multiple interference switches,” *Appl. Phys. Lett.*, vol. 91, no. 6, p. 061118, Aug. 2007.

[46] M. Beck, M. M. de Lima, and P. V. Santos, “Acousto-optical multiple interference devices,” *J. Appl. Phys.*, vol. 103, no. 1, p. 014505, Jan. 2008.

[47] Y. Takagaki, P. V. Santos, E. Wiebicke, O. Brandt, H.-P. Schönherr, and K. H. Ploog, “Guided propagation of surface acoustic waves in AlN and GaN films grown on 4 H – SiC (0001) substrates,” *Phys. Rev. B*, vol. 66, no. 15, p. 155439, Oct. 2002.

[48] G. F. Cardinale, J. L. Skinner, A. A. Talin, R. W. Brocato, D. W. Palmer, D. P. Mancini, W. J. Dauksher, K. Gehoski, N. Le, K. J. Nordquist, and D. J. Resnick, “Fabrication of a surface acoustic wave-based correlator using step-and-flash imprint lithography,” *J. Vac. Sci. Technol. B Microelectron. Nanom. Struct.*, vol. 22, no. 6, p. 3265, Dec. 2004.

[49] P. Kirsch, M. B. Assouar, O. Elmazria, V. Mortet, and P. Alnot, “5 GHz surface acoustic wave devices based on aluminum nitride/diamond layered structure realized using electron beam lithography,” *Appl. Phys. Lett.*, vol. 88, no. 22, p. 223504, May 2006.

[50] D. Neculoiu, A. Müller, G. Deligeorgis, A. Dinescu, A. Stavrinidis, D. Vasilache, A. M. Cismaru, G. E. Stan, and G. Konstantinidis, “AlN on silicon based surface acoustic wave resonators operating at 5 GHz,” *Electron. Lett.*, vol. 45, no. 23, p. 1196, Nov. 2009.

[51] S. Büyükköse, B. Vratzov, D. Ataç, J. van der Veen, P. V Santos, and W. G. van der Wiel, "Ultrahigh-frequency surface acoustic wave transducers on $ZnO/SiO_2/Si$ using nanoimprint lithography.," *Nanotechnology*, vol. 23, no. 31, p. 315303, Aug. 2012.

[52] S. Büyükköse, B. Vratzov, J. van der Veen, P. V. Santos, and W. G. van der Wiel, "Ultrahigh-frequency surface acoustic wave generation for acoustic charge transport in silicon," *Appl. Phys. Lett.*, vol. 102, no. 1, p. 013112, Jan. 2013.

[53] Y. Akahane, T. Asano, B.-S. Song, and S. Noda, "High-Q photonic nanocavity in a two-dimensional photonic crystal.," *Nature*, vol. 425, no. 6961, pp. 944–7, Oct. 2003.

[54] K. J. Vahala, "Optical microcavities.," *Nature*, vol. 424, no. 6950, pp. 839–46, Aug. 2003.

[55] D. A. Fuhrmann, S. M. Thon, H. Kim, D. Bouwmeester, P. M. Petroff, A. Wixforth, and H. J. Krenner, "Dynamic modulation of photonic crystal nanocavities using gigahertz acoustic phonons," *Nat. Photonics*, vol. 5, no. 10, pp. 605–609, Sep. 2011.

[56] G. Piazza, P. J. Stephanou, and A. P. Pisano, "Piezoelectric Aluminum Nitride Vibrating Contour-Mode MEMS Resonators," *J. Microelectromechanical Syst.*, vol. 15, no. 6, pp. 1406–1418, Dec. 2006.

[57] W. H. P. Pernice, C. Xiong, C. Schuck, and H. X. Tang, "High-Q aluminum nitride photonic crystal nanobeam cavities," *Appl. Phys. Lett.*, vol. 100, no. 9, p. 091105, Feb. 2012.

[58] C. Xiong, W. H. P. Pernice, and H. X. Tang, "Low-loss, silicon integrated, aluminum nitride photonic circuits and their use for electro-optic signal processing.," *Nano Lett.*, vol. 12, no. 7, pp. 3562–8, Jul. 2012.

[59] S. G. Johnson, M. Ibanescu, M. A. Skorobogatiy, O. Weisberg, J. D. Joannopoulos, and Y. Fink, "Perturbation theory for Maxwell's equations with shifting material boundaries.," *Phys. Rev. E. Stat. Nonlin. Soft Matter Phys.*, vol. 65, no. 6 Pt 2, p. 066611, Jun. 2002.

[60] A. Yariv and P. Yeh, “Optical waves in crystals : propagation and control of laser radiation,” *Opt. waves Cryst. Propag. Control laser Radiat.*, 2003.

[61] F. Calle, J. Pedros, T. Palacios, and J. Grajal, “Nitride-based surface acoustic wave devices and applications,” *Phys. status solidi*, vol. 2, no. 3, pp. 976–983, Feb. 2005.

[62] G. Bu, D. Ciplys, M. Shur, L. J. Schowalter, S. Schujman, and R. Gaska, “Electromechanical coupling coefficient for surface acoustic waves in single-crystal bulk aluminum nitride,” *Appl. Phys. Lett.*, vol. 84, no. 23, p. 4611, May 2004.

[63] E. Bausk, R. Taziev, and A. Lee, “Synthesis of slanted and quasi-slanted SAW transducers,” *IEEE Trans. Ultrason. Ferroelectr. Freq. Control*, vol. 51, no. 8, pp. 1002–1009, Aug. 2004.

[64] C.-M. Lin, Y.-Y. Chen, and T.-T. Wu, “A novel weighted method for layered SAW filters using slanted finger interdigital transducers,” *J. Phys. D. Appl. Phys.*, vol. 39, no. 3, pp. 466–470, Feb. 2006.

[65] A. El Habti, “High-frequency surface acoustic wave devices at very low temperature: Application to loss mechanisms evaluation,” *J. Acoust. Soc. Am.*, vol. 100, no. 1, p. 272, Jul. 1996.

[66] K. Yamanouchi, H. Nakagawa, and H. Odagawa, “GHz-range surface acoustic wave low loss filter at super low temperature,” in *Proceedings of the 1999 Joint Meeting of the European Frequency and Time Forum and the IEEE International Frequency Control Symposium (Cat. No.99CH36313)*, 1999, vol. 2, pp. 911–914.

[67] R. Blattmann, H. J. Krenner, S. Kohler, and P. Hänggi, “Entanglement creation in a quantum-dot–nanocavity system by Fourier-synthesized acoustic pulses,” *Phys. Rev. A*, vol. 89, no. 1, p. 012327, Jan. 2014.

[68] M. S. Kang, A. Butsch, and P. S. J. Russell, “Reconfigurable light-driven opto-acoustic isolators in photonic crystal fibre,” *Nat. Photonics*, vol. 5, no. 9, pp. 549–553, Aug. 2011.

[69] H. Shin, W. Qiu, R. Jarecki, J. A. Cox, R. H. Olsson, A. Starbuck, Z. Wang, and P.

T. Rakich, “Tailorable stimulated Brillouin scattering in nanoscale silicon waveguides.,” *Nat. Commun.*, vol. 4, p. 1944, Jan. 2013.

[70] Z. Yu and S. Fan, “Complete optical isolation created by indirect interband photonic transitions,” *Nat. Photonics*, vol. 3, no. 2, pp. 91–94, Jan. 2009.

[71] T. J. Kippenberg and K. J. Vahala, “Cavity optomechanics: back-action at the mesoscale.,” *Science*, vol. 321, no. 5893, pp. 1172–6, Aug. 2008.

[72] A. A. Savchenkov, A. B. Matsko, V. S. Ilchenko, D. Seidel, and L. Maleki, “Surface acoustic wave opto-mechanical oscillator and frequency comb generator.,” *Opt. Lett.*, vol. 36, no. 17, pp. 3338–40, Sep. 2011.

[73] A. H. Safavi-Naeini and O. Painter, “Proposal for an optomechanical traveling wave phonon–photon translator,” *New J. Phys.*, vol. 13, no. 1, p. 013017, Jan. 2011.

[74] J. Xu and R. Stroud, *Acousto-optic devices: principles, design, and applications*. Wiley, 1992.

[75] P. Gräupner, J. C. Pommier, A. Cachard, and J. L. Coutaz, “Electro-optical effect in aluminum nitride waveguides,” *J. Appl. Phys.*, vol. 71, no. 9, p. 4136, 1992.

[76] S. Y. Davydov, “Evaluation of physical parameters for the group III nitrates: BN, AlN, GaN, and InN,” *Semiconductors*, vol. 36, no. 1, pp. 41–44, Jan. 2002.

[77] A. F. Wright, “Elastic properties of zinc-blende and wurtzite AlN, GaN, and InN,” *J. Appl. Phys.*, vol. 82, no. 6, p. 2833, Sep. 1997.

[78] F. Marquardt and S. M. Girvin, “Trend: Optomechanics,” *Physics (College. Park. Md).*, vol. 2, May 2009.

[79] S. Mancini, D. Vitali, and P. Tombesi, “Scheme for teleportation of quantum states onto a mechanical resonator.,” *Phys. Rev. Lett.*, vol. 90, no. 13, p. 137901, Apr. 2003.

[80] K. Børkje, A. Nunnenkamp, and S. M. Girvin, “Proposal for entangling remote micromechanical oscillators via optical measurements.,” *Phys. Rev. Lett.*, vol. 107, no. 12, p. 123601, Sep. 2011.

[81] M. Karuza, C. Biancofiore, M. Bawaj, C. Molinelli, M. Galassi, R. Natali, P. Tombesi, G. Di Giuseppe, and D. Vitali, “Optomechanically induced transparency in a membrane-in-the-middle setup at room temperature,” *Phys. Rev. A*, vol. 88, no. 1, p. 013804, Jul. 2013.

[82] J. Chan, T. P. M. Alegre, A. H. Safavi-Naeini, J. T. Hill, A. Krause, S. Gröblacher, M. Aspelmeyer, and O. Painter, “Laser cooling of a nanomechanical oscillator into its quantum ground state,” *Nature*, vol. 478, no. 7367, pp. 89–92, Oct. 2011.

[83] J. D. Teufel, T. Donner, D. Li, J. W. Harlow, M. S. Allman, K. Cicak, A. J. Sirois, J. D. Whittaker, K. W. Lehnert, and R. W. Simmonds, “Sideband cooling of micromechanical motion to the quantum ground state.,” *Nature*, vol. 475, no. 7356, pp. 359–63, Jul. 2011.

[84] D. W. C. Brooks, T. Botter, S. Schreppler, T. P. Purdy, N. Brahms, and D. M. Stamper-Kurn, “Non-classical light generated by quantum-noise-driven cavity optomechanics.,” *Nature*, vol. 488, no. 7412, pp. 476–80, Aug. 2012.

[85] A. H. Safavi-Naeini, S. Gröblacher, J. T. Hill, J. Chan, M. Aspelmeyer, and O. Painter, “Squeezed light from a silicon micromechanical resonator.,” *Nature*, vol. 500, no. 7461, pp. 185–9, Aug. 2013.

[86] R. M. Shelby, M. D. Levenson, and P. W. Bayer, “Guided acoustic-wave Brillouin scattering,” *Phys. Rev. B*, vol. 31, no. 8, pp. 5244–5252, Apr. 1985.

[87] P. S. J. Russell, D. Culverhouse, and F. Farahi, “Theory of forward stimulated Brillouin scattering in dual-mode single-core fibers,” *IEEE J. Quantum Electron.*, vol. 27, no. 3, pp. 836–842, Mar. 1991.

[88] M. S. Kang, A. Brenn, and P. S. J. Russell, “All-optical control of gigahertz acoustic resonances by forward stimulated interpolarization scattering in a photonic crystal fiber.,” *Phys. Rev. Lett.*, vol. 105, no. 15, p. 153901, Oct. 2010.

[89] B. J. Eggleton, C. G. Poulton, and R. Pant, “Inducing and harnessing stimulated

Brillouin scattering in photonic integrated circuits," *Adv. Opt. Photonics*, vol. 5, no. 4, p. 536, Dec. 2013.

[90] J.-C. Beugnot, S. Lebrun, G. Pauliat, H. Maillotte, V. Laude, and T. Sylvestre, "Brillouin light scattering from surface acoustic waves in a subwavelength-diameter optical fibre.," *Nat. Commun.*, vol. 5, p. 5242, Jan. 2014.

[91] R. Van Laer, B. Kuyken, D. Van Thourhout, and R. Baets, "Interaction between light and highly confined hypersound in a silicon photonic nanowire," *Nat. Photonics*, vol. 9, no. 3, pp. 199–203, Feb. 2015.

[92] M. Merklein, I. V Kabakova, T. F. S. Büttner, D.-Y. Choi, B. Luther-Davies, S. J. Madden, and B. J. Eggleton, "Enhancing and inhibiting stimulated Brillouin scattering in photonic integrated circuits.," *Nat. Commun.*, vol. 6, p. 6396, Jan. 2015.

[93] M. Tomes and T. Carmon, "Photonic micro-electromechanical systems vibrating at X-band (11-GHz) rates.," *Phys. Rev. Lett.*, vol. 102, no. 11, p. 113601, Mar. 2009.

[94] G. Bahl, M. Tomes, F. Marquardt, and T. Carmon, "Observation of spontaneous Brillouin cooling," *Nat. Phys.*, vol. 8, no. 3, pp. 203–207, Jan. 2012.

[95] G. Bahl, J. Zehnpfennig, M. Tomes, and T. Carmon, "Stimulated optomechanical excitation of surface acoustic waves in a microdevice.," *Nat. Commun.*, vol. 2, p. 403, Jan. 2011.

[96] S. Yang, J. H. Page, Z. Liu, M. L. Cowan, C. T. Chan, and P. Sheng, "Focusing of sound in a 3D phononic crystal.," *Phys. Rev. Lett.*, vol. 93, no. 2, p. 024301, Jul. 2004.

[97] S. Mohammadi, A. A. Eftekhar, W. D. Hunt, and A. Adibi, "High-Q micromechanical resonators in a two-dimensional phononic crystal slab," *Appl. Phys. Lett.*, vol. 94, no. 5, p. 051906, Feb. 2009.

[98] E. B. Magnusson, B. H. Williams, R. Manenti, M.-S. Nam, A. Nersisyan, M. J. Peterer, A. Ardavan, and P. J. Leek, "Surface acoustic wave devices on bulk ZnO crystals at low temperature," *Appl. Phys. Lett.*, vol. 106, no. 6, p. 063509, Feb. 2015.

[99] M. V Gustafsson, T. Aref, A. F. Kockum, M. K. Ekström, G. Johansson, and P. Delsing, “Propagating phonons coupled to an artificial atom.,” *Science*, vol. 346, no. 6206, pp. 207–11, Oct. 2014.

[100] J. Bochmann, A. Vainsencher, D. D. Awschalom, and A. N. Cleland, “Nanomechanical coupling between microwave and optical photons,” *Nat. Phys.*, vol. 9, no. 11, pp. 712–716, Sep. 2013.

[101] K. Y. Fong, L. Fan, L. Jiang, X. Han, and H. X. Tang, “Microwave-assisted coherent and nonlinear control in cavity piezo-optomechanical systems,” *Phys. Rev. A*, vol. 90, no. 5, p. 051801, Nov. 2014.

[102] S. Datta, *Surface acoustic wave devices*. Prentice-Hall, 1986.

[103] M. V. Gustafsson, P. V. Santos, G. Johansson, and P. Delsing, “Local probing of propagating acoustic waves in a gigahertz echo chamber,” *Nat. Phys.*, vol. 8, no. 4, pp. 338–343, Feb. 2012.

[104] Q. Quan and M. Loncar, “Deterministic design of wavelength scale, ultra-high Q photonic crystal nanobeam cavities.,” *Opt. Express*, vol. 19, no. 19, pp. 18529–42, Sep. 2011.

[105] A. Ruiz M. and P. B. Nagy, “Diffraction correction for precision surface acoustic wave velocity measurements,” *J. Acoust. Soc. Am.*, vol. 112, no. 3, p. 835, Sep. 2002.

[106] A. Khelif, A. Choujaa, S. Benchabane, B. Djafari-Rouhani, and V. Laude, “Guiding and bending of acoustic waves in highly confined phononic crystal waveguides,” *Appl. Phys. Lett.*, vol. 84, no. 22, p. 4400, May 2004.

[107] A. El Habti, “High-frequency surface acoustic wave devices at very low temperature: Application to loss mechanisms evaluation,” *J. Acoust. Soc. Am.*, vol. 100, no. 1, p. 272, Jul. 1996.

[108] Q. Quan and M. Loncar, “Deterministic design of wavelength scale, ultra-high Q photonic crystal nanobeam cavities.,” *Opt. Express*, vol. 19, no. 19, pp. 18529–42, Sep. 2011.

[109] M.-S. Lee, S. Wu, Z.-X. Lin, and R. Ro, “Bulk Acoustic Wave Analysis of Crystalline-Plane-Oriented Aluminum Nitride Films,” *Japanese Journal of Applied Physics*, vol. 46, no. 10A. pp. 6719–6726, 2007.

[110] J. D. Joannopoulos, S. G. Johnson, J. N. Winn, and R. D. Meade, *Photonic Crystals: Molding the Flow of Light (Second Edition)*. Princeton University Press, 2011.

[111] H. A. Haus, *Waves and Fields in Optoelectronics*. Englewood Cliffs: Prentice-Hall, Inc., Englewood Cliffs, New Jersey, 1984.

[112] S. Fan, W. Suh, and J. D. Joannopoulos, “Temporal coupled-mode theory for the Fano resonance in optical resonators,” *J. Opt. Soc. Am. A*, vol. 20, no. 3, p. 569, Mar. 2003.

[113] M. Xu and L. V. Wang, “Photoacoustic imaging in biomedicine,” *Rev. Sci. Instrum.*, vol. 77, no. 4, p. 041101, Apr. 2006.

[114] J. Xu and R. Stroud, *Acousto-optic devices: principles, design, and applications*. Wiley, 1992.

[115] *Guided-Wave Acousto-Optics: Interactions, Devices, and Applications*. Springer Science & Business Media, 2013.

[116] T. Sogawa, P. V. Santos, S. K. Zhang, S. Eshlaghi, A. D. Wieck, and K. H. Ploog, “Dynamic band-structure modulation of quantum wells by surface acoustic waves,” *Phys. Rev. B*, vol. 63, no. 12, p. 121307, Mar. 2001.

[117] X. Sun, X. Zhang, and H. X. Tang, “High-Q silicon optomechanical microdisk resonators at gigahertz frequencies,” *Appl. Phys. Lett.*, vol. 100, no. 17, p. 173116, Apr. 2012.

[118] R. Pant, C. G. Poulton, D.-Y. Choi, H. Mcfarlane, S. Hile, E. Li, L. Thevenaz, B. Luther-Davies, S. J. Madden, and B. J. Eggleton, “On-chip stimulated Brillouin scattering.,” *Opt. Express*, vol. 19, no. 9, pp. 8285–90, Apr. 2011.

[119] R. Van Laer, B. Kuyken, D. Van Thourhout, and R. Baets, “Interaction between

light and highly confined hypersound in a silicon photonic nanowire," *Nat. Photonics*, vol. 9, no. 3, pp. 199–203, Feb. 2015.

[120] D. ROYER and E. Dieulesaint, *Elastic Waves in Solids I: Free and Guided Propagation*, vol. 29. Springer Science & Business Media, 1999.

[121] V. Yantchev and I. Katardjiev, "Thin film Lamb wave resonators in frequency control and sensing applications: a review," *J. Micromechanics Microengineering*, vol. 23, no. 4, p. 043001, Apr. 2013.

[122] E. Dogheche, D. Remiens, S. Shikata, A. Hachigo, and H. Nakahata, "High-frequency surface acoustic wave devices based on LiNbO[sub 3]/diamond multilayered structure," *Appl. Phys. Lett.*, vol. 87, no. 21, p. 213503, Nov. 2005.

[123] E. Dogheche, D. Remiens, S. Shikata, A. Hachigo, and H. Nakahata, "High-frequency surface acoustic wave devices based on LiNbO[sub 3]/diamond multilayered structure," *Appl. Phys. Lett.*, vol. 87, no. 21, p. 213503, Nov. 2005.

[124] W. H. P. Pernice, C. Xiong, and H. X. Tang, "Photonic crystal dumbbell resonators in silicon and aluminum nitride integrated optical circuits," *J. Nanophotonics*, vol. 7, no. 1, p. 073095, Apr. 2013.

[125] K. Fang, Z. Yu, and S. Fan, "Realizing effective magnetic field for photons by controlling the phase of dynamic modulation," *Nat. Photonics*, vol. 6, no. 11, pp. 782–787, Oct. 2012.

[126] J. Capmany and D. Novak, "Microwave photonics combines two worlds," *Nat. Photonics*, vol. 1, no. 6, pp. 319–330, Jun. 2007.